Mid-Infrared-Emitting Quantum Cascade Lasers on Metamorphic Buffer Layers

By

Ayushi Rajeev

A dissertation submitted in partial fulfillment of

the requirements for the degree of

Doctor of Philosophy

(Electrical Engineering)

at the

UNIVERSITY OF WISCONSIN-MADISON

2019

Date of final oral examination: March 28, 2019

The dissertation is approved by the following members of the Final Oral Committee:

Luke J. Mawst, Professor, Electrical and Computer Engineering

Dan Botez, Professor, Electrical and Computer Engineering

Thomas F. Kuech, Professor, Chemical and Biological Engineering

Susan E. Babcock, Professor, Materials Science and Engineering

Abstract

When using conventional substrates, such as InP and GaAs, the materials constituting the superlattice (SL) core region of the quantum cascade laser (QCL) are constrained by strain-induced critical-thickness limitations. Metamorphic buffer layers (MBLs) can serve as “virtual substrates” with a designer-chosen surface lattice constant, thus expanding the compositional-design space for a variety of device structures, including short-wavelength QCLs. An optimized short-wavelength (3.4 µm) single-phonon-resonant (SPR)+ miniband extraction QCL design, grown on an $In_xGa_{1-x}As$ MBL, is presented along with the optical and thermal device considerations in play. MBLs can be grown with a variety of graded regions such as linear composition grade from GaAs to $In_xGa_{1-x}As$ or by employing dislocation filters between Si substrate and InP. QCL and test superlattices’ regrowth on these MBLs with the corresponding materials and device analysis, is presented in this work.

In addition to the materials limitation for the design of QCL devices, the requirement to have the constituent layers (1-5 nm) to be precisely controlled in the various compositions and thicknesses, is a challenge. Interfacial grading in strained SLs is studied via atom probe tomography for SLs with various layer thicknesses and relative lattice strains. The tip reconstructions are analyzed by fitting the interfaces to diffusion profiles. Mechanisms possible for the observed interdiffusion profile, such as surface segregation and/or bulk diffusion, are discussed.

With an understanding of the compositional gradient at the interfaces, together with optimized QCL designs and regrowth on the MBLs, short-wavelength QCLs with high performances can be achieved.

Acknowledgements

I would like to use this opportunity to express gratitude to everyone I encountered during my time at UW-Madison, in turn helping me along the way in some aspect or the other. First and foremost, I thank my advisor, Prof. Luke Mawst for taking me into his group as a new graduate student and giving me the opportunity to work under his guidance. I would also like to thank my prelim and defense exam committee members, Prof. Dan Botez, Prof. Sue Babcock and Prof. Tom Kuech, for their time and support through the years and for providing a good direction to this work through their comments and suggestions.

I would like to acknowledge the support of my colleagues: Dr. Kevin Schulte, Dr. TaeWan Kim, Dr. Toby Garrod, Dr. Chun-Chieh Chang, Dr. Jeremy Kirch and Colin Boyle for being very patient teachers as I leant k.p modeling, MOCVD growth, device fabrication, MBL theory and material characterization. I also thank Dr. Chris Sigler for COMSOL simulations and our collaboration on projects involving device simulations, Honghyuk Kim for readily processing QCL devices on MBLs, Kevin Oresick and Don Lindberg III for assistance and expertise on device testing, Cathy (Xiaoqing) Li for TEM analysis, Junyan Miao for help with HVPE MBLs, Brian Zutter, Phillip Buelow, Aaron Tan and Micah Cheng for their prompt polishing of substrates for device growth, and also Tom Earles, Jae Ha Ryu, Dr. Kaddour Lekhal, Dr. Omar Elleuch and Shining Xu. I thank my collaborators: Prof K. M. Lau and group at HKUST for providing InP MBLs and Dr. Yuri Flores for help with IFR studies. The atom probe tomography experiments necessitate a special mention for Weixin Chen for teaching me the basics, Ben Knipfer for assisting with sample prep and experiments and Dr. Dieter Isheim at Northwestern University for a very helpful and long-lasting collaboration. My sincere thanks to all the staff scientists at Wisconsin Center for

Nanoscale Technology for trainings on the various instruments and always being available for research specific discussions.

Most importantly, I would like to thank my parents, brother and husband for their support at every step of the way and making sure I reach the finish line.

I am grateful for funding from the following sources: The National Science Foundation (PFI-1317292); (DMR-1121288) and (DMR-0832760), Navy STTR N68335-11-C-0432, Air Force Research Laboratory under Grant FA8650-13-21616 and NSF ECCS 1806285. I'd also like to gratefully acknowledge support and use of facilities and instrumentation supported by the University of Wisconsin Materials Research Science and Engineering Center (DMR-1121288).

Contents

Chapter 1 Introduction 1
1.1 Mid-infrared quantum cascade lasers (QCLs) 1
1.2 Metamorphic buffer layers (MBLs) as substrates 2
1.3 Motivation 3
1.4 Organization 4
Chapter 2 λ~ 3.4 µm QCLs on InGaAs Metamorphic Buffer Layers 7
2.1 Introduction 7
2.2 Quantum Cascade Laser Design 9
2.2.1 Quantum Cascade Laser Active-Region Design 9
2.2.2 Complete Quantum Cascade Laser Structure: Thermo-Optical Analysis 11
2.3 Experimental Details 15
2.4 Results and Discussion 16
2.4.1 HVPE-MBL Surface Preparation 16
2.4.2 QCL design 17
2.4.3 QCL active region regrowth: test structures 31
2.4.4 QCL active region regrowth: complete structure 36
2.4.5 MOCVD-MBL 40
2.5 Conclusions 43
Chapter 3 λ~ 4.8 µm QCLs on InP Metamorphic Buffer Layers 48
3.1 Introduction 48
3.2 InP MBLs 51
3.3 Experiment details and discussion 52
3.3.1 Surface Preparation Techniques 53
3.3.2 Strained Superlattice test structures 56
3.3.3 QCL test structures and complete device growths 60

3.4 Conclusions 69
Chapter 4 Atom Probe Tomography for Interface Analysis 73
4.1 Introduction 73
4.2 Principle of operation 74
4.3 Experimental Setup 77
4.4 Reconstruction and Analysis 85
4.4.1 Extent of Intermixing in the Thick-motif sample 89
4.4.2 Extent of Intermixing in the Thin-motif sample 91
4.4.3 Layer thickness dependent interfacial intermixing 94
4.4.4 Lateral Interface Roughness 98
4.5 Conclusions 99
Chapter 5 Concluding Remarks 103
5.1 Summary 103
5.2 Future Work 104

List of Figures

Figure 2.1 CB diagram and modulus squared of the most relevant wavefunctions shown at the operating electric field at threshold (142 kV⁄cm) for a 3.39 µm emitting, SPR + miniband-extraction QCL design grown on an $In_{0.22}Ga_{0.78}As$ MBL cap layer. The primed numbers identify wavefunctions from the extractor region that penetrate into the AR. 10

Figure 2.2 Complete laser structure showing the upper and lower optical confinement layers and the cladding layers. 12

Figure 2.3 AFM measurements showing surface morphology of MBLs post annealing treatment at 630 °C (a) As-grown,(b) CMP treatment applied,(c) CMP and Wet-etching treatment applied. 17

Figure 2.4 Calculated EL spectrum for the 3.39 µm emitting QCL on MBL design (figure 2.1). Inhomogeneous broadening due to IFR scattering has been considered for calculations. 27

Figure 2.5. Simulation of magnetic-field intensity profile of the fundamental transverse mode for the complete laser structure with 2 µm thick: (a) $In_{0.69}Ga_{0.31}P$; (b) $In_{0.21}Al_{0.79}As$ lower-cladding layers. 29

Figure 2.6 Simulated thermal dissipation within the complete laser structure, for a 5 mm long device. with: (a) InP; (b) $In_{0.69}Ga_{0.31}P$; (c) $In_{0.21}Al_{0.79}As$ cladding layers, for 15 W power to dissipate. 30

Figure 2.7 Optical Images, using Nomarski interference contrast, depicting surface morphology of (a) As-grown MBL, (b) 10-stage QCL active region regrowth on a surface- optimized MBL. 32

Figure 2.8 TEM images: (a){220} dark- field image of ten stages of QCL active region regrowth on an MBL, showing dislocations propagating from the cap layer through the regrown SL layers, (b)Higher magnification image of (a),(c)Phase contrast high-resolution image providing atomic detail within a stage. 33

Figure 2.9 HR-XRD scans (a) (004) ω–2θ RSM, (b) (004) ω–2θ line scan (solid) compared with best fit simulation (dashed). 34

Figure 2.10 TEM images for the growth of the 10-stages of the QCL active region with cladding and confinement layers (a) lower magnification image showing the entire structure (b) higher magnification image showing the 10-stage repetition and a defect propagating through the constituent SL 35

Figure 2.11 HRXRD along the (004) comparing the 10-stage regrowth with and without the upper cladding. 35

Figure 2.12: I-V characteristics for 4 mesa devices obtained from 10-stage QCL sample 36

Figure 2.13 (004) RSM for the 30-stages of the active region regrowth on the lower cladding, with the corresponding omega-2theta extracted scan 37

Figure 2.14 Nomarski image of the surface after 30-stage QCL regrowth on lower cladding and confinement layers atop the MBL 37

Figure 2.15: Cross-sectional SEM image showing the fabricated ridge waveguide device from the complete laser structure regrowth using the 30-stage QCL on the MBL 38

Figure 2.16: Cross-sectional STEM images of the full QCL structure regrowth on an MBL, shown at various magnifications 39

Figure 2.17: I-V characteristics for 2 ridge guide devices obtained from the 30-stage QCL sample, with the measurement iteration as indicated 40

Figure 2.18 MOCVD MBL1 (a) 004 XRD scan (b) 004 RSM (c) Nomarski optical image showing the cross-hatched surface........ 41

Figure 2.19 (a) Surface morphology of MOCVD MBL2 by a Normarski optical image (b) (004) XRD scan 42

Figure 2.20 Nomarski optical images of MOCVD MBL2 (a) as-grown with a thick cap layer (b) after CMP procedure 43

Figure 3.1 Optical microscopy images of InP MBL2 (a) As-grown (b) after CMP (c) after CMP and wet etching; AFM (d) As-grown (e) after CMP 54

Figure 3.2 Optical microscopy images of InP MBL2 (a) As-grown (b) after CP; AFM (c) As-grown (d) after CP 55

Figure 3.3 Atomic force microscopic images of InP MBL3 with (a) 2.5 μm of InP growth (b) 20 min CP subsequently........ 56

Figure 3.4 Nomarski optical images of an (a) as-grown MBL (b) MBL with 2.5 mm of InP growth (c) MBL with 20 min CP subsequently........ 56

Figure 3.5 Asymmetrical HRXRD (115) reciprocal space map for InP MBL1 57

Figure 3.6 EpiTT™ reflectometer measurement during the MOCVD growth, showing the reflectance and temperature profiles as a function of time. Blue scan is for InP MBL1and the red scan is for an InP substrate, indicative of 5 °C surface temperature difference between the two substrates. 58

Figure 3.7 (004) HRXRD scan from the growth of a 500 nm InP buffer and 10×SL: $In_{0.6}Ga_{0.4}As$ (3 nm)/ InP (31 nm) 58

Figure 3.8 HRXRD scans and simulation to fit experimental results for the growth of 150 nm InP buffer and 5 × SL: $In_{0.39}Al_{0.61}As$ (11.48 nm)/ $In_{0.635}Ga_{0.365}As$ (11.9 nm). 10 repetitions of the same SL are indicated on the graph. Scans are offset vertically for clarity. 59

Figure 3.9 HRXRD comparison between InP MBL1, InP MBL2 and InP MBL3 for the growth of 150 nm InP buffer and 5×SL: $In_{0.39}Al_{0.61}As$ (11.48 nm)/ $In_{0.635}Ga_{0.365}As$ (11.9 nm) 60

Figure 3.10 HRXRD scan for the growth of 1 μm InP buffer layer and 5 stages of the active region. 60

Figure 3.11 (-2-24) asymmetrical HRXRD RSM scan showing that the 5 stages of active region growth are strained with respect to InP 61

Figure 3.12 Photoluminescence measurements to compare the 5-stage growth on an InP substrate with that on the InP MBL3 62

Figure 3.13 HRTEM analysis for the regrowth of 5 stages of the QCL active region a) on an InP substrate b) on the InP MBL3 c) on the InP MBL3 with threading dislocation penetrating through 62

Figure 3.14 (004) HRXRD comparison of the regrowth of 40-stages of the active region on the InP MBL3 and InP 65

Figure 3.15 40-stage active region regrowth on InP MBL3 (a) surface morphology by a Nomarski optical image (b) SEM image showing undulations in the top stages grown towards the end of active region growth 65

Figure 3.16 Measured EL spectra for ridge waveguide device from QCL on InP MBL3 (current density 2.33 kA/cm^2) and mesa device from QCL on InP. 66

Figure 3.17 SEM image showing some undulations in the top stages grown towards the end of active region growth, but mostly planar in comparison to figure 3.15 (b) 67

Figure 3.18 Device characterization of the 20-stage QCL regrowth (a) RT-EL measurements for devices on InP MBL3 and InP (b) I-V curves of the devices on InP MBL3 vs InP substrate (c) L-I-V curves on the InP substrate 69

Figure 4.1: CAMECA 3000X Si™ instrument at the UW-Madison campus 77

Figure 4.2: Schematic showing key components of the experimental setup [1] 78

Figure 4.3 Schematic diagrams of the motif characteristics of the superlattice samples [15] 79

Figure 4.4 Preparation of an APT specimen by FIB lift out technique (a) deposition of a Pt cap over the wedge of interest; (b) wedge formation by milling at 30° to the normal; (c) weld the micromanipulator to one side of the now-released wedge; (d) mill the other side of the wedge to complete lift-off; (e) Pt welding of the wedge onto a Si micropost; (f) milled to separate one specimen from the wedge; (g) 90° rotated view of (f); (h) one of the many annular milling steps to form a tip; (i) further annular milling showing tip formation on the micropost with some material protrusions needing clean-up; (j) the tip showing the SL layers and substrate which will be ready for APT analysis after the removal of Pt protective layer 82

Figure 4.5 SL schematic to study the interfacial intermixing dependence on layer thicknesses. 84

Figure 4.6 (a) SEM image of the final tip shape before evaporation (b) HRTEM image 84

Figure 4.7 High-resolution X-ray diffraction (HRXRD) (004) ω-2θ scan for the thick-motif SL with simulations: (red) abrupt SL interfaces and (black) SL with a 1 nm thick constant composition intermixing layer. All scans are offset vertically for clarity 86

Figure 4.8 Atom maps for the obtained atom probe tomography (APT) for (a) thick-motif SL (b) thin-motif SL. 87

Figure 4.9 (a) Proxigram concentration profiles for the group III elements perpendicular to the interface in the thick-motif SL. Error bars represent counting-based statistical precision of the atom probe data; (b) Measured Al concentration profile, together with a best-fit semi-infinite solid solution to Fick's second law of diffusion applied to the InGaAs–InAlAs interface. 89

Figure 4.10 (a): Proxigram for thin-motif SL showing only group III concentrations. (b) Diffusion length estimation by fitting Fick's law of diffusion to the Al content profile 89

Figure 4.11 Reconstructed APT tip to study the layer thickness dependent interfacial intermixing. Only 50% of the Al and Ga atoms are shown. 96

Figure 4.12 Layer thickness dependent 1-D composition profile from (a) a central ROI within the reconstructed tip, looking at only Al and Ga profiles (b) STEM-EDX 97

Figure 4.12: a) InGaAs, growth rate= 0.09 nm/s, *T*= 605 °C, V/III= 495, RMS roughness= 0.199 nm b) InGaAs, growth rate= 0.09 nm/s, *T*= 605 °C, V/III= 496, RMS roughness =0.191 nm c) InAlAs, growth rate= 0.13 nm/s, *T*= 605 °C, V/III= 340, RMS roughness= 0.453 nm 99

List of Tables

Table 2.1 List of material parameters employed for thermo-optical analysis of the complete laser structure. Only the real parts of the refractive indices are noted here, although imaginary parts will be used for the calculation of losses as discussed below. 12

Table 2.2 List of the material parameters employed for thermal analysis of the complete laser structure. The room-temperature estimated thermal conductivity is provided where the temperature dependence is not well-known. 14

Table 2.3 Key parameters for SPR + miniband extraction QCL-structure designs grown on an MBL: the operating field at threshold; the energy difference between the upper laser level, state 3, and the next higher AR energy state, state 4, E_{43}; the energy level separation between the lower laser states (states 2 and 2') and the ground state of the next-stage injector, Δ_{inj}; the dipole matrix element between the upper laser level and lower laser level, z_{32g}; the lifetime of transitions between state 4 and state 3, τ_{43}, the global lifetimes for the upper and lower laser states, τ_{3g} and $\tau_{22'g}$; the average strain per stage; and the strain of well and barrier layers. For comparison, we also show the same parameters for SPR-only QCLs on InP [3] 19

Table 2.4: Strain × thickness products in units of Angstroms for the QCL design on MBL, compared with QCLs on InP substrate. 23

Table 2.5 Comparison of InGaP versus InAlAs as lower-cladding layers for 3.4 μm emitting QCLs, and of 3.4 μm emitting QCLs on MBL versus 4.6 μm emitting QCL. 26

Table 2.6 Calculated IFR intersubband scattering rate and times for selected states of the 3.39 μm emitting QCL on MBL design. Involved levels are labeled as in figure 2.1. 28

Table 2.7 Comparison of the target thicknesses for one stage of the active region design with the actual thickness values calculated from Figure 2.8 (c). All thickness values are in Angstroms. Bold numbers indicate wells and others indicate barriers in the QCL test structure. 33

Table 3.1 MO source conditions used for this work 53

Table 3.2 Typical growth rates and V/III ratios for this work [30]. 53

Table 4.1: Evaporative fields are listed for the primary elements under consideration in the materials studied (except P) [14] *Most abundant isotope listed in case of multiple isotopes **For single charge state 76

Table 4.2 Growth rates measured in calibration runs for V:III precursor ratios used to grow each superlattice (SL) 80

Table 4.3 SL layer compositions and SL periods determined from HRXRD simulations and APT reconstructions 87

Table 4.4 Diffusion lengths obtained by fitting Fick's second law to Al and Ga concentration profiles in the thick-motif sample (table 4.3), not accounting for the 10% discrepancy between HRXRD and APT SL period measurements 91

Table 4.5 Actual vs target thicknesses for the SL schematic in figure 4.5 94

Chapter 1 Introduction

1.1 Mid-infrared quantum cascade lasers (QCLs)

High-power lasers operating in the mid-infrared (IR) spectral region with emission in the 3.0 to 3.5 μm wavelength range have garnered interest due to applications such as advanced remote sensing and ranging. High-performance, low threshold-current density, interband-transition lasers have been reported within the 3.0 to 3.5 μm wavelength range by employing either type-I quantum wells (QWs) [1]–[3] or type-II QWs (i.e., interband cascade lasers) [4]–[6]. However, such devices are highly temperature sensitive due to hole leakage (in the case of type-I QW devices) as well as Auger recombination and/or Auger-assisted carrier leakage [1]–[8]. As a result, such devices exhibit low threshold-current characteristic temperature coefficient, T_0, values and low slope-efficiency characteristic temperature coefficient, T_1, values [1]–[6]. Since the maximum continuous-wave (CW) power, P_{max}, depends strongly on the T_0 and especially the T_1 values [9]–[11], this explains why the P_{max} values have been relatively low (<500 mW) from both type-I and type-II QW lasers operating in this wavelength range.

Quantum cascade lasers (QCLs), being intersubband (ISB)-transition devices, do not suffer from Auger recombination, thus relatively high T_0 values can be obtained [11] especially from devices designed for carrier-leakage suppression [11], [12]. QCLs have also achieved a wide range of emission wavelengths using a single-material system for designing and fabricating devices. However, when using conventional substrates, such as InP and GaAs, the materials constituting the superlattice (SL) core region of the QCL are constrained by strain-induced critical-thickness

limitations. It is well known that the degree of strain relaxation induced increases as one approaches the critical thickness of the individual (compressive-strained) QW and (tensile-strained) barrier layers constituting the SL, thus leading to subsequent device failure. Strain relaxation can also develop if the average strain of the SL core region becomes too large. However, the actual strain limits that can be tolerated without relaxation are impacted by kinetic factors, which, in turn, depend on the growth temperature and the growth rate.

1.2 Metamorphic buffer layers (MBLs) as substrates

MBLs enable the growth of lattice-mismatched layers through the growth of epitaxial layers by controlled chemical and structural transition [13]. Any epitaxial mismatched layer begins to relax once it reaches its critical thickness. For a graded MBL with many compositions, many different critical thicknesses exist. The lattice relaxation is associated with the formation of misfit dislocations which are generated when the glide force F_G is larger than the dislocation line tension F_L [14]. Various grading techniques have also been explored for $In_xGa_{1-x}As$/ GaAs material system such as linear grading [15], [16] and step graded buffers [17], [18]. Another approach to having an MBL is to grow a very thick layer of single composition.

MBLs have been extensively used to fabricate interband lasers, some examples of which are discussed. Nash et al. grew a high Al content $Al_zIn_{1-z}Sb$ interfacial layer on GaAs proceeded by 8 μm thick $Al_xIn_{1-x}Sb$ that also doubles as the bottom cladding layer [19]. The interfacial and the cladding layers accommodate the lattice mismatch between GaAs and GaInSb QWs. These type I QW diode lasers achieved pulsed 3.3 μm emission up to 202 K operating temperature. Gu et al. [20] employed an $In_{0.8}Al_{0.2}As$ MBL on InP grading the In content from 0.52 to 0.84. This acts as the bottom cladding layer for the type I laser and also reduces the strain in the InAs QWs

in order to obtain emission wavelengths up to 2.9 µm at 230 K for pulsed operation. InAsP MBLs grown on InP have enabled mid IR emission at 2.5 µm at 77 K from InAs QWs [21].

1.3 Motivation

As explained in sec 1.1, the move from interband lasers to conduction-band engineered ISB lasers is being witnessed to attain mid-IR emission wavelengths. For better strain compensation and increased flexibility with QCL design, MBLs are great candidates for custom substrates. ISB absorption from a strain compensation SL grown on an $Al_xIn_yGa_{1-x-y}As$ MBL on GaAs was observed at 4.72 µm [22]. Moreover, 3.6 µm emission wavelength was observed by electroluminescence (EL) measurement from the mesa formed of the growth of one stage of a QCL on a step-graded $In_xGa_{1-x}As$ MBL [22]. With further design optimization to push the emission wavelength below 3.5 µm [23], ten stages of a QCL active region have been successfully grown on the $In_xGa_{1-x}As$ MBL [24]. This motivates the efforts to achieve short-wavelength mid-IR QCLs (λ=3.0-3.5 µm) on MBLs.

III-V material substrates such as GaAs and InP are expensive and MBLs grown on Si provide an opportunity to reduce those costs while realizing III-V integration with Si photonics. A variety of MBLs have been grown in the thick single layer technique by Lau et al. [25]–[27]. These substrates provided by them will be utilized to understand the differences in growth and performance of QCLs (λ=4.8 µm) grown on InP MBLs in comparison to those grown on InP substrates.

QCL designs are found to be sensitive to 1 Å changes in well or barrier thicknesses, more so in the layers where the lasing transition occurs. Therefore, in parallel, there is an effort to understand compositional grading at the interfaces in the active region as they could have a large

impact on the calculated wavefunctions in the conduction band, and the subsequent device characteristics. This involves the growth of test structures and characterization of interfaces using atom probe tomography (APT), atomic force microscopy (AFM), x-ray diffraction (XRD), transmission electron microscopy (TEM) and electroluminescence (EL).

1.4 Organization

The first chapter introduces the current state of the art QCLs and their device performance along with providing the motivation to grow QCLs on MBLs.

The second chapter will elaborate on the active region design for a QCL with an emission wavelength (λ~3.4 µm), along with thermal and optical modeling of the cladding layers. Hydride vapor phase epitaxy (HVPE) grown $In_xGa_{1-x}As$ MBLs are the virtual substrates used for the growth of 10-stage and 30-stage core region. These are characterized XRD, reciprocal space maps (RSM), Nomarski optical microscopic images, AFM and TEM.

The third chapter focuses on III-V integration with Si through QCLs designed for an emission wavelength of 4.8 µm. In collaboration with Hong Kong University of Science and Technology (HKUST), three kinds of InP MBLs grown on Si substrates are analyzed for their suitability as substrates for QCL growth. SL and QCL active region growths are used as test structures to determine the best InP MBL candidate.

The fourth chapter probes the importance of interface analysis for strained layers employed in QCLs and the application of atom probe tomography (APT) to better understand compositional intermixing at the interfaces.

Chapter five summarizes this work and suggests some future directions this work can take. The first being interface analysis using AFM, APT, XRD and TEM for SLs and QCLs

implementing various growth conditions. The second direction would be the growth of the optimized QCL design (λ~3.4 µm) on an $In_xGa_{1-x}As$ MBL.

References

[1] L. Shterengas, G. Belenky, T. Hosoda, G. Kipshidze, and S. Suchalkin, "Continuous wave operation of diode lasers at 3.36 µm at 12 °C," *Appl. Phys. Lett.*, vol. 93, no. 011103, 2008.

[2] L. Shterengas, G. Kipshidze, T. Hosoda, J. Chen, and G. Belenky, "Diode lasers emitting at 3 m m with 300 mW of continuous-wave output power," *Electron. Lett.*, vol. 45, no. 18, 2009.

[3] T. Hosoda, G. Kipshidze, L. Shterengas, and G. Belenky, "Diode lasers emitting near 3.44 µm in continuous-wave regime at 300K," *Electron. Lett.*, vol. 46, no. 21, 2010.

[4] I. Vurgaftman *et al.*, "Mid-infrared interband cascade lasers operating at ambient temperatures," *New J. Phys.*, vol. 11, no. 125015, 2009.

[5] I. Vurgaftman *et al.*, "Interband cascade lasers with low threshold powers and high output powers," *IEEE J. Sel. Top. Quantum Electron.*, vol. 19, no. 4, 2013.

[6] I. Vurgaftman *et al.*, "Interband cascade lasers," *J. Phys. D. Appl. Phys.*, vol. 48, no. 123001, pp. 1–17, 2015.

[7] W. W. Bewley *et al.*, "Lifetimes and Auger coefficients in type-II W interband cascade lasers," *Appl. Phys. Lett.*, vol. 93, no. 041118, pp. 1–3, 2008.

[8] D. A. Firsov *et al.*, "Dynamics of photoluminescence and recombination processes in Sb-containing laser nanostructures," *Semiconductors*, vol. 44, no. 1, pp. 50–58, 2010.

[9] D. Botez, "Design considerations and analytical approximations for high continuous-wave power, broad-waveguide diode lasers," *Appl. Phys. Lett.*, vol. 74, no. 21, pp. 3102–3104, 1999.

[10] D. Botez, J. C. Shin, S. Kumar, L. J. Mawst, I. Vurgaftman, and J. R. Meyer, "Electron leakage and its suppression via deep-well structures in 4.5- to 5.0-µm-emitting quantum cascade lasers," *Opt. Eng.*, vol. 49(11), no. 111108, 2010.

[11] D. Botez, C. C. Chang, and L. J. Mawst, "Temperature sensitivity of the electro-optical characteristics for mid-infrared (λ = 3-16 µm)-emitting quantum cascade lasers," *J. Phys. D. Appl. Phys.*, vol. 49, no. 043001, pp. 1–33, 2016.

[12] J. C. Shin *et al.*, "Highly temperature insensitive, deep-well 4.8 µm emitting quantum cascade semiconductor lasers," *Appl. Phys. Lett.*, vol. 94, no. 20, pp. 1–4, 2009.

[13] T. F. Kuech *et al.*, "Metamorphic and non-conventional `buffer' layers," *2011 Compd. Semicond. Week 23rd Int. Conf. Indium Phosphide Relat. Mater.*, p. 4, 2011.

[14] J. E. Ayers, T. Kujofsa, P. Rago, and J. E. Raphael, “Relaxation II. Graded Layers and Multilayered Structures,” in *Heteroepitaxy of Semiconductors:Theory, Growth, and Characterization*, 2nd ed., Boca Raton, Florida: CRC Press, 2017.

[15] A. Sacedón *et al.*, “Design of InGaAs linear graded buffer structures,” *Appl. Phys. Lett.*, vol. 66, no. 24, pp. 3334–3336, 1995.

[16] K. E. Lee and E. A. Fitzgerald, “High-quality metamorphic compositionally graded InGaAs buffers,” *J. Cryst. Growth*, vol. 312, no. 2, pp. 250–257, 2010.

[17] G. Salviati *et al.*, “TEM and X-ray diffraction studies of III-V lattice mismatched multilayers and superlattices,” *Inst. Phys. Conf. Ser. No 146*, pp. 337–348, 1995.

[18] H. Ji-Fang *et al.*, “GaAs-based long-wavelength InAs quantum dots on multi-step-graded InGaAs metamorphic buffer grown by molecular beam epitaxy,” *J. Phys. D. Appl. Phys.*, vol. 44, no. 335102, pp. 1–5, 2011.

[19] G. R. Nash *et al.*, “Midinfrared GaInSb/AlGaInSb quantum well laser diodes operating above 200 K,” *Appl. Phys. Lett.*, vol. 94, no. 091111, pp. 1–3, 2009.

[20] Y. Gu *et al.*, “InP-based type-I quantum well lasers up to 2.9 μm at 230 K in pulsed mode on a metamorphic buffer,” *Appl. Phys. Lett.*, vol. 106, no. 121102, pp. 1–4, 2015.

[21] J. Kirch *et al.*, “InAsyP1-y Metamorphic Buffer Layers (MBLs) on InP Substrates for Mid-IR Diode Lasers,” *OSA/CLEO/IQEC*, vol. CTuGG6, pp. 6–7, 2009.

[22] L. J. Mawst *et al.*, “Low-strain, quantum-cascade-laser active regions grown on metamorphic buffer layers for emission in the 3.0–4.0 μm wavelength region,” *IET Optoelectron.*, vol. 2013.0060, no. 10.1049, pp. 1–8, 2013.

[23] A. Rajeev, C. Sigler, T. Earles, Y. V Flores, L. J. Mawst, and D. Botez, “Design considerations for λ ~ 3.0-to 3.5-μm-emitting quantum cascade lasers on metamorphic buffer layers,” *Opt. Eng.*, vol. 57, no. 1, p. 011017(1-10), 2017.

[24] A. Rajeev *et al.*, “Regrowth of quantum cascade laser active regions on metamorphic buffer layers,” *J. Cryst. Growth*, vol. 452, pp. 268–271, 2016.

[25] Q. Li, X. Zhou, C. W. Tang, and K. M. Lau, “Material and Device Characteristics of Metamorphic In0.53Ga0.47As MOSHEMTs Grown on GaAs and Si Substrates by MOCVD,” *IEEE Trans. Electron Devices*, vol. 60, no. 12, pp. 4112–4118, 2013.

[26] B. Shi, Q. Li, and K. M. Lau, “Self-organized InAs/InAlGaAs quantum dots as dislocation filters for InP films on (001) Si,” *J. Cryst. Growth*, vol. 464, pp. 28–32, 2017.

[27] J. Norman *et al.*, “Electrically pumped continuous wave quantum dot lasers epitaxially grown on patterned, on-axis (001) Si,” *Opt. Express*, vol. 25, no. 4, pp. 3927–3934, 2017.

Chapter 2 λ~ 3.4 µm QCLs on InGaAs Metamorphic Buffer Layers

2.1 Introduction

The strain limitations imposed by the constituent materials are in direct conflict with one of the foremost requirements for QCLs in the 3.0 to 3.5 µm wavelength regime, which is to have large conduction band (CB) offsets between wells and barriers in order to accommodate the high transition energies. Even if strain relaxation is not present, high strain affects the interface morphology [1], [2] in the active regions (ARs) of the stages of the QCL core region, which, in turn, is expected to impact the device performance. InP-based 3.56 µm emitting QCLs [3] have demonstrated high CW output power (0.5 W), although such devices utilize $In_xGa_{1-x}As/In_yAl_{1-y}As$-superlattice (SL) ARs of highly strained ($\Delta a/a$ ~ 2%) QWs and barriers. While relatively high T_0 (threshold-current characteristic temperature coefficient) values (152 to 166 K) were obtained, the T_1 (slope efficiency characteristic temperature coefficient) value was moderately high (~190 K) only for 3.56 µm emitting devices, as it dropped to ~116 K for 3.39 µm emitting devices, most likely due to the onset of leakage to satellite valleys [4]. Similarly, 3.3 µm emitting devices [5] have displayed low T_1 values (~71 K), over the 250 to 300 K temperature range, indicating strong carrier leakage to satellite valleys. The T_0 values were also found to be low (100 K) above an operating temperature of 250 K, due to carrier leakage and possibly strong backfilling, considering the relatively high injector-doping level. Even higher strain ($\Delta a/a$ ~ 3%) barriers have been used to enable the emission wavelength to be as short as 3.0 µm, [6] although very low T_0 and T_1 values limited the CW output power to quite low values (~2.5 mW). Such poor performance was most likely due to strong carrier leakage to satellite valleys (L, X) for ~3.05 µm emitting devices grown on InP [7].

We propose the use of metamorphic buffer layers (MBLs) as the means to achieve high-performance low-strain QCLs at 3.0 to 3.5 μm emission wavelengths [8], [9]. These "virtual substrates" under consideration were grown on (001) GaAs substrates by hydride vapor phase epitaxy [10]. They consisted of nine $In_xGa_{1-x}As$ layers with linear grading of the In content in each of the nine ~1.0 μm thick steps. The final layer was a constant-composition cap layer which is typically ~15 μm thick to allow for surface preparation in order to perform the regrowth of strained layers atop with high fidelity [9]. The MBL cap is found to be nearly fully relaxed (>95%), owing to its thickness, and exhibits tilt with respect to the substrate, which is a function of composition and thickness [2], [10]. The MBL enables trapping of misfit dislocations at the composition steps while forcing the threading dislocations (TDs) to glide to the edges of the sample, thus giving us a virtual substrate with a threading-dislocation density (TDD) of the order of ~10^5 cm^{-2}. However, the induced strain relaxation in the MBL results in a cross-hatched surface morphology which is detrimental to QCL-device performance. The use of chemical–mechanical planarization (CMP) with appropriate applied pressure on the MBL cap was found to reduce the cross-hatching height by more than 20 times [11]. A single stage of the QCL structure grown atop an MBL, which had undergone the chemical mechanical planarization (CMP) treatment, did result in electroluminescence (EL) emission near 3.6 μm wavelength from mesa devices tested at 80 K [10]. However, indium enrichment was observed in the MBL cap layer when heated to high regrowth temperatures. An additional wet-chemical etching step introduced after the CMP alleviates the indium segregation, as will be shown in this work. To enable growth of the complete laser design, several challenges remain such as the choice of cladding material and optical-waveguide design, which are being addressed in this study. Moreover, the structural, thermal, and optical

characteristics of the ternary cladding material, with specific compositions that are lattice-matched to the MBL, have not been previously reported.

A direct consequence of using MBLs is the expansion of the design space for QCLs emitting at mid-IR wavelengths by having an application-oriented custom-grown substrate, also known as a virtual substrate. Here, we perform a comprehensive design optimization of a particular AR design based on an MBL employing an $In_{0.22}Ga_{0.78}As$ cap layer. A thermo-optical analysis for the complete laser design indicates that the use of $In_xAl_{1-x}As$ cladding layers allows for both good optical confinement and adequate heat transport. CMP followed by wet-chemical etching of the MBL, is shown here to allow for the regrowth of highly-planar strained-layer SL structures applicable to QCLs. Ten and thirty stages of the QCL structure of this AR design for 3.4 µm emission target wavelength were grown on an MBL using an optimized surface treatment. Fidelity of the constituent SL is analyzed using x-ray diffraction and transmission electron microscopy.

2.2 Quantum Cascade Laser Design

2.2.1 Quantum Cascade Laser Active-Region Design

To analyze the design of the QCL ARs grown on MBLs, the energy-band structure, electronic wavefunctions, and electron energy-state lifetimes have been calculated using an 8-band $k \cdot p$ code, as previously reported [8]. Conventional QCL structures utilize fixed compositions for the wells and barriers with variations only in the thickness of each layer type. For such QCLs, it has been found [12] that for 3.76 µm emitting devices [13] one can achieve both efficient carrier leakage suppression and fast, miniband-like carrier extraction when using, for lower-laser-level depopulation, the single-phonon-resonance (SPR) AR structure in conjunction with resonant-tunneling extraction from the lower laser level [14]. We have achieved the same type of AR design (i.e., SPR + miniband extraction) for our short-wavelength (λ= 3.0 to 3.5 µm) QCL structures

grown on MBLs. More specifically, an SPR + miniband extraction AR design was reached given a lattice constant of 0.574 nm for the virtual substrate (i.e., the cap layer of the MBL) so as to provide a relatively low-strain QCL structure for emission in the 3.0 to 3.5 μm wavelength range. Such a design, based on an MBL cap composition of $In_{0.22}Ga_{0.78}As$, with a 10-stage core region consisting of AlAs barriers and $In_{0.45}Ga_{0.55}As$ wells, and designed to emit at 3.39 μm has been grown by using metalorganic chemical vapor deposition (MOCVD) of high crystalline quality [9]. The layers thicknesses (expressed in Å) within one stage of the QCL core region are as follows: **25**/16/**24**/17/*21/18/****20****/21*/**19**/21/**18**/18/**17**/28/**12**/13/**39**/10/**33**/16. The bold-faced layers are the wells and the other layers are barriers, with the doped layers (n-type, $2\times10^{17}cm^{-3}$) indicated by italics. Figure 2.1 shows the CB diagram and relevant electronic wavefunctions for this design at the indicated applied electric field.

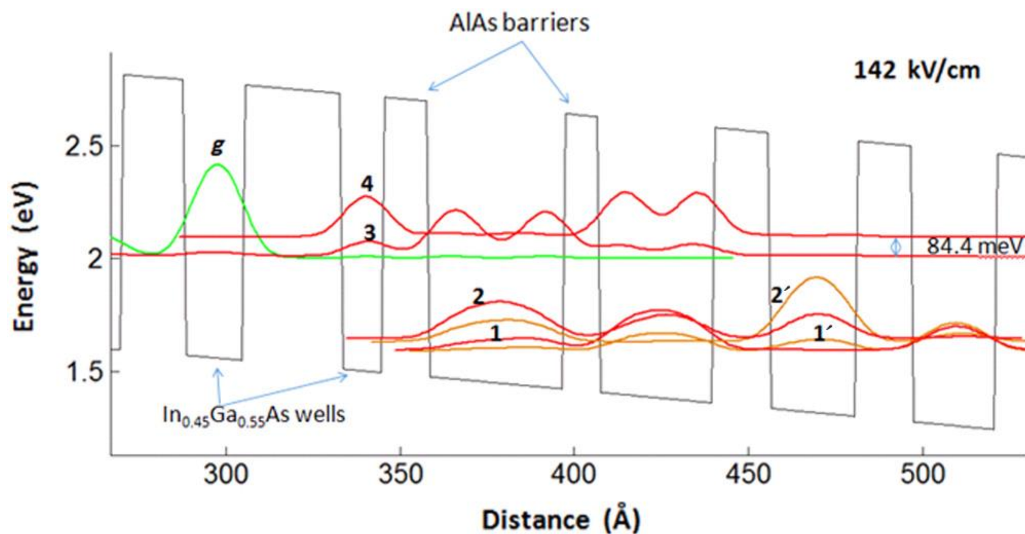

Figure 2.1 CB diagram and modulus squared of the most relevant wavefunctions shown at the operating electric field at threshold (142 kV/cm) for a 3.39 μm emitting, SPR + miniband-extraction QCL design grown on an $In_{0.22}Ga_{0.78}As$ MBL cap layer. The primed numbers identify wavefunctions from the extractor region that penetrate into the AR.

2.2.2 Complete Quantum Cascade Laser Structure: Thermo-Optical Analysis

The AR modeling is followed by the 1-D optical analysis of the complete laser structure shown in figure 2.2. This makes use of a wave-transfer matrix method for TM-polarized light. Using the refractive-index profile of this structure (table 2.1), the wave-transfer matrix method [15] is employed to analyze the optical confinement and mode profiles obtained. We consider two different cladding materials, $In_xAl_{1-x}As$ and $In_xGa_{1-x}P$, since both materials can be lattice matched to the MBL and have refractive indices lower than the average refractive index of the SL core region.

As the MBL cap is ~10 µm thick and nearly fully relaxed, for all simulations, the constant composition in the cap (i.e., $In_{0.22}Ga_{0.78}As$) is treated as a substrate. The upper and lower-cladding layers are grown lattice matched to the MBL cap and consist of either $In_{0.21}Al_{0.79}As$ or $In_{0.69}Ga_{0.31}P$. The upper and lower optical-confinement layers are $In_{0.22}Ga_{0.78}As$. The QCL core region comprises 30-stages, with the layer thicknesses and doping levels for a stage described above. The last semiconductor layer grown is a highly n-type-doped contact/ plasmon layer, which is $In_{0.21}Al_{0.79}As$ or $In_{0.69}Ga_{0.31}P$. An additional thin, highly doped $In_{0.22}Ga_{0.78}As$ contact layer could be grown on top to provide a low-resistance ohmic contact, although this is not included in the model for simplicity. This is followed by Ti/Au metal contact layers.

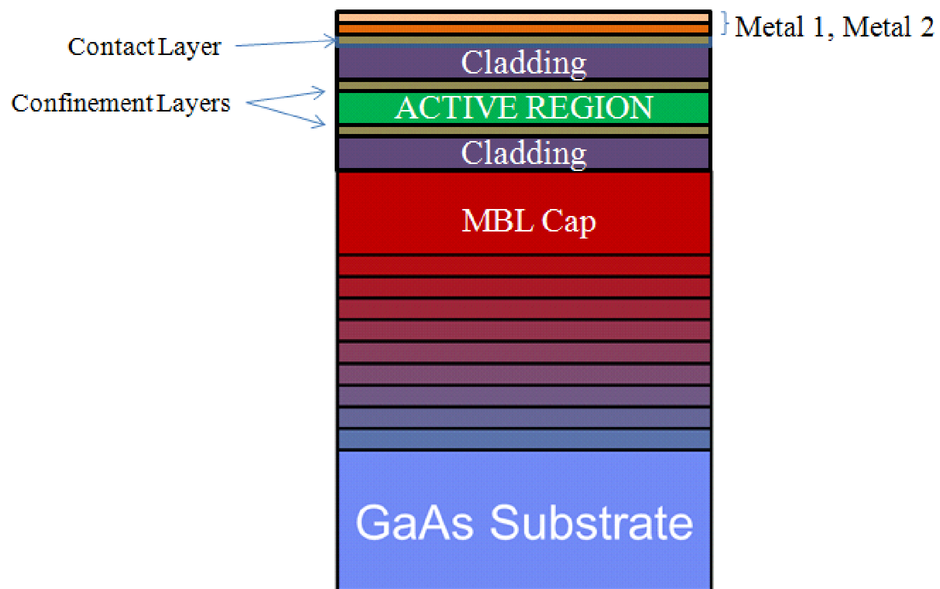

Figure 2.2 Complete laser structure showing the upper and lower optical confinement layers and the cladding layers.

Layer Name	Composition/ Doping	Refractive Index (n)
MBL Cap	$In_{0.22}Ga_{0.78}As/2\times10^{17}\ cm^{-3}$	3.347
Lower/Upper Cladding	$In_{0.21}Al_{0.79}As/\ 2\times10^{16}\ cm^{-3}$	2.993
	$In_{0.69}Ga_{0.31}P/\ 2\times10^{16}\ cm^{-3}$	3.075
Lower/Upper Confinement	$In_{0.22}Ga_{0.78}As/\ 4\times10^{16}\ cm^{-3}$	3.346
Active Region	Section 2.1	3.158
Contact Layer	$In_{0.21}Al_{0.79}As/\ 5\times10^{18}\ cm^{-3}$	2.918
	$In_{0.69}Ga_{0.31}P/\ 5\times10^{18}\ cm^{-3}$	2.967

Table 2.1 List of material parameters employed for thermo-optical analysis of the complete laser structure. Only the real parts of the refractive indices are noted here, although imaginary parts will be used for the calculation of losses as discussed below.

The Drude model [16], [17] is employed to determine the refractive indices of each of these layers for an emission wavelength of 3.4 µm. Specifically, for the core region, the refractive index

is obtained by averaging over 30 stages of alternating well and barrier layers and also taking into account the injector layers that are intentionally doped. Refractive indices for the metal layers are obtained from Refs [18], [19].

The thermal analysis for the structure is conducted using the heat transfer module of the COMSOL Multiphysics™ software package. Steady-state equations are employed for analyzing the thermal dissipation under CW operation of the QCL. For simulation purposes, the QCL is considered to be processed to form ridge waveguides 10 µm wide. A two-step gold electroplating process would be employed to fill in the trenches and obtain a planar top surface for mounting [20]. The chip would be mounted in epi-down fashion using 4 µm thick indium solder on a 300 µm thick diamond submount already bonded to a copper heatsink, which will be 1.5 mm thick and 3 cm wide. The boundary conditions for the packaged chip are set as room temperature for the bottom of the heatsink, with the other boundaries being adiabatic. The thermal conductivities are listed for all the materials involved in fabricating and packaging this laser, providing the temperature dependences where known (table 2.2). The challenge, as stated earlier, is to estimate the appropriate value of thermal conductivities for the two cladding-layer options for this QCL design: $In_{0.21}Al_{0.79}As$ and $In_{0.69}Ga_{0.31}P$. The dependence of thermal resistivity of a ternary alloy on the binary-compound resistivities is as follows: [21]

$$T_{A_xB_{1-x}C}(x) = xB_{AC} + (1-x)B_{BC} + C_{A-B}x(1-x) \quad 2.1$$

where C_{A-B} is the bowing parameter owing to the lattice disorder originating from the random distribution of A and B atoms on the interchangeable sublattice sites.

Layer Name	Composition	Thermal conductivity (W/m.K)
MBL Cap [21], [22]	$In_{0.22}Ga_{0.78}As$	6.694
Lower/Upper Cladding [21], [23]	$In_{0.21}Al_{0.79}As$	8.621
	$In_{0.69}Ga_{0.31}P$	5.946
Lower/Upper Confinement [21], [23]	$In_{0.22}Ga_{0.78}As$	6.694
Core Region[24]	Section 2.1	$k_{//}=5.3-3.9\times10^{-3}T+5.3\times10^{-7}T^2$ $k_{\|}=2.3$
Plasmon/ Contact Layer [21], [23]	$In_{0.21}Al_{0.79}As$	8.621
	$In_{0.69}Ga_{0.31}P$	5.946
Gold [24]		$337 - 660\times10^{-4}T$
Titanium [24]		$31.46 - 4.338\times10^{-2}T + 4\times10^{-5}T^2$
Copper [24]		$349+14710T^{-1}$
Diamond [25]		1800
Indium Solder [24]		$1.9 - 6.96\times10^{-2}T + 9.86\times10^{-5}T^2$

Table 2.2 List of the material parameters employed for thermal analysis of the complete laser structure. The room-temperature estimated thermal conductivity is provided where the temperature dependence is not well-known.

C_{In-Ga} has been calculated to be 72 W^{-1} deg cm at room temperature from fitting the thermal resistivity data of InAs-GaAs alloys and is assumed to be the same for InP-GaP alloys. This bowing parameter results in thermal resistivities that are in good agreement with those experimentally determined for $In_xGa_{1-x}P$ layers of different x concentration [26], [27].

The disorder alloy-bowing parameter for InAlAs is estimated to be 60 W^{-1} deg cm [23]. These are yet to be confirmed experimentally. The thermal resistivities for the binary alloys under consideration, namely InAs, AlAs, InP and GaP, have all been well characterized [21]. The

anisotropic thermal conductivity for the core region is assumed to be close to that obtained for a conventional 4.6 μm emitting QCL [24]. This is expected to suffice for the purpose of comparing the effectiveness of using InAlAs versus InGaP as cladding-layer materials.

2.3 Experimental Details

The MBLs employed for the QCL-device structures were grown by hydride vapor phase epitaxy (HVPE). The $In_xGa_{1-x}As$ MBLs were grown on (001) GaAs substrates with nine individual layers, each being ~1.0 μm thick and consisting of a fixed In content which was incremented in steps from layer to layer. Finally, the tenth layer of final uniform composition (here: $In_{0.23}Ga_{0.77}As$) and ~15 μm thickness is grown on the top, commonly referred to as the cap layer [28]. The buffer structure allows the formation of misfit dislocations as a means to relieve film stress while minimizing threading dislocations. The MBLs were characterized using high-resolution X-ray diffraction (HR-XRD) and reciprocal space mapping (RSM). The MBL cap is found to be nearly fully relaxed (~95%) owing to the thickness and can exhibit a crystallographic tilt with respect to the substrate, which is a function of composition and thickness [2], [10]. The MBL's InGaAs top layer of constant Indium composition displays some pits, hillocks, and crosshatching. CMP employing a solution of 4% bleach and 96% silica nanoparticle slurry (50 weight% silica) was used to planarize the MBL surface by removing approximately 4–5 μm of material from the cap layer. The MBLs were cut into 1 cm^2 pieces and mounted on a 2″ Si wafer. The applied pressure on the samples, besides the polishing solution, was the main determinant of the polishing rate and surface morphology. The CMP process optimization for ternary materials such as the InGaAs MBL cap layer is discussed in detail in [11]. After polishing, $In_xGa_{1-x}As/Al_yIn_{1-y}As$ strained-layer SL structures were grown by MOCVD on the prepared HVPE-grown MBL. Details of the MOCVD growth have been published previously [10]. The resulting SL structures were characterized by

HR-XRD RSM, transmission electron microscopy (TEM) imaging and atomic force microscopy (AFM) surface imaging.

Currently, we grow the MBLs by MOCVD in order to obtain high repeatability and full wafers with uniform MBL structures. The growth temperature is 700 °C, reactor pressure 100 Torr and wafer rotation is 100 rpm. Conventional sources trimethyl gallium ($(CH_3)_3Ga$, TMGa), trimethyl indium ($(CH_3)_3In$, TMIn), trimethyl aluminum ($(CH_3)_3Al$, TMAl), arsine (AsH_3) and phosphine (PH_3) were used for the growths as mentioned above. These MBLs are step-graded from GaAs to $In_{0.22}Ga_{0.78}As$ in steps of 1% In keeping the misfit%/µm constant [29]. Additionally, high growth rate MBLs (~10 µm/hr) are also being grown by MOCVD and characterized for etch pit dislocation densities and surface roughnesses for various growth temperatures and miscut substrates. Moreover, a new mask set has been designed to fabricate both contacts on the top side such that losses while flowing current through the MBL, are avoided.

2.4 Results and Discussion

2.4.1 HVPE-MBL Surface Preparation

AFM measurements indicate that the RMS surface roughness of the MBL can be reduced by more than a factor of 2.5 using CMP on the as-grown MBLs which lessens the cross-hatch features and hillocks [30]. The samples subjected to CMP possessed a mound-like surface morphology, shown in figure 2.3 (b), after being heated within the MOCVD reactor under AsH_3/H_2 at temperatures ranging from 500 °C to 650 °C. Upon characterization with scanning electron microscopy (SEM) using a backscatter electron detector and X-ray photoelectron spectroscopy (XPS), these mound-like features were found to possess higher mass density than the surrounding material as well as an increased In/Ga ratio. Analysis using TEM in the {220} dark field condition confirmed the

mound-like features to be In-rich $In_xGa_{1-x}As$ hillocks. The In enrichment changes the local lattice parameter and subsequent growth leads to lattice mismatch-based defects propagating into the subsequently grown layer. This is evident from the bright field diffraction contrast TEM image of an MOCVD-grown strained-layer superlattice with $In_xGa_{1-x}As$ wells/ $Al_yIn_{1-y}As$ barriers on top of the MBL [11]. An increase in the full width half maximum (FWHM) of the SL XRD fringes, when compared to the regrowth on an as-grown MBL, was also observed [11], [30]

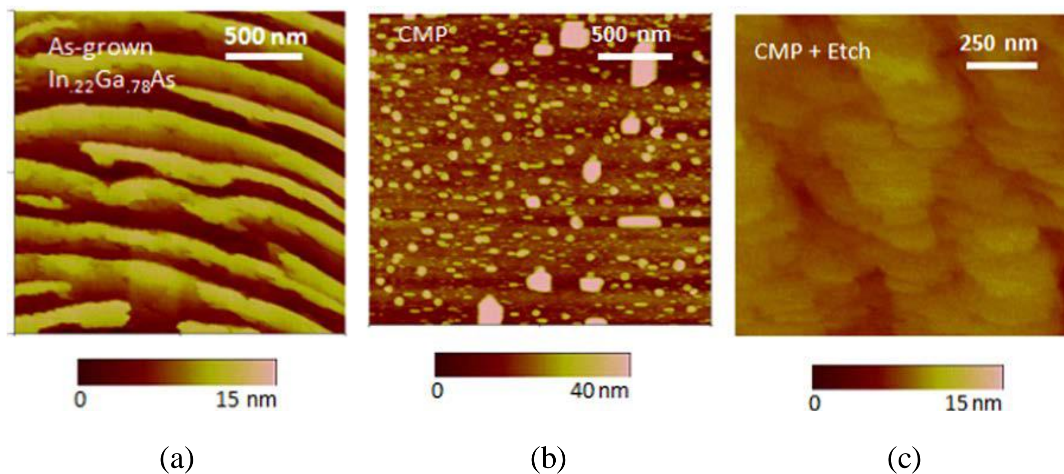

Figure 2.3 AFM measurements showing surface morphology of MBLs post annealing treatment at 630 °C (a) As-grown,(b) CMP treatment applied,(c) CMP and Wet-etching treatment applied.

The In segregation found after annealing was mitigated by employing a post CMP wet-chemical etch. Prior to growth on the MBL, the MBL was wet-etched in an H_2O:H_3PO_4:H_2O_2 (38:1:1) solution for one minute which removes residual damage from the surface that had been introduced by the CMP [11]. As can be seen in figure 2.3 (c), the CMP/wet-etched MBL has a different morphology but no strong indication of the In-enriched surface features after annealing at a high temperature of 630 °C.

2.4.2 QCL design

Key parameters used in determining the device performance, for the 3.39 μm emitting AR design shown in figure 2.1, are listed in table 2.3. For this optimized AR design, resonant-tunneling

extraction (to the next injector region) occurs from both the lower laser level (state 2) and the state below it (state 1), which constitutes miniband-like extraction [12]. In turn, as evident from table 2.3, the lower-laser-level global lifetime [31] $\tau_{22'g}$ (0.195 ps) is basically half the value of that for the SPR-only 3.56 μm emitting QCLs grown on InP [3] (i.e., 0.397 ps). As a result, the room-temperature slope efficiency is expected to be significantly higher, due to both higher laser-transition differential efficiency, [12], [14] and, as discussed below, less carrier leakage, just as in the case of SPR + miniband extraction, 3.76 μm emitting QCLs [13] versus SPR-only, 3.56 μm emitting QCLs [3].

The upper-laser-level global lifetime τ_{3g} requires a delicate balance of maximizing its value (often easily obtained by having extended wavefunctions throughout the AR and beyond) with the opposing need for a highly vertical laser transition. Keeping the ratio of upper laser levels' lifetimes and lower laser levels' lifetimes relatively large enables effective population inversion. In structures with resonant extraction from the lower laser, level both that level (state 2 in this case) and the extractor level (state 2′) are considered for the lasing transition [14]. Thus, the dipole matrix element is a global one, z_{32g}, taking into account transitions from both (energy) levels 3 to 2 and from levels 3 to 2′, and signifies the degree of overlap between the corresponding wavefunctions. τ_{32g}, the global lifetime for the laser transition, needs to be maximized such that the global, effective upper-level lifetime [31] converges to τ_{3g} as the lifetime ratio $\tau_{22'g}/\tau_{32g}$ approaches zero.

3.39 µm design on $In_{0.22}Ga_{0.78}As$ MBL	**3.56 µm design on InP** [3]
Operating Field = 142 kV/cm	194 kV/cm
E_{43} = 84.4meV	E_{43} = 65.1meV
Δ_{inj} = 226.41 meV	Δ_{inj} = 391.2 meV
z_{32g} = 11.09 Å	z_{32g} = 10.36 Å
τ_{3g}-= 1.156 ps	τ_{3g} = 1.904 ps
τ_{32g} = 1.81 ps	τ_{32g} = 3.521 ps
$\tau_{22'g}$ = 0.195ps	τ_{2g} = 0.397 ps
τ_{43} = 0.51 ps	τ_{43} = 0.548 ps
Average strain per stage = - 0.00284	+ 0.00148
Strain per barrier, well pair = +1.42 %, -1.61 %	+2.32 %, -1.85 %

Table 2.3 Key parameters for SPR + miniband extraction QCL-structure designs grown on an MBL: the operating field at threshold; the energy difference between the upper laser level, state 3, and the next higher AR energy state, state 4, E_{43}; the energy level separation between the lower laser states (states 2 and 2') and the ground state of the next-stage injector, Δ_{inj}; the dipole matrix element between the upper laser level and lower laser level, z_{32g}; the lifetime of transitions between state 4 and state 3, τ_{43}, the global lifetimes for the upper and lower laser states, τ_{3g} and $\tau_{22'g}$; the average strain per stage; and the strain of well and barrier layers. For comparison, we also show the same parameters for SPR-only QCLs on InP [3]

The figure of merit (FOM) using these critical parameters, for a first-order approximation of the threshold-current density, J_{th}, is as follows: [32]

$$FOM = \left|z_{32g}\right|^2 * \left\{\tau_{3g}\left(1 - \frac{\tau_{22'g}}{\tau_{32g}}\right)\right\} \quad 2.2$$

and since the backfilling current is negligible in both structures, due to very large values for the energy difference (at threshold) between the lower laser level, state 2, and the injector ground level, state g, in the next stage Δ_{inj} (table 2.3), one obtains

$$J_{th} \propto \frac{1}{FOM} \quad 2.3$$

The illustrated QCL design has a FOM value of 127.9 Å^{2}ps compared to the calculated value of 181.3 Å^{2}ps for the 3.56 µm QCL grown on InP [3]. However, the FOM values do not take into account the carrier leakage from the upper laser level, which, as discussed below, is significantly lower for our 3.39 µm QCL design on MBL than for the 3.56 µm emitting QCL design on InP. Thus, the actual difference between the achievable J_{th} values for the two devices will definitely be lower than indicated by the calculated FOM values.

The relatively large value for the energy difference between the upper laser level, state 3, and the next higher AR energy level, state 4, E_{43}, of the 3.39 µm QCL on MBL (i.e., 84.4 meV) will result in negligible carrier leakage through thermal excitation from state 3 to state 4 and consequent relaxation to the lower AR energy states (i.e., to 1, 1', 2, and 2') [33]. This will happen because the E_{43} value strongly impacts the scattering rate from state 3 to state 4 ($1/\tau_{34}$) and, in turn, the leakage current density J_{leak} [33]. The former is estimated as follows, given an electronic temperature T_{e3} in state 3: [34], [35]

$$\frac{1}{\tau_{34}} \approx \frac{1}{\tau_{43}} exp\left(-\frac{E_{43}}{kT_{e3}}\right) \quad 2.4$$

To reduce the scattering rate into the upper AR energy states (i.e., $1/\tau_{34}$), we designed QCLs with large E_{43} and τ_{43} values. The resulting design characteristics, related to the device performance, are reduced temperature sensitivities for the threshold-current density, J_{th}, and the slope efficiency, η, (i.e., higher T_0 and T_1 values) and subsequently increased maximum CW power, P_{max}, and maximum CW wallplug efficiency, $\eta_{wp,max}$, due to higher values for T_0 and especially higher values for T_1 [12], [31], [36]. From table 2.3, one can see that while the τ_{43} values are similar for the two compared devices, the E_{43} value is higher for 3.39 μm QCLs on MBL than for 3.56 μm QCLs on InP (i.e., 84.4 meV versus 65.1 meV). This is consistent with the fact that the E_{43} value generally decreases with increasing field strength; thus, given that the 3.56 μm QCLs on InP has a significantly higher field strength than our 3.39 μm device on MBL (i.e., 194 versus 142 kV/cm), the higher E_{43} value for the device grown on MBL is justified. Since, as seen from eq. 2.4, the scattering rate to the upper AR states is an exponential function of $-E_{43}$, the carrier leakage will be significantly lower for 3.39 μm QCLs on MBL than for 3.56 μm QCLs on InP. We note that for these 3.4 μm emitting QCLs on MBL we have been able to achieve both carrier leakage suppression as well as miniband-like extraction without the need for deep QWs in the AR [14], [37] or tapered barrier heights in the AR [12], [14], [31]. In addition, carrier leakage to satellite valleys (L, X) is also substantially reduced owing to the lower In percentage in QWs (i.e., 45%) for this QCL on MBL when compared to conventional QCLs grown on InP substrates for the wavelength range being studied (e.g., 80% for 3.56 μm emitting QCLs [3] and 72% for 3.3 μm emitting QCLs [5]). As pointed out above in sec. 2.1, with increasing strain, which means with increasing In content in the QWs, such leakage becomes a significant portion of the total room temperature J_{th} value for devices grown on InP, unlike devices designed for emission in the 3.5 to 4.0 μm range [4], [38], [39].

Large Δ_{inj} values, like the ones in table 2.3, ensure that the backfilling-current density due to thermal excitation from the ground state in the injector region of a stage to the lower laser level in the AR of the previous stage is minimized. However, a trade-off exists here as too large a value for Δ_{inj} will result in undesirably high voltages. Note that the QCL design on MBL presented in table 2.3 has a significantly lower Δ_{inj} value compared to that for the QCL design on InP. This will result in a reduction in operating voltage, yet the Δ_{inj} value is large enough to minimize carrier backfilling, as further discussed below.

Other important characteristics for this design are a low average strain per stage (here: net compressive) and a fairly vertical lasing transition from state 3 to state 2, as seen in the AR band diagram (figure 2.1). Moreover, it is important to note that these specific compositions would result in +3.54% strain in the wells and +0.558% strain in the barriers if the SL would have been grown on InP. That is, the QW strain value would be extremely large in addition to the fact that both wells and barriers would be tensilely strained, thus ineffective in achieving strain compensation in the AR. We also note that the degree of strain balancing is much better for the device grown on MBL than for the device grown on InP.

As shown in table 2.4, the limiting strain-thickness product for a barrier in the AR for this design is only 30% of that for the 3.0 μm emitting QCL on InP [6] and 56% of that for the 3.56 μm emitting QCL on InP [3]. Interestingly, the MBL based design also compensates extremely well the limiting strain-thickness product for the wells and barriers in the injector region. The significantly lower strain values for the MBL-based QCL designs, compared to those for conventional short-wavelength QCLs, alleviate the issues of strain relaxation and may ultimately lead to improved device reliability for 3.0 to 4.0 μm emitting QCLs.

		QCL on MBL (3.39 µm)	QCL on InP[6] (3.0 µm)	QCL on InP[3] (3.56 µm)
Injector Region	Well	-0.403	-0.445	-0.444
	Barrier	0.397	0.531	0.786
Active Region	Well	-0.629	-0.570	-0.612
	Barrier	0.184	0.614	0.324

Table 2.4: Strain × thickness products in units of Angstroms for the QCL design on MBL, compared with QCLs on InP substrate.

Optical-mode confinement analysis is performed by combining the designed core region with cladding and optical confinement layers forming the complete laser structure. The refractive-index steps between the $In_{0.21}Al_{0.79}As$ cladding layers and the core region are higher than when using $In_{0.69}Ga_{0.31}P$ cladding layers. Straightaway, this gives superior optical-mode confinement to the core region when using InAlAs cladding layers. The threshold-current density is calculated as follows: [12], [14]

$$J_{th} = \frac{\alpha_m + \alpha_{w,eff}}{\eta_{inj,tot}\Gamma g} = \frac{\alpha_m + \alpha_{w,sim} + \alpha_{isb,bf}}{\eta_{inj}\eta_p\Gamma g} \qquad 2.5$$

where α_m is the mirror loss, $\alpha_{w,sim}$ is the simulated loss that includes free-carrier absorption losses and radiation leakage loss to the substrate owing to the antiguided nature of the transverse waveguide in the structure, $\alpha_{isb,bf}$ is the sum of ISB absorption losses in the injector regions and the equivalent loss corresponding to backfilling, $\eta_{inj,tot}$ is the total injection efficiency, η_{inj} is the tunneling-injection efficiency into the upper laser level, η_p is the pumping efficiency which reflects the degree of carrier leakage (i.e., $\eta_p = 1 - J_{leak}/J_{th}$), Γ is the (transverse) optical-mode confinement factor to the core region, and g is the differential gain in the case of unity tunneling-injection efficiency and no carrier leakage [12].

The loss term $\alpha_{isb,bf}$ can be considered to be negligible for these devices for the following reasons: (1) the ISB absorption, a measure of optical losses in the injector regions due to absorption between minibands, drops fast with emission wavelength (i.e., from ~2.3 cm^{-1} at λ = 8.8 μm [14] to ~0.5 cm^{-1} at λ =4.6 μm [40]) since with increased CB offset the injector-region minibands are further apart energywise, thus, since for our case the CB offset is significantly larger than for 4.6 μm emitting devices, the ISB absorption will become negligible; (2) the backfilling current density, J_{bf} , will be negligible since the Δ_{inj} value is rather large (i.e., 226 meV) compared to values in the 120 to 150 meV range for 4.6 μm emitting QCLs and given that $J_{bf} \propto \exp(-\Delta_{inj}/kT_{eg})$ [12]. The device cavity length is taken to be 3 mm, and the reflectivities for the high-reflectivity (HR)-coated back facet and the uncoated front facet are taken to be 97% and 27%, respectively. The value for differential gain g is calculated using the expression for gain cross-section g_c [32] divided by Γ and multiplied by $\tau_{up,g}$, the global, effective upper-state lifetime [31], [32]

$$g = \tau_{up,g} \times \frac{4\pi e}{\varepsilon_0 n_{refr}\lambda} \frac{z_{32g}^2}{2\gamma_{32} L_p} \qquad 2.6$$

where $\tau_{up,g}$, accounting for population inversion and electrical pumping, is given as

$$\tau_{up,g} = \tau_{3g}\left(1 - \frac{\tau_{22'g}}{\tau_{32_g}}\right) \qquad 2.7$$

$2\gamma_{32}$ is the full-width half maximum (FWHM) broadening of the transition, as obtained from EL measurements, L_p is the thickness of one stage, λ is the emission wavelength of the QCL, and n_{refr} is the average refractive index for the AR as per the design.

We use the 4.6 μm emitting QCL by Lyakh et al. [41] as the standard device for comparison to our design, as far as the value of the $\eta_{inj,tot}$ g product, due to the similarity in crystal growth method employed (i.e., MOCVD) for the core region. First of all, for $\eta_{inj,tot}$, we consider a typical η_{inj} value of 0.97, and for η_p we take 0.85, since those devices had strong carrier leakage as

evidenced by a low T_1 value of 140 K [42] which we have shown [33] to correspond to $\eta_p \approx 0.85$ for conventional 4.6 to 4.7 µm emitting QCLs. Then $\eta_{inj,tot} = 0.82$. Further confirmation that 0.82 is a good estimate for the $\eta_{inj,tot}$ value is the relatively large discrepancy found by Maulini et al. [40] between calculated and experimental wallplug efficiency values [i.e., a factor of 0.77 that corresponds to ~0.80 for $\eta_{inj,tot}$ when taking into account the small deviation from linearity (~4%) of the pulsed L − I curve at drives corresponding to the maximum wallplug efficiency]. As for g, one can use the parameters provided in Ref. [41]with the exception of the $\tau_{up,g}$ value for which the lifetimes provided in Ref. [41] take into account only longitudinal optical phonon scattering; that is, only inelastic scattering. Fortunately, the same structure was studied in Ref. [42], and good agreement with experiment was found when $\tau_{4g,inelastic} = 1.1$ ps and $\tau_{4g,elastic} = 1.5$ ps. [The elastic part is primarily due to interface-roughness (IFR) scattering.] Then, the total global upper-state lifetime $\tau_{4g,tot}$ is 0.635 ps, that is, 1.73 times lower that $\tau_{4g,inelastic}$. Thus, the value for the $\eta_{inj,tot}$ g product calculated without considering elastic scattering: 14.7 cm/kA, reduces to a value of 6.97 cm/kA (when elastic scattering is considered). We note that this estimated value is in excellent agreement with the experimental value of 6.8 cm/kA; [41] thus, it gives us confidence that applying the same procedure will provide a reasonably accurate value for the $\eta_{inj,tot}$ g product, as needed in order to estimate the potential J_{th} values for 3.39 µm emitting QCLs on MBLs. The room-temperature J_{th} value for the 4.6 µm emitting QCL was 1.5 kA/cm^2 for a 40-stage core-region device [41]. We scaled it to 1.73 kA/cm^2 for direct comparison to 30-stage core-region devices. Moreover, when considering a 3 mm long cavity with one HR-coated back facet, the J_{th} value becomes 1.28 kA/cm^2 (see table 2.5). Having obtained good agreement between calculated J_{th} values and experimental results, the same estimation procedure is applied to the 3.39 µm emitting QCL-on-MBL design.

	4.6 µm QCL on InP [41]	**3.4 µm QCL on MBL**		
Lower Cladding Material/Thickness		2 µm InGaP	2 µm InAlAs	3 µm InAlAs
α_{sim} (cm^{-1})	-	2.559	1.786	0.811
Γ	0.67	0.48	0.641	0.691
J_{th} (kA/cm^2)	1.28	3.18	2.00	1.40
Lower Confinement (µm)	-	0.35	0.25	0.15
Upper Confinement (µm)	-	0.55	0.35	0.15

Table 2.5 Comparison of InGaP versus InAlAs as lower-cladding layers for 3.4 µm emitting QCLs, and of 3.4 µm emitting QCLs on MBL versus 4.6 µm emitting QCL.

An EL spectral linewidth, $2\gamma_{32g}$, of ~50 meV is expected, that is, a similar value as for ~3.76 µm emitting QCLs of similar QW and well strain (i.e., ~ ±1.5%) and same lower-level depopulation scheme (i.e., SPR + miniband extraction) [13]. As a matter of fact, the EL linewidth in mid-IR QCLs is primarily due to IFR scattering, [43] and we calculate a value of $2_{\gamma 32g}$ =54.6 meV for the 3.39 µm emitting QCL on MBL design. The calculated EL spectrum is shown in figure 2.4. The EL spectrum in this design will be primarily due to radiative transitions from level 3 into levels 2 and 2’ (figure 2.1). Furthermore, because of the lower optical dipole matrix element for the 3 to 2’ radiative transition compared to the 3 to 2 transition (4.5 versus 10.1 Å), the intensity of the 3 to 2’ EL component is reduced by a factor of ~5.1. The FWHM values of the individual EL spectra correspond to the IFR-induced inhomogeneous broadening values between the involved levels and are calculated as in Refs. [44], [45]

$$\gamma_{3,(2,2')}^{IFR} = \frac{\pi m_c}{\hbar^2} \Delta^2 \Lambda^2 \sum_i \Delta_{CB}^2 \left(\varphi_3^2(z_i) - \varphi_{(2,2')}^2(z_i)\right)^2 \qquad 2.8$$

where $m_c = 0.0472m_0$ is the conduction band effective mass in the $In_{0.45}Ga_{0.55}As$ quantum well material, $\Delta = 0.14$ nm is the in-depth roughness height and $\Lambda = 6$ nm is the in-plane roughness correlation length, $\Delta_{CB} = 1.2$ eV is the Gamma-valley conduction band offset for the $In_{0.45}Ga_{0.55}As$/AlAs heterointerface, and $\varphi_{3,(2,2')}(z_i)$ are the wavefunction amplitudes of the involved levels the ith interface. It is important to note that minimal adjustment of the roughness parameters (Δ, Λ) was used with respect to values reported in the literature, as for example in [46]. Specifically, we use $\Delta = 0.14$ nm and $\Lambda = 6$ nm, whereas $\Delta = 0.15$ nm and $\Lambda = 6$ nm was used in [46]. In our consideration, such fluctuations in the roughness parameters are expected in the analysis of samples from different labs/growth sources. Altogether, we find excellent agreement between calculated (54.6 meV) and expected (~ 50 meV) $2\gamma_{32g}$values.

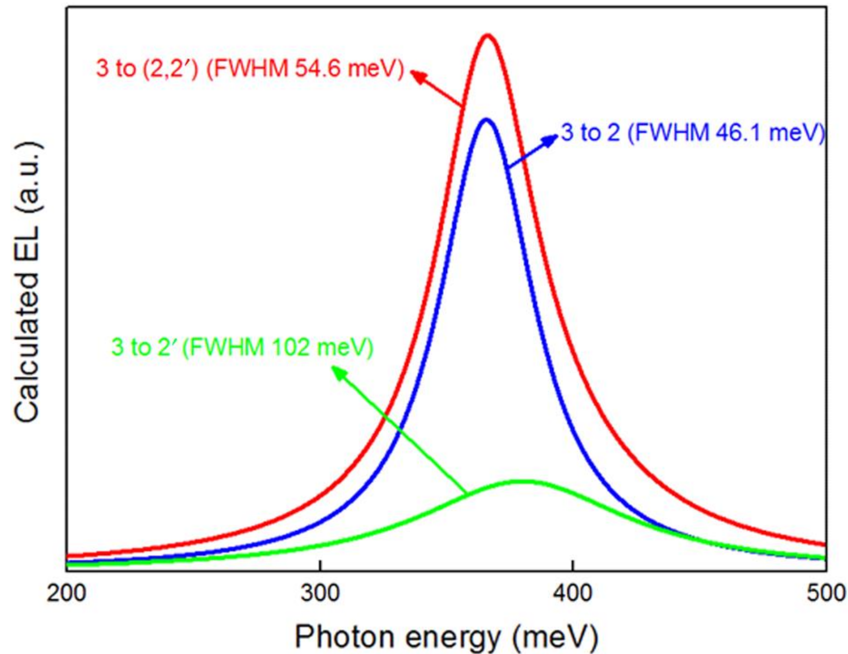

Figure 2.4 Calculated EL spectrum for the 3.39 μm emitting QCL on MBL design (figure 2.1). Inhomogeneous broadening due to IFR scattering has been considered for calculations.

Table 2.6 summarizes calculated scattering times for IFR-induced intersubband scattering between selected states of the 3.39 μm emitting QCL on MBL design. These values are calculated as in [46]

$$\frac{1}{\tau_{m,n}^{IFR}} = \frac{\pi m_c}{\hbar^3}\Delta^2\Lambda^2\sum_i \Delta_{CB}^2\,\varphi_m^2(z_i)\varphi_n^2(z_i)\exp\left(\frac{-\Lambda^2 m_c E_{mn}}{2\hbar^2}\right) \quad 2.9$$

with $m = 3$ and $n = 2,2', 1,1'$ as in figure 2.1. E_{mn} is the intersubband energy spacing between individual levels. The same parameters as in eq. 2.8 are used in the calculations of eq. 2.9. We calculate a global IFR relaxation time for the upper laser level, state 3, of ~ 0.724 ps.

Involved levels	**Scattering rate (ps^{-1})**	**Scattering time (ps)**
3 – 2	0.672	1.486
3 – 2′	0.316	3.156
3 – 1	0.28	3.518
3 – 1′	0.106	9.405

Table 2.6 Calculated IFR intersubband scattering rate and times for selected states of the 3.39 μm emitting QCL on MBL design. Involved levels are labeled as in figure 2.1.

For $\eta_{inj,tot}$ we obtain a value of 0.94 by using calculated values of 0.97 for both η_{inj} and η_p [12]. The relatively high value for η_p is a reflection of both high E_{43} (84.4 meV) and τ_{43} (0.51 ps) values which lead to negligible leakage current [see eq. 2.4]. By using total values (i.e., including IFR scattering) for τ_{3g}, $\tau_{22'g}$, and τ_{32g} we obtain a total value for $\tau_{up,g}$ 0.428 ps. Then, the gain coefficient g is calculated to be 3.14 cm/kA, and is kept constant along with the waveguide loss for all simulations following.

Asymmetry of transverse-field profiles is due to the unequal thicknesses of the optical-confinement layers employed in these designs (figure 2.5). These thicknesses are chosen in accordance with the optimization of the Γg product and the sum of losses (α_{tot}= $\alpha_m + \alpha_{w,sim} +$

$\alpha_{isb,bf}$) in order to obtain the lowest J_{th} value. For a fixed lower-cladding thickness of 2 μm and upper cladding thickness of 3.5 μm, the best-case scenarios with the highest Γ, lowest α_{tot} and lowest J_{th} values are shown in figure 2.5.

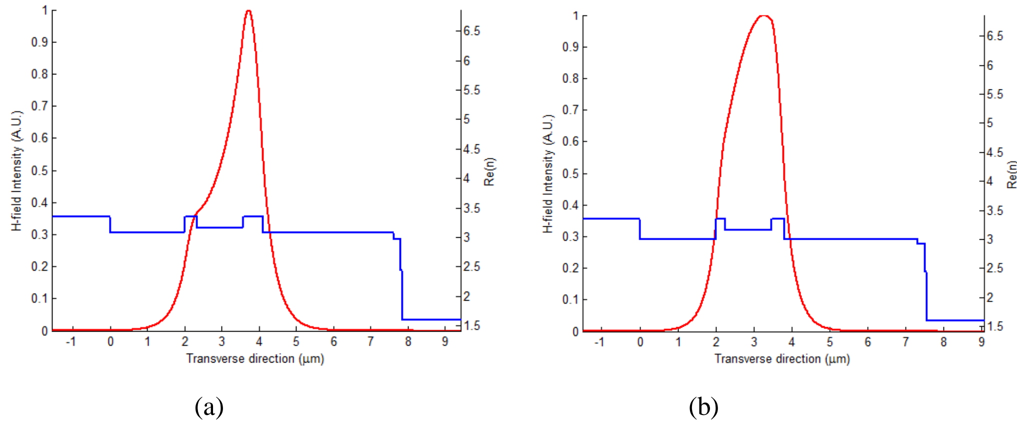

Figure 2.5. Simulation of magnetic-field intensity profile of the fundamental transverse mode for the complete laser structure with 2 μm thick: (a) $In_{0.69}Ga_{0.31}P$; (b) $In_{0.21}Al_{0.79}As$ lower-cladding layers.

On observing that InAlAs is the material of choice over InGaP in order to obtain the lowest J_{th} value for these QCLs (table 2.5), the impact of varying the thickness of the lower-cladding layer is studied for 3 mm long, HR-coated devices. It is evident that the 3 μm thick InAlAs lower-cladding configuration is theoretically the best in terms of the confinement factor and loss coefficient α_{sim} and that the J_{th} value is expected to be only ~ 10 % higher than that for the 4.6 μm emitting QCL. There is scope for improvement by increasing the cavity length to 5 mm in order to reduce α_m and consequently, J_{th}. That is, for L = 5 mm, the J_{th} value decreases to 0.99 kA/cm^2, for the 3 μm thick InAlAs lower-cladding design. Additionally, this configuration results in a symmetric mode profile owing to equal lower and upper confinement layer thicknesses, again obtained by minimizing (α_{tot}/ Γ).

We also performed a thermal analysis that provides an understanding of the heat dissipation in 3.4 μm emitting QCLs on MBL with InAlAs and InGaP cladding layers when compared to an

InP cladding 4.6 μm QCLs [47]. InP is the obvious cladding layer choice for InP-based QCLs being a well-characterized binary material with high thermal conductivity (68.03 W/m.K) [22], [23].

The thermal dissipation simulation is performed on a model using the best configuration obtained from optical-mode analysis for the 3.4 μm emitting QCL using InAlAs cladding layers (figure 2.6 (c)). This is compared to QCL structures of InGaP and InP cladding layers as to analyze the effectiveness of these materials as thermally conducting cladding layers (figure 2.6 (a), (b)). 10 μm wide and 5 mm long ridge structures are considered, with a Si_3N_4 current-confinement dielectric layer, and plated Au around and above the ridge.

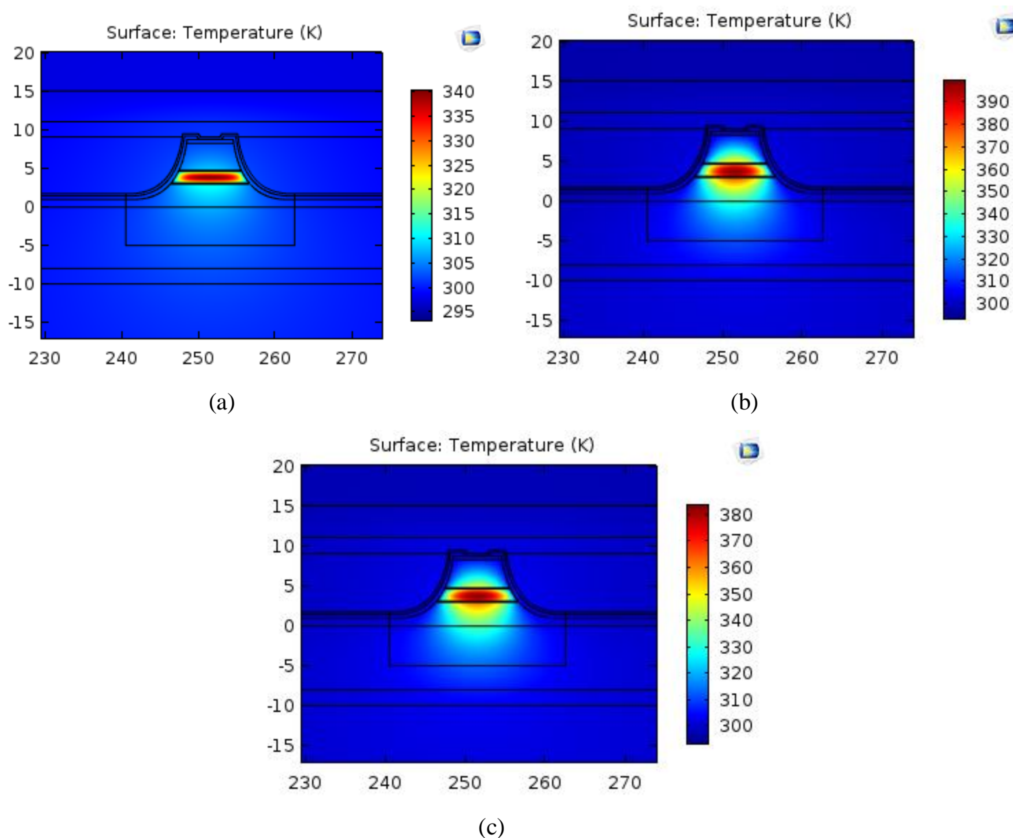

Figure 2.6 Simulated thermal dissipation within the complete laser structure, for a 5 mm long device. with: (a) InP; (b) $In_{0.69}Ga_{0.31}P$; (c) $In_{0.21}Al_{0.79}As$ cladding layers, for 15 W power to dissipate.

To quantify this heat dissipation, we look at the average temperature rise, ΔT_{act}, in the core region with respect to the heatsink temperature, which is taken to be room temperature. We assume 5% CW wallplug efficiency for the input power (i.e., 95% of the input power will be dissipated as heat). The 5 % value is chosen to be about twice that obtained for 3.56 μm emitting QCLs [3] at room temperature (i.e., ~ 2.5 %), since our structure has carrier leakage suppression which has been shown [31] to result in basically doubling of the CW wallplug efficiency value compared to devices with significant carrier leakage. The ΔT_{act} value for structures with InP, InGaP and InAlAs claddings, given 15 W of input power, is 33.6 K, 74.6 K, and 63.8 K respectively. That is, using InAlAs claddings increases ΔT_{act} by a factor of ~ 1.9 compared to when using InP claddings, and decreases ΔT_{act} by ~ 15 % to when using InGaP claddings. The former illustrates the penalty expected in thermal conduction for short-wavelength QCLs employing ternary cladding layers lattice-matched to the virtual-substrate layers atop on MBLs.

2.4.3 QCL active region regrowth: test structures

As a measure of the suitability of the HVPE-MBL substrates for QCL use, the growth of ten stages of this QCL design was carried out on the CMP and wet-etched MBL surface. Optical images obtained using the Nomarski microscope, demonstrate that the surface morphology is significantly smoother than the as-grown MBL for the test structure regrowth (figure 2.7).

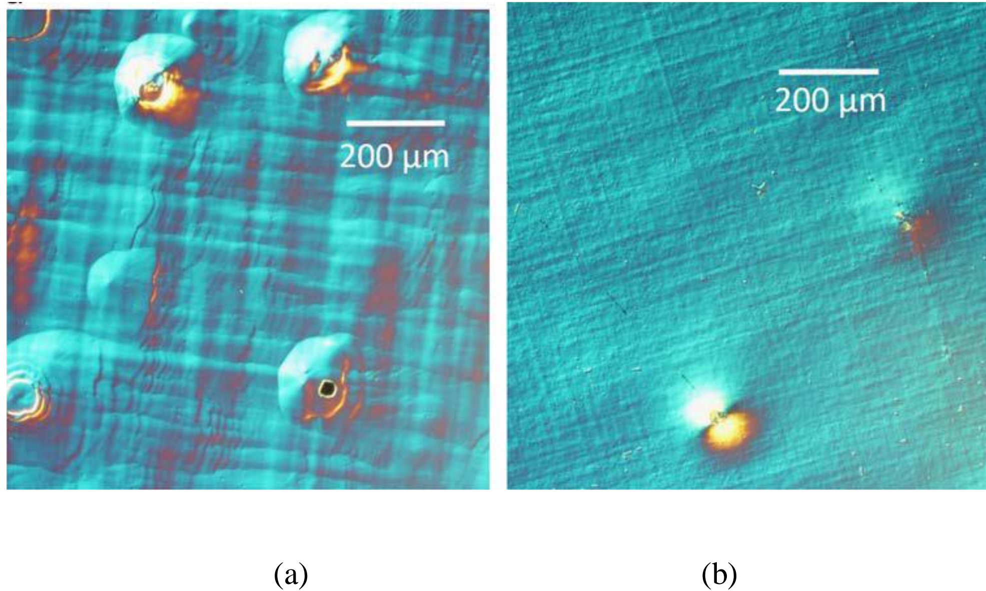

(a) (b)

Figure 2.7 Optical Images, using Nomarski interference contrast, depicting surface morphology of (a) As-grown MBL, (b) 10-stage QCL active region regrowth on a surface- optimized MBL.

It is observed that the applied polishing procedure is effective in preparing a virtual substrate appropriate for regrowth of structures with strained layers, as is also evident from the TEM and XRD data. To assess the structural characteristics of the superlattice region grown on the MBL, grown layers were imaged using diffraction contrast TEM of ⟨110⟩ cross-sectional specimens. The image shown in figure 2.8 (a) portrays the ten-stage stack of the QCL active region grown on the MBL. Dislocations originating in the MBL cap layer are seen propagating through the regrown layers. The dislocation density for this sample is estimated to be $1x10^5$ cm^{-2} from the etch pits observed in dark field images obtained with an optical microscope. Figure 2.8 (b) is a higher magnification image of a few stages showing distinct contrast to the well and barrier layers suggesting sharp and uniform interfaces, although it is difficult to quantify the interface roughness from such a TEM image.

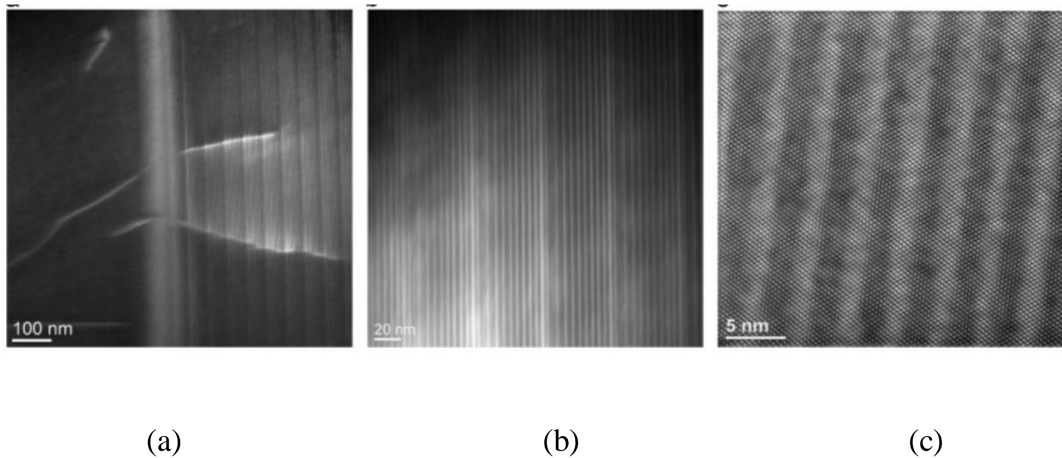

(a) (b) (c)

Figure 2.8 TEM images: (a){220} dark- field image of ten stages of QCL active region regrowth on an MBL, showing dislocations propagating from the cap layer through the regrown SL layers, (b)Higher magnification image of (a),(c)Phase contrast high-resolution image providing atomic detail within a stage.

Figure 2.8 (c) is a phase contrast TEM image providing atomic-scale detail. This image was used to calculate the individual layer thicknesses which are subsequently used to fit the XRD data (table 2.7).

Target thickness	**25**	16	**24**	17	**21**	18	**20**	**21**	**19**	21	**18**	18	**17**	28	**12**	13	**39**	10	**33**	16
Actual thickness	**26**	18	**23**	20	**20**	18	**20**	20	**18**	18	**18**	18	**18**	23	**12**	15	**41**	18	**35**	18

Table 2.7 Comparison of the target thicknesses for one stage of the active region design with the actual thickness values calculated from Figure 2.8 (c). All thickness values are in Angstroms. Bold numbers indicate wells and others indicate barriers in the QCL test structure.

The high-resolution X-ray diffraction pattern consisting of a reciprocal space map (RSM) of the (004) reflection is shown in figure 2.9 (a). The well-defined superlattice fringes possess a narrow FWHM within the RSM indicating that the layers are uniform with relatively sharp interfaces. Figure 2.9 (b) shows the integrated mosaic intensity along the ω axis at each point on the 2θ axis. This simulates a conventional rocking curve taken in a ω–2θ geometry. The integrated line is shown as the upper solid line while the lower dashed line is a simulation portraying the best fit. The best fit simulation is obtained by using 1.15 × TEM thickness for the wells and 0.8 × TEM

thickness for the barriers. Up to a 20% error in the calculated thicknesses is well within the acceptable range of uncertainty for deriving such layers from the TEM micrograph. This uncertainty amounts to ±one monolayer which is easily accounted for in the abruptness of the interfaces.

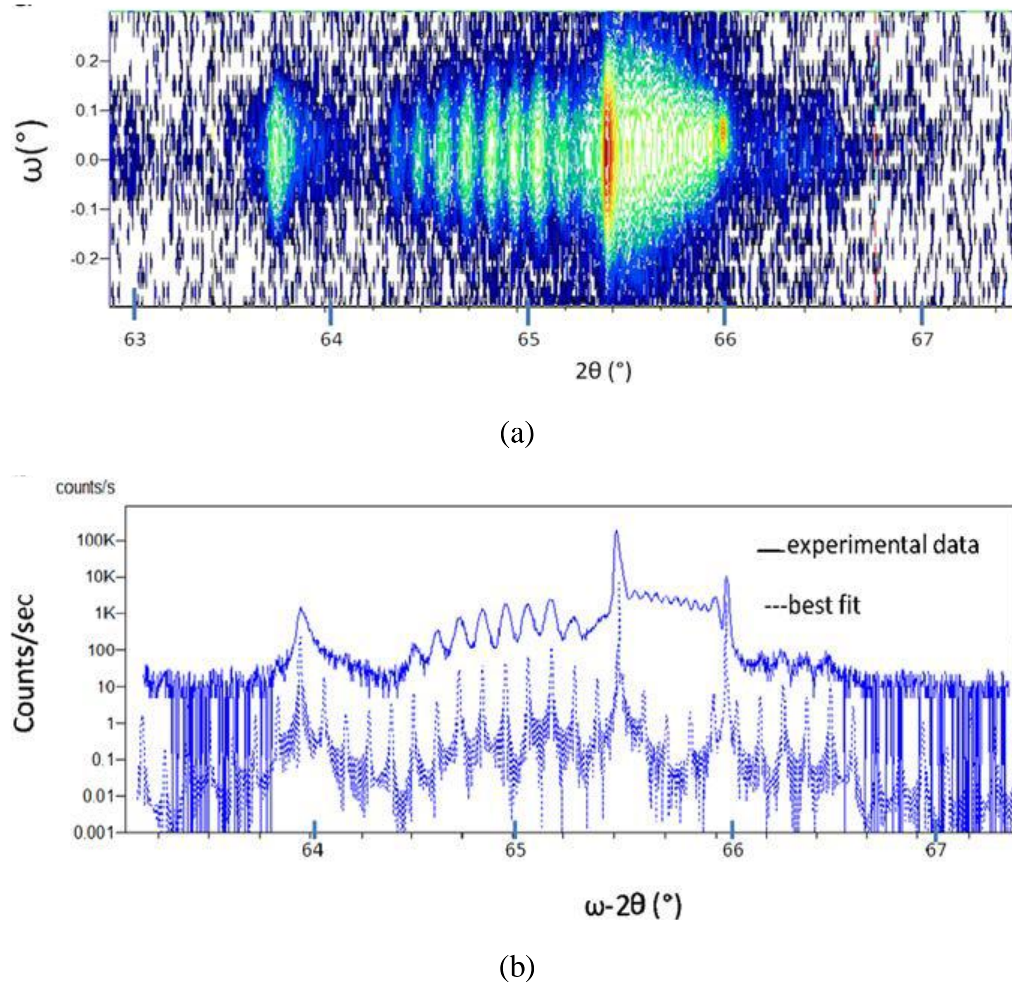

Figure 2.9 HR-XRD scans (a) (004) ω–2θ RSM, (b) (004) ω–2θ line scan (solid) compared with best fit simulation (dashed).

Similarly, the growth of ten stages of the active region along with a 2 μm lower cladding, 3.5 μm upper cladding and confinement layers was performed. Associated TEM data is shown in figure 2.10 demonstrating highly planar and well-formed SL. Further confirmation is obtained from the SL fringes as seen from the (004) XRD scan in figure 2.11. The 10-stage QCL sample

has been processed into 200 µm wide mesa devices to observe electroluminescence. These devices appear to be highly resistive as observed from the current vs. voltage characteristics (I-Vs) in figure 2.12. It was also observed that the mesa devices do not degrade upon repeated measurements.

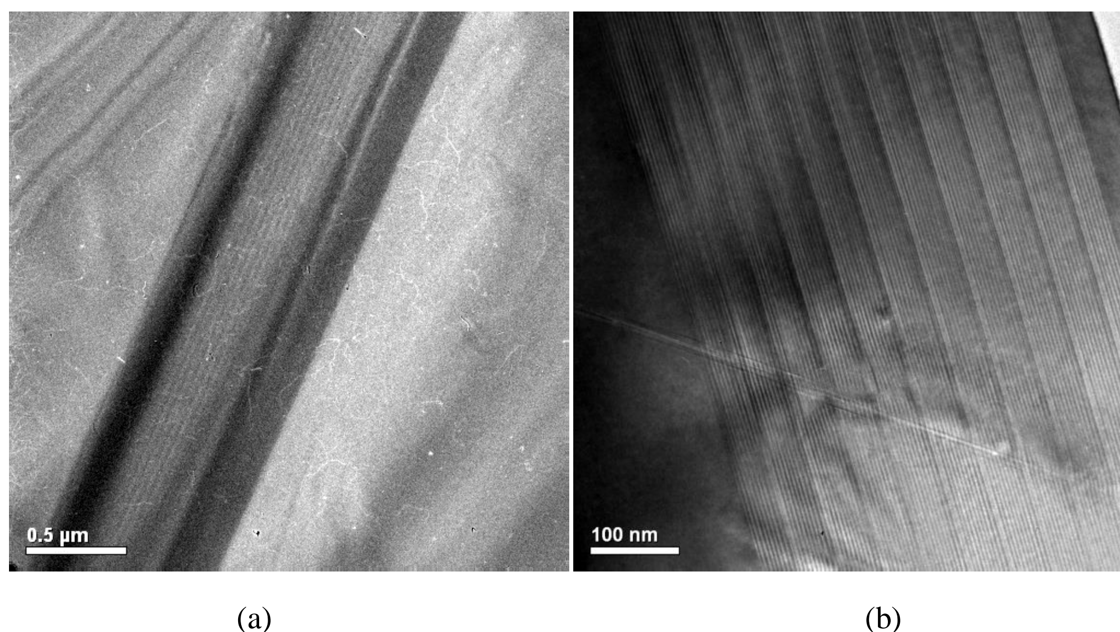

Figure 2.10 TEM images for the growth of the 10-stages of the QCL active region with cladding and confinement layers (a) lower magnification image showing the entire structure (b) higher magnification image showing the 10-stage repetition and a defect propagating through the constituent SL

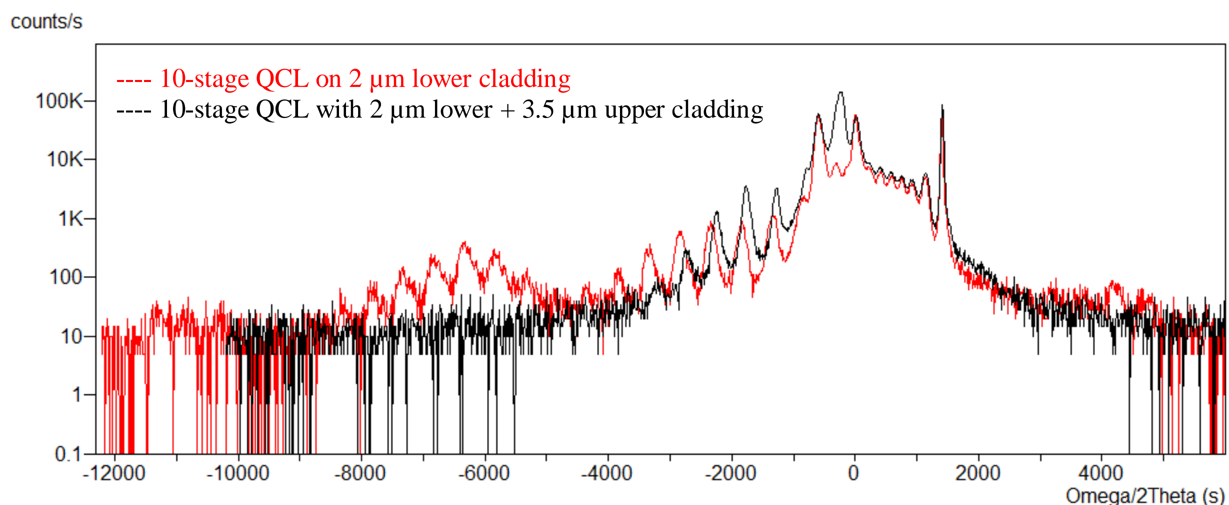

Figure 2.11 HRXRD along the (004) comparing the 10-stage regrowth with and without the upper cladding.

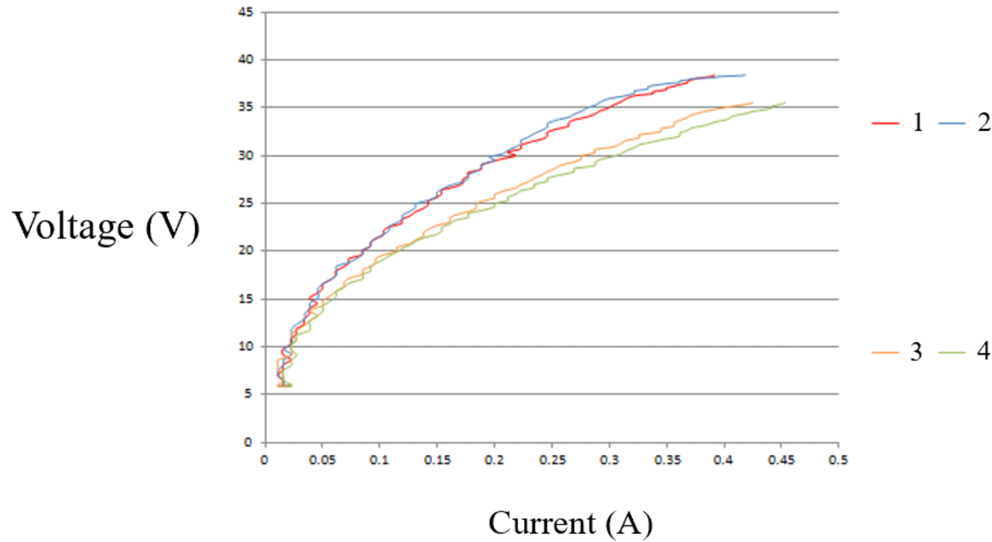

Figure 2.12: I-V characteristics for 4 mesa devices obtained from 10-stage QCL sample

2.4.4 QCL active region regrowth: complete structure

The 30-stage QCL full structure was grown with cladding, confinement and contact layers as discussed for 10-stage QCL, using the HVPE-grown MBL material. The lower confinement layer was 250 nm thick $In_{0.22}Ga_{0.78}As$ with a target doping level of $1x10^{17}$ cm^{-3} n-type. The growth temperature is reverted back to 600 °C for the upper cladding layer to protect the active region underneath. Both cladding layers have a target n-type doping level of $1x10^{17}$ cm^{-3}. The contact layer is a highly doped $In_{0.22}Ga_{0.78}As$ targeting $5x10^{18}$ cm^{-3}. As expected, the intensity of the observed SL fringes increases with the higher number of stages and more SL fringes were observed in comparison with the 10-stages regrowth. (figure 2.13). Nomarski microscopic image of this surface is shown in (figure 2.14).

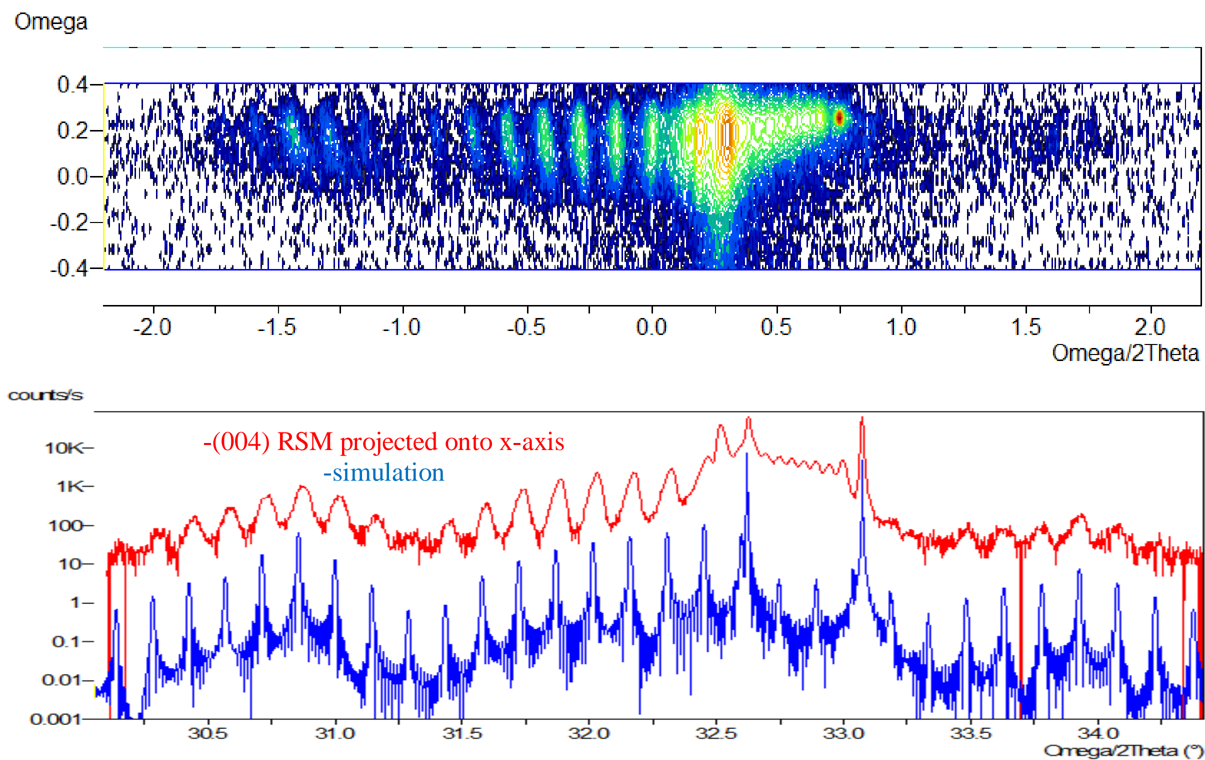

Figure 2.13 (004) RSM for the 30-stages of the active region regrowth on the lower cladding, with the corresponding omega-2theta extracted scan

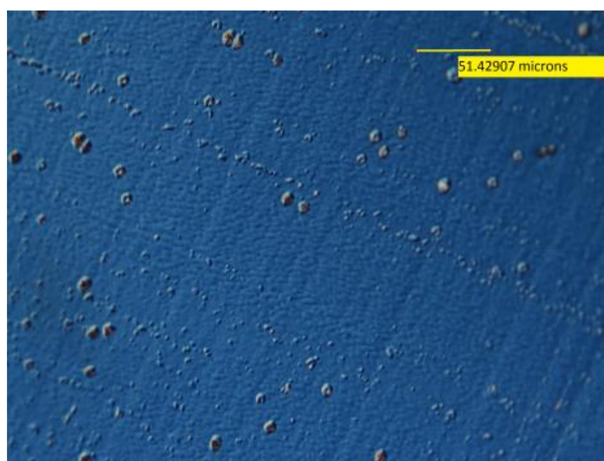

Figure 2.14 Nomarski image of the surface after 30-stage QCL regrowth on lower cladding and confinement layers atop the MBL

This QCL on MBL material was processed into ridge waveguide devices (figure 2.15) which turned out to be highly resistive. Cross-section STEM images were obtained on a chip in order to better understand defects as possible causes for the observed device performance. The images are taken from the central part of the ridge guide. In the low magnification image, a set of defects are seen disrupting the SL layers. This could possibly be originating on the top of the MBL due to hillock formations during HVPE growth. The rest of the SL, however, shows the layers to be well aligned even in the high magnification images although with some waviness. Work is ongoing to compare layer thicknesses as seen in STEM images with the target and see if there are any deviations across the ridge due to the MBL surface morphology.

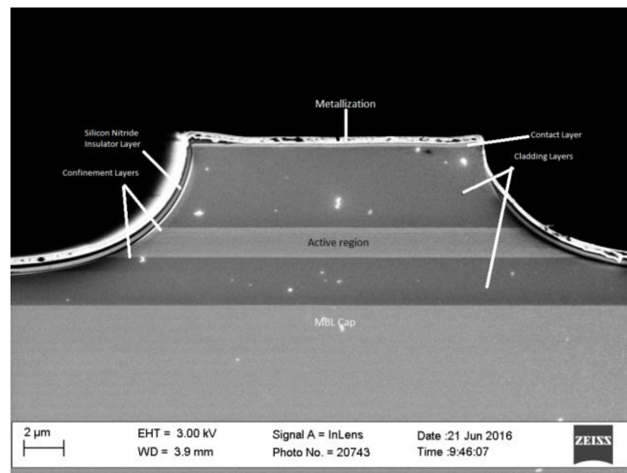

Figure 2.15: Cross-sectional SEM image showing the fabricated ridge waveguide device from the complete laser structure regrowth using the 30-stage QCL on the MBL

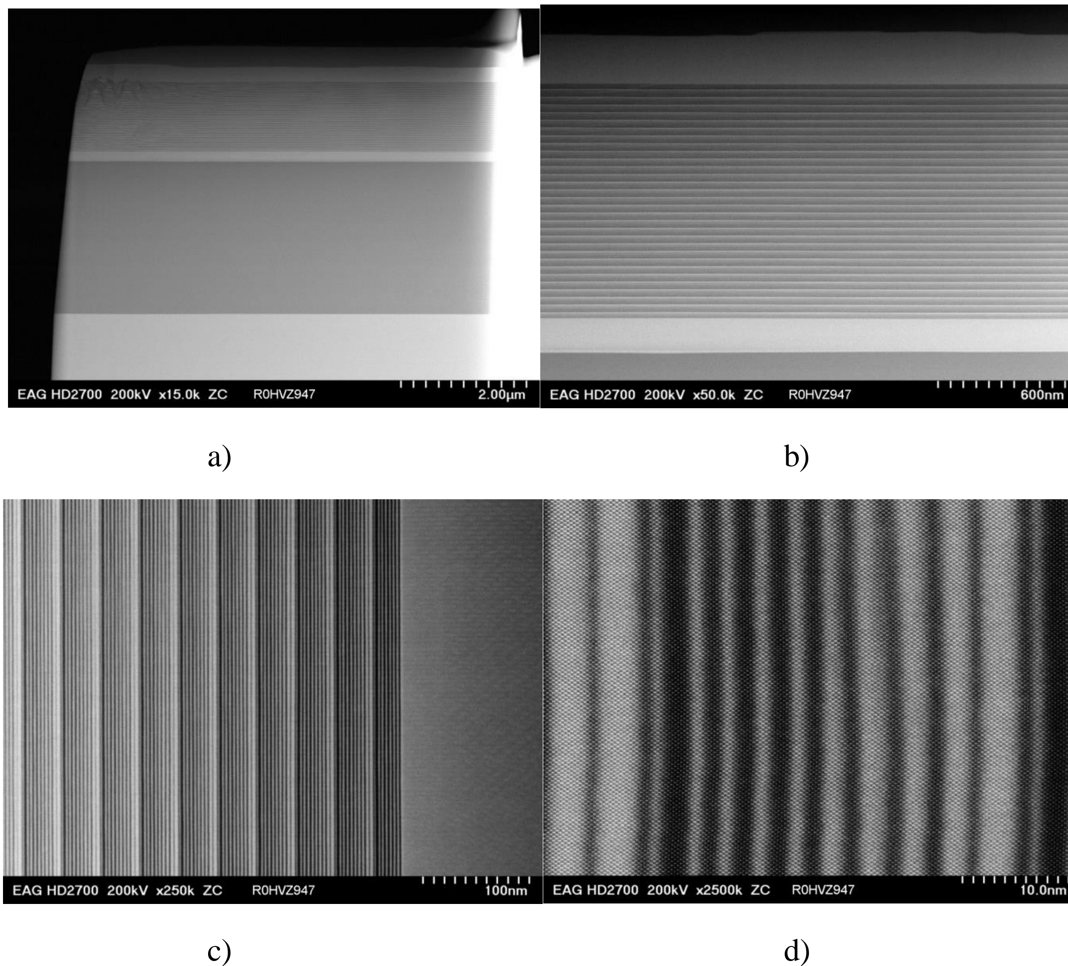

Figure 2.16: Cross-sectional STEM images of the full QCL structure regrowth on an MBL, shown at various magnifications

The resistive I-Vs (figure 2.17) for these devices are seen to degrade with repeated measurements. The cause of this degradation is suspected to be the cladding layer doping. This is difficult to calibrate as the $In_{0.21}Al_{0.79}As$ is not lattice-matched to the commercially available semi-insulating (S.I.) substrates GaAs and InP for a traditional Hall measurement. For this set of experiments, the doping level for $In_{0.21}Al_{0.79}As$ was estimated by growing n-type doped AlAs on S.I. GaAs. At a growth temperature of 700 °C and a growth rate of 1.04 μm/hr for AlAs, with a 1 sccm flow of disilane, an n-type doping level of 8.5×10^{17} cm^{-3} was obtained by Hall measurement. In the future, we intend to perform Electrochemical Capacitance Voltage (ECV) measurements to confirm the doping trends in $In_{0.21}Al_{0.79}As$ grown on the MBL.

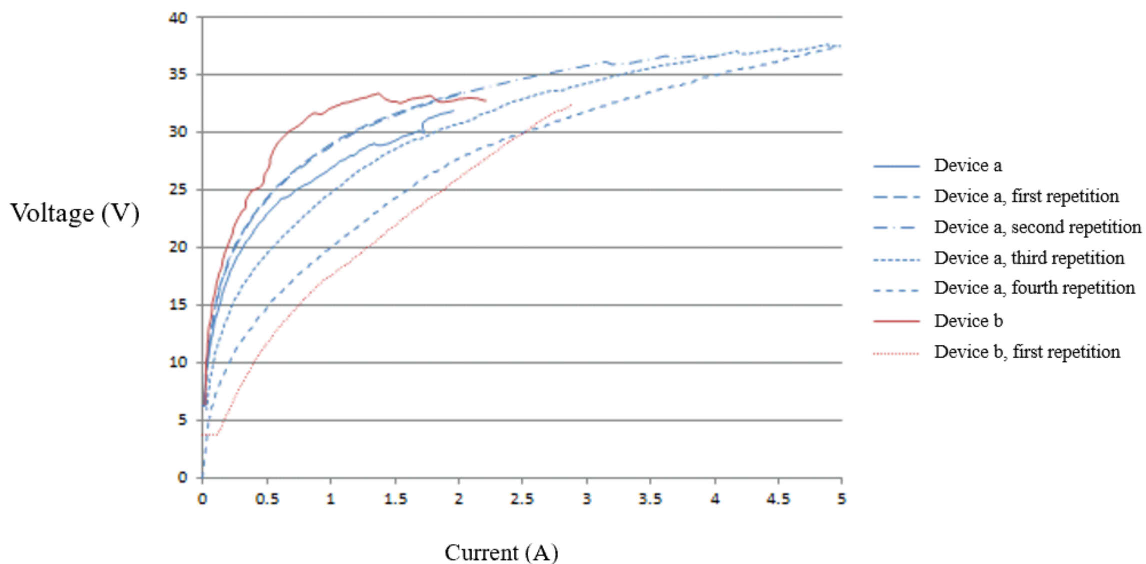

Figure 2.17: I-V characteristics for 2 ridge guide devices obtained from the 30-stage QCL sample, with the measurement iteration as indicated

2.4.5 MOCVD-MBL

HVPE enables high growth rate (~100 µm/hr) for MBL growth unlike with MOCVD. Also, the reactor geometry of the HVPE reactor at UW-Madison allows for a fixed sample holder size which can accommodate a substrate size of ~4 cm^2 per growth run [48]. It is desirable to have MOCVD-grown MBLs to have highly repeatable MBL cap layer compositions, as well as the ability to grow on multiple, full 2” GaAs substrates, even if the growth process has a penalty in the achievable growth rates. It is also beneficial if the hillocks often observed in high growth rate HVPE-MBLs [9] can be avoided. To demonstrate the potential for MOCVD to grow ternary materials at relatively high growth rates, MBLs with different compositional gradings than HVPE-MBLs, were grown by MOCVD, with growth rates up to 3 µm/hr. Higher growth rates are achievable, although this would require altering the TMIn and TMGa bath temperatures.

MBL 1 was grown with 22 composition steps with a target 1% In increment in each 0.14 µm thick step [29]. A 2 µm thick cap was grown at the target In composition accounting for the in-plane lattice constant of the nearly fully relaxed last composition step. XRD data for the same is shown in figure 2.18 (a) along with the reciprocal space map in (004) figure 2.18 (b). The cap layer is found to be of the composition $In_{0.18}Ga_{0.82}As$, with 94% relaxation. A Nomarski optical image shows the expected cross-hatch pattern due to strain relaxation (figure 2.18 (c)).

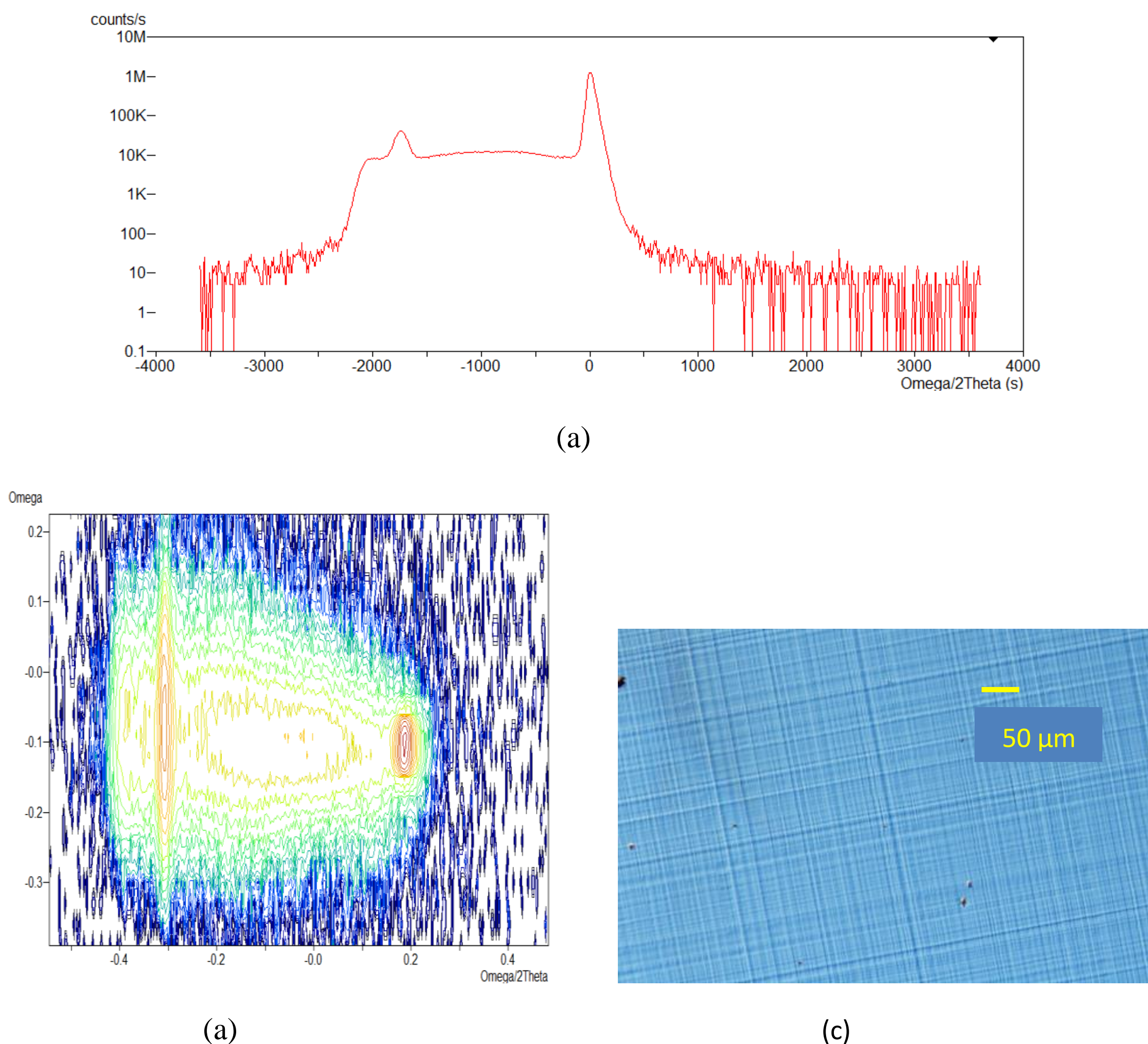

Figure 2.18 MOCVD MBL1 (a) 004 XRD scan (b) 004 RSM (c) Nomarski optical image showing the cross-hatched surface

MBL2 growth experiment focused on increasing the growth rates by 2.5 times and also incorporating n-type doping as intended for establishing contacts to the QCL device. The average doping when MBL2 is grown on a semi-insulating GaAs substrate is 8.7×10^{17} cm^{-3} n-type by Hall measurement. The surface morphology is as depicted in figure 2.19 (a). The cap layer has a composition $In_{0.18}Ga_{0.82}As$ with 86% relaxation as calculated from the XRD data (figure 2.19 (b)).

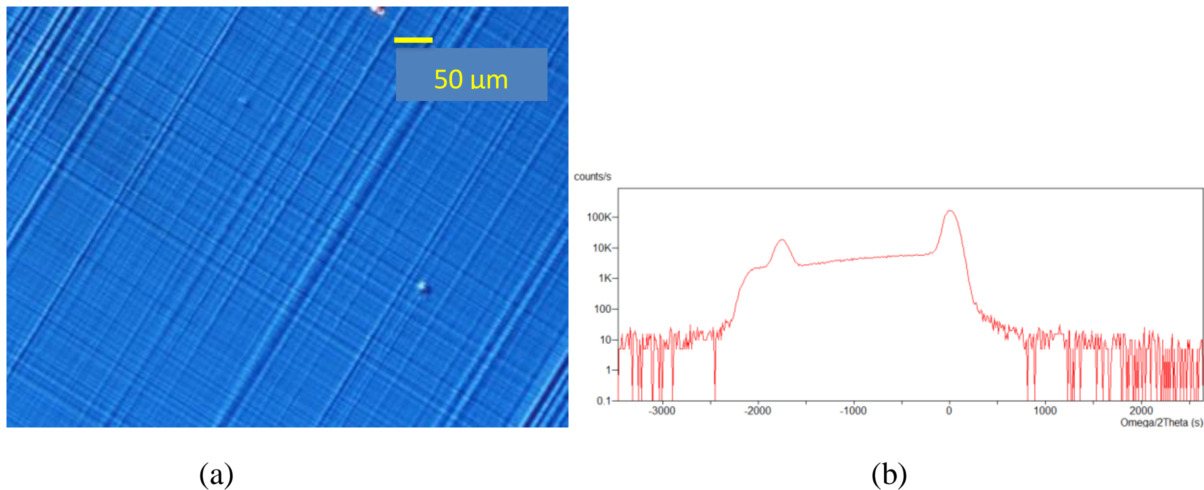

(a) (b)

Figure 2.19 (a) Surface morphology of MOCVD MBL2 by a Normarski optical image (b) (004) XRD scan

An optimized surface preparation technique was developed for HVPE-MBLs [9]. To apply CMP and consequent wet etching to reduce the cross-hatched surface morphology, the MBL needs to have thicker caps (tens of microns). To achieve this, MBL2 growth recipe was repeated with longer growth times for the cap layer. An optical image for such an MBL before and after CMP is shown in figure 2.20.

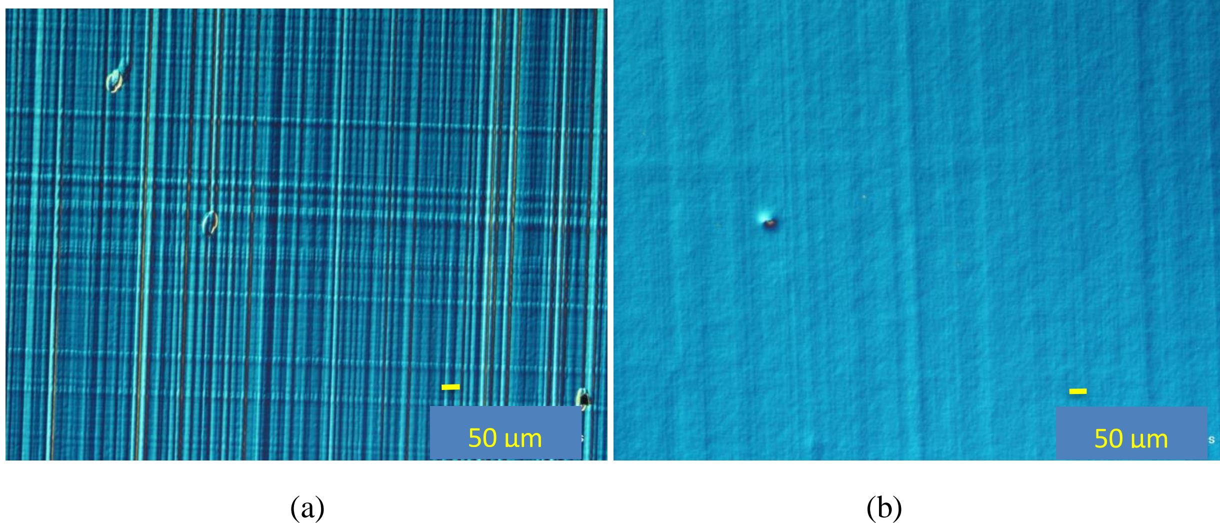

(a) (b)

Figure 2.20 Nomarski optical images of MOCVD MBL2 (a) as-grown with a thick cap layer (b) after CMP procedure

Few surface features are observed on the MBL surface, other than the expected cross-hatched morphology. The initial InAlAs QCL cladding layer calibrations lattice-matched to the InGaAs cap layer of the MBL have been completed and full QCL structure growth is planned for future work.

2.5 Conclusions

A mid-IR QCL with an emission wavelength of 3.4 μm is designed for a virtual substrate of the composition $In_{0.22}Ga_{0.78}As$. This design has the advantage of depopulation of the lower laser level involving both the SPR scheme and resonant-tunneling extraction to the extractor/injector region. In turn, one obtains fast, miniband-like carrier extraction from the AR. In collaboration with MIT, scattering due to IFR is taken into account to estimate an EL linewidth of 54.6 meV for this device. Utilizing both elastic and inelastic lifetimes, the J_{th} value is projected to be as low as 1.4 kA/cm^2 for 3 mm long, HR-coated devices. The thermal and optical characteristics of InAlAs cladding and InGaP cladding structures for the presented QCL design on MBLs are analyzed. InAlAs is computationally shown to be more effective than InGaP in confining the optical field as well as

better for dissipating the generated heat. There is, however, a penalty in the heat dissipation of such a QCL owing to the requirement of a ternary cladding layer lattice-matched to the MBL when compared to the InP-based QCLs employing InP claddings.

An HVPE-grown MBL was used to access a substrate lattice parameter which could not be obtained by the use of a conventional binary semiconductor substrate. CMP and wet-chemical etching were found to be effective in preparing the MBL surface for growth of the QCL structure. Successful MOVPE growth of ten and thirty stages of a QCL active region with cladding and confinement layers on such a surface has been achieved with high structural fidelity.

Future work includes growth and characterization of QCLs with the designed cladding layers on MOCVD grown MBLs.

References

[1] P. Franzosi, G. Silviati, F. Genova, A. Stano, and F. Taiariol, "Misfit dislocations in InGaAs/InP MBE single heterostructures," *J. Cryst. Growth*, vol. 75, no. 3, pp. 521–534, 1986.

[2] R. Beanland, D. J. Dunstan, and P. J. Goodhew, "Plastic relaxation and relaxed buffer layers for semiconductor epitaxy," *Adv. Phys.*, vol. 45, no. 2, pp. 87–146, 1996.

[3] N. Bandyopadhyay, S. Slivken, Y. Bai, and M. Razeghi, "High power, continuous wave, room temperature operation of $\lambda \sim 3.4$ µm and $\lambda \sim 3.55$ µm InP-based quantum cascade lasers," *Appl. Phys. Lett.*, vol. 100, no. 212104, pp. 1–4, 2012.

[4] A. Aldukhayel *et al.*, "Investigations of carrier scattering into L-valley in λ=3.5µm InGaAs/AlAs(Sb) quantum cascade lasers using high hydrostatic pressure," *Phys. Status Solidi*, vol. 250, no. 4, pp. 693–697, 2013.

[5] A. Bismuto, M. Beck, and J. Faist, "High power Sb-free quantum cascade laser emitting at 3.3 µm above 350 K," *Appl. Phys. Lett.*, vol. 98, no. 191104, 2011.

[6] N. Bandyopadhyay, Y. Bai, S. Tsao, S. Nida, S. Slivken, and M. Razeghi, "Room temperature continuous wave operation of $\lambda \sim 3 - 3.2$ µm quantum cascade lasers," *Appl. Phys. Lett.*, vol. 101, no. 241110, pp. 1–4, 2012.

[7] M. P. Semtsiva, M. Wienold, S. Dressler, and W. T. Masselink, "Short-wavelength ($\lambda \approx$ 3.05 µm) InP based straincompensated quantum-cascade laser," *Appl. Phys. Lett.*, vol. 90, no. 051111, 2007.

[8] L. J. Mawst *et al.*, "InGaAs/AlInAs strain-compensated Superlattices grown on metamorphic buffer layers for low-strain, 3.6 µm-emitting quantum-cascade-laser active regions," *J. Cryst. Growth*, vol. 370, pp. 230–235, 2013.

[9] A. Rajeev *et al.*, "Regrowth of quantum cascade laser active regions on metamorphic buffer layers," *J. Cryst. Growth*, vol. 452, pp. 268–271, 2016.

[10] L. J. Mawst *et al.*, "Low-strain, quantum-cascade-laser active regions grown on metamorphic buffer layers for emission in the 3.0–4.0 µm wavelength region," *IET Optoelectron.*, vol. 2013.0060, no. 10.1049, pp. 1–8, 2013.

[11] B. T. Zutter *et al.*, "Planarization and processing of metamorphic buffer layers grown by hydride vapor-phase epitaxy," *J. Electron. Mater.*, vol. 43, no. 4, pp. 873–878, 2014.

[12] D. Botez, C. C. Chang, and L. J. Mawst, "Temperature sensitivity of the electro-optical characteristics for mid-infrared (λ = 3-16 µm)-emitting quantum cascade lasers," *J. Phys. D. Appl. Phys.*, vol. 49, no. 043001, pp. 1–33, 2016.

[13] N. Bandyopadhyay *et al.*, "Watt level performance of quantum cascade lasers in room temperature continuous wave operation at λ~3.76 µm," *Appl. Phys. Lett.*, vol. 97, no. 131117, pp. 1–3, 2010.

[14] J. D. Kirch *et al.*, "86% internal differential efficiency from 8 to 9 microns-emitting, step-taper active-region quantum cascade lasers," *Opt. Express*, vol. 24, no. 21, pp. 24483–24494, 2016.

[15] S. Li, G. Witjaksono, S. Macomber, and D. Botez, "Analysis of Surface-Emitting Second-Order Distributed Feedback Lasers With Central Grating Phaseshift," *IEEE J. Sel. Top. Quantum Electron.*, vol. 9, no. 5, pp. 1153–1165, 2003.

[16] P. Drude, "Zur Elektronentheorie der Metalle," *Ann. Phys.*, vol. 306, no. 3, pp. 566–613, 1900.

[17] P. Drude, "Zur Elektronentheorie der Metalle; II. Teil. Galvanomagnetische und thermomagnetische Effecte," *Ann. Phys.*, vol. 308, no. 11, pp. 369–402, 1900.

[18] M. A. Ordal, R. J. Bell, R. W. Alexander, L. L. Long, and M. R. Querry, "Optical properties of Au, Ni, and Pb at submillimeter wavelengths," *Appl. Opt.*, vol. 26, no. 4, pp. 1203–1209, 1988.

[19] M. A. Ordal, R. J. Bell, R. W. Alexander, L. A. Newquist, and M. R. Querry, "Optical properties of Al, Fe, Ti, Ta, W, and Mo at submillimeter wavelengths," *Appl. Opt.*, vol. 27, no. 6, pp. 1203–1209, 1988.

[20] R. P. Leavitt *et al.*, "High-performance quantum cascade lasers in the 7.3- to 7.8-µm wavelength band using strained active regions," *Opt. Eng.*, vol. 49(11), no. 111109, 2010.

[21] S. Adachi, "Lattice thermal resistivity of III-V compound alloys," *J. Appl. Phys.*, vol. 54, no. 4, pp. 1844–1848, 1983.

[22] W. Nakwaski, “Thermal conductivity of binary, ternary, and quaternary III-V compounds,” *J. Appl. Phys.*, vol. 64, no. 1, pp. 159–166, 1988.

[23] H. Yang, H. Wang, and K. Radhakrishnan, “Thermal resistance of metamorphic InP-based HBTs on GaAs substrates using a linearly graded In/sub x/Ga/sub 1-x/P metamorphic buffer,” *IEEE Trans. Electron Devices*, vol. 51, no. 8, pp. 1221–1227, 2004.

[24] H. K. Lee and J. S. Yu, “Thermal effects in quantum cascade lasers at λ ~ 4.6 µm under pulsed and continuous-wave modes,” *Appl. Phys. B*, vol. 106, no. 3, pp. 619–627, 2012.

[25] M. Razeghi, “High-performance InP-based mid-IR quantum cascade lasers,” *IEEE J. Sel. Top. Quantum Electron.*, vol. 15, no. 3, pp. 941–951, 2009.

[26] R. Jin, “Sub-nanossecond pulse characteristics of InGaP/GaAs HBTs,” Lehigh Preserve.

[27] W. Both and F. P. Hermann, “Thermal resistivity of quaternary solid solution GaxIn1-xAsyP1-y lattice matched to InP and GaAs,” *Cryst. Res. Technol.*, vol. 17, no. K117, 1982.

[28] K. L. Schulte *et al.*, “Metalorganic vapor phase growth of quantum well structures on thick metamorphic buffer layers grown by hydride vapor phase epitaxy,” *J. Cryst. Growth*, vol. 370, pp. 293–298, 2013.

[29] K. E. Lee and E. A. Fitzgerald, “High-quality metamorphic compositionally graded InGaAs buffers,” *J. Cryst. Growth*, vol. 312, pp. 250–257, 2010.

[30] L. J. Mawst *et al.*, “Quantum-cascade-laser active regions on metamorphic buffer layers,” in *Proceedings of SPIE - The International Society for Optical Engineering*, 2015, vol. 9370.

[31] D. Botez, J. C. Shin, J. D. Kirch, C. C. Chang, L. J. Mawst, and T. Earles, “Multidimensional conduction-band engineering for maximizing the continuous-wave (CW) wallplug efficiencies of mid-infrared quantum cascade lasers,” *IEEE J. Sel. Top. Quantum Electron.*, vol. 19, no. 4, 2013.

[32] J. Faist, F. Capasso, D. L. Sivco, C. Sirtori, A. L. Hutchinson, and A. Y. Cho, “Quantum Cascade Laser,” *Science*, vol. 264, pp. 553–556, 1994.

[33] D. Botez, S. Kumar, J. C. Shin, L. J. Mawst, I. Vurgaftman, and J. R. Meyer, “Temperature dependence of the key electro-optical characteristics for midinfrared emitting quantum cascade lasers,” *Appl. Phys. Lett.*, vol. 97, no. 7, pp. 1–4, 2010.

[34] D. Botez, “Comment on ‘Highly temperature insensitive quantum cas- cade lasers,” *Appl. Phys. Lett.*, vol. 98, no. 216101, 2011.

[35] D. Botez *et al.*, “The temperature dependence of key electro-optical characteristics for mid-infrared emitting quantum cascade lasers,” in *SPIE OPTO Proceedings Volume 7953, Novel In-Plane Semiconductor Lasers X*, 2011.

[36] D. Botez, J. C. Shin, S. Kumar, L. J. Mawst, I. Vurgaftman, and J. R. Meyer, “Electron leakage and its suppression via deep-well structures in 4.5- to 5.0-µm-emitting quantum

cascade lasers," *Opt. Eng.*, vol. 49(11), no. 111108, 2010.

[37] J. C. Shin *et al.*, "Highly temperature insensitive, deep-well 4.8 μm emitting quantum cascade semiconductor lasers," *Appl. Phys. Lett.*, vol. 94, no. 20, pp. 1–4, 2009.

[38] J. P. Commin, D. G. Revin, S. Y. Zhang, A. B. Krysa, K. Kennedy, and J. W. Cockburn, "High peak power λ~3.3 and 3.5 μm InGaAs/AlAs(Sb) quantum cascade lasers operating up to 400 K," *Appl. Phys. Lett.*, vol. 97, no. 3, pp. 31106–31109, 2010.

[39] Y. V. Flores *et al.*, "Thermally activated leakage current in high-performance short-wavelength quantum cascade lasers," *J. Appl. Phys.*, vol. 113, no. 13, 2013.

[40] R. Maulini *et al.*, "High power thermoelectrically cooled and uncooled quantum cascade lasers with optimized reflectivity facet coatings," *Appl. Phys. Lett.*, vol. 95, no. 15, pp. 1–4, 2009.

[41] A. Lyakh *et al.*, "1.6 W high wall plug efficiency, continuous-wave room temperature quantum cascade laser emitting at 4.6 μm," *Appl. Phys. Lett.*, vol. 92, no. 11, pp. 18–20, 2008.

[42] C. Pflügl *et al.*, "Activation energy study of electron transport in high performance short wavelengths quantum cascade lasers," vol. 18, no. 2, pp. 746–753, 2010.

[43] J. B. Khurgin, "Inhomogeneous origin of the interface roughness broad- ening of intersubband transitions," *Appl. Phys. Lett.*, vol. 93, no. 091104, 2008.

[44] A. Wittmann, Y. Bonetti, J. Faist, E. Gini, and M. Giovannini, "Intersubband linewidths in quantum cascade laser designs," *Appl. Phys. Lett.*, vol. 93, no. 141103, 2008.

[45] J. B. Khurgin *et al.*, "Role of interface roughness in the transport and lasing characteristics of quantum-cascade lasers," *Appl. Phys. Lett.*, vol. 94, no. 9, 2009.

[46] Y. Chiu, Y. Dikmelik, P. Q. Liu, N. L. Aung, J. B. Khurgin, and C. F. Gmachl, "Importance of interface roughness induced intersubband scattering in mid-infrared quantum cascade lasers," *Appl. Phys. Lett.*, vol. 101, no. 17, 2012.

[47] Y. Bai *et al.*, "Room temperature continuous wave operation of quantum cascade lasers with watt-level optical power," *Appl. Phys. Lett.*, vol. 92, no. 10, pp. 1–4, 2008.

[48] K. L. Schulte, "Defect Analysis in III-V Semiconductor Thin Films Grown by Hydride Vapor Phase Epitaxy by Defect Analysis in III-V Semiconductor Thin Films Grown by Hydride Vapor Phase Epitaxy," University of Wisconsin-Madison, 2014.

Chapter 3 λ~ 4.8 µm QCLs on InP Metamorphic Buffer Layers

3.1 Introduction

The first quantum cascade laser (QCL) demonstrated on InP was by Faist et al. [1] which yielded 8.5 mW of peak power from one facet and had a threshold current density J_{th} of 11 kA/cm^2 for a 750 µm long device. Since then, with continued optimization of QCL design and growth, InP based QCLs have emerged to be key optoelectronic devices for optical telecommunication and detection of hydrocarbons with traces in the mid-IR wavelength regime. By 2004, strain-balanced active regions had enabled QCLs for emission at 4.8 µm yielding CW power up to operating temperatures of 323K and J_{th}=1.71 kA/cm^2 with 310 mW per facet at 298 K [2]. Optimization of the bottom contact and ridge geometry along with episide-down bonding on a diamond submount were found to be effective in increasing the wallplug and thermal efficiency [3]. The step-tapered active resonant extraction (STA-RE) design for λ~ 4.8 µm resulted in 1.5 W CW power with a 4 mm long HR coated device at 287 K heatsink temperature [4]. Internal differential efficiency, η_{id}, of 77% was obtained for this device which is the largest till date in the 4.0-6.5 µm emission wavelength range, pushing it even closer to the fundamental limit of 90% [5].

A challenge remains inspite of these advancements with QCLs on InP, i.e. heteroepitaxy on Si to enable photonics, optical interconnects and complementary metal-oxide-semiconductor (CMOS) technology [6]. This will also utilize cheaper substrates (Si) instead of InP, and the existing mature fabrication technology for Si-based devices. There are primarily three possibilities for achieving III-V integration with Si: heteroepitaxial growth, flip-chip integration and wafer bonding technology. An example of the flip-chip procedure for an InGaAs/InP laser designed for emission at 1.55 µm was provided by Mitze et al. in 2005 [7]. It illustrates the use of three planes of fabrication: Si top layer involving waveguides and standoffs, buried oxide for vertical alignment

and AuSn solder bumps for electrical connections. Another approach is die-to-wafer bonding where an unprocessed III-V stack is bonded epi-side down onto a Silicon on insulator (SOI) wafer using polymer thermosetting or surface-activated oxides [8]. The InP substrate is removed and the III-V on SOI stack is processed together. As fine alignment as in the case of the flip-chip process, isn't needed, the die-to-wafer bonding saves time and expenses of III-V consumption as they are bonded per requirement. Direct wafer bonding of GaAs on Si is explored and InAs/GaAs QD lasers have been demonstrated [9]. Fabry–Perot (FP) [10] and distributed feed-back (DFB) [11] QCLs emitting at 4.6 μm have been demonstrated by wafer bonding on Silicon-on-Nitride-on-Insulator (SONOI) substrates. Transfer printing on silicon-on-sapphire has also enabled monolithic integration of mid-IR QCL on Si [12]. Precise alignment limits further advance of such techniques making it less cost-effective.

Direct growth of InP on Si is deemed not feasible due to the 8% lattice-mismatch and ~50% thermal co-efficient of expansion mismatch. Moreover, the growth of polar InP on non-polar Si can lead to the formation of two-dimensional arrays of III-III or V-V bonds in a III-V material grown on Si. The boundary between the two domains with an antiphase relation is called an antiphase boundary [13]–[15] which can be detrimental to the device performance similar to dislocations. Lau group at HKUST is a pioneer in successfully growing a variety of InP MBLs on Si [16]–[18].

To achieve heteroepitaxial growth of QCLs, metamorphic buffer layers (MBLs) involving various controlled strain relaxation techniques to reach the desired relaxed cap layer composition, are employed. To this extent, a QCL active region designed for an emission wavelength of 3.4 μm, has been successfully grown on an InGaAs MBL using metalorganic chemical vapor deposition (MOCVD) growth [19]–[21]. λ~11 μm QCLs have been demonstrated on Si employing the InAs/

AlSb material system using molecular beam epitaxy (MBE) growth [22]. λ~4.6 μm QCLs have also been demonstrated on GaAs employing the InGaAs/InAlAs material system for the active region and an InAlAs MBL, all grown by MBE [23]. λ~4.35 μm QCL on an InAlAs MBL has also recently been monolithically integrated on MBE grown InP on Si substrates with 6° miscut toward [111], additionally employing a Ge buffer to grade the lattice constant from Si to GaAs [24]. Low RMS roughness of the InP buffer layer (0.7 nm) was reported with a threading dislocation density of mid $\times 10^{8}$ cm^{-2}.

The work presented in this chapter is in collaboration with K. M. Lau group at HKUST, such that they performed the growth of InP MBLs. The surface preparation is followed by the MOCVD growth of test superlattices (SLs) and device structures at UW-Madison. A comparison of these MBLs through high resolution x-ray diffraction (HRXRD) studies is presented and the MBL providing the sharpest and the most number of SL fringes amongst them is proposed for growing a full QCL structure. MOCVD growth of InP-based QCL structures on a Si (001) substrate is demonstrated by employing a metamorphic InP buffer layer with InAs/InP quantum dots as dislocation filters. Calibration samples consist of a strain-compensated 11.98 nm $In_{0.365}Al_{0.635}As$/14.8 nm $In_{0.64}Ga_{0.36}As$ SL structure as well as 5-stages of the λ~4.8 μm QCL active region, which are grown atop the metamorphic buffer and are used to assess the structural properties of the SL through HRXRD and high-resolution transmission electron microscopy (HRTEM). Full QCL structures with the 40-stage active region are which fabricated into edge-emitting ridge-waveguide structures and demonstrate low-temperature electroluminescence (LT-EL) with a full width half maximum (FWHM) of 48.6 meV.

3.2 InP MBLs

Record high f_T and f_{max} values were obtained with an $In_{0.7}GA_{0.3}As$ metamorphic high electron mobility transistor fabricated on a GaAs substrate, making use of the low electron effective mass and high electron mobility inherent to III-V semiconductors [25]. Composite gate stacks such as Al_2O_3/InAlAs have enabled $In_{0.53}Ga_{0.47}As$ metal-oxide-semiconductor field-effect-transistors (MOSFETS) with high transconductance on Si [26]. Monolithic integration of such devices onto Si enables the use of large wafer areas and reduce excessive InP wafer costs. Using the two growth temperature steps enlisted in [27], InP buffer layers were grown on GaAs on 4" (001) Si substrates by MOCVD at HKUST. An $In_{0.53}Ga_{0.47}As$ interlayer is used to improve the surface morphology and act as a dislocation filter [16]. They find the FWHM of the InP peak by HRXRD to be 166 arcsec. They are also able to reduce the dislocation density to 1.5×10^9 cm^{-2}. This substrate will now be referred to as InP MBL1.

InP has also been grown on (001) Si with no miscut, using selective patterning and KOH etching to form V-grooves. III-V growth in these grooves alleviates the problems of antiphase domain formations and acts as a filter for dislocations and stacking faults [15]. Substrates of this kind provided by Lau group will be referred to as InP MBL2. They have recently demonstrated the first III-V semiconductor laser in the form of quantum dots grown on V-grooved Si (also known as GoVS), yielding 84 mW CW power per facet, with CW operation up to 353 K [17]. By electron channeling contrast imaging (ECCI), the dislocation density was calculated to be 7×10^7 cm^{-2}.

Another kind of metamorphic InP substrate has been grown by Lau et al, which utilizes InAs/ InAlGaAs quantum dots as dislocation filters in the InP buffer [18]. By plan view and cross-sectional TEM analysis, the dislocations were observed to be bending and annihilating reducing the top InP surface dislocation density to 3.2×10^8 cm^{-2} deduced by Ayers model.

InP MBLs with InAs/InP QD insertions [28] are used as virtual substrates for the growth of a QCL with a step-tapered active-resonant extraction design for λ~4.8 μm emission wavelength [4]. The insertions are two repetitions of seven-layer InAs/InP QDs separated by a 300 nm spacer layer of InP, which act as dislocation filters (DFL) [28]. Room temperature photoluminescence measurements showed increased intensity with the MBLs containing QD filters. These substrates provided by HKUST will be referred to as InP MBL3. While high-performance QCLs on InP substrates have been reported using either MBE or MOCVD, MOCVD is advantageous for regrowth processes, such as forming buried heterostructure devices or buried distributed feedback gratings and is widely used in the manufacturing of optoelectronic devices. Buried heterostructure lasers on InP substrates have been previously reported with this QCL design, and have demonstrated single-facet CW output powers of 2.6 W and 12% wallplug efficiency [29].

3.3 Experiment details and discussion

All growths discussed in this section are performed on a Thomas Swan 3×2" vertical close-coupled showerhead MOCVD reactor. The wafer rotation is constant at 100 rpm and reactor pressure is maintained at 100 Torr. The sources utilized are trimethyl indium (TMIn), trimethyl gallium (TMGa), trimethyl aluminum (TMAl), arsine (AsH_3) and phosphine (PH_3). We use two TMIn sources, TMIn1 for lower growth rates, switching between TMAl and TMGa for the SL layers and TMIn2 for high growth rate for growing InP buffer. The source temperature and pressures for the metalorganic (MO) sources are listed in table 3.1. Typical growth rates and V/III ratios are listed in table 3.2. Epison™ is used to maintain a constant concentration of TMIn through a controlled feedback loop.

MO Source	Temperature (°C)	Pressure (Torr)	Epison Concentration Set Point (%)
TMIn1	17	800	0.12
TMIn2	17	400	0.22
TMGa	-10	1000	-
TMAl	17	1000	-

Table 3.1 MO source conditions used for this work

Layer	Growth rate (Å/s)	V/III Precursor ratio
InGaAs	0.9-1.5	278-461
InAlAs	0.6-1.4	316-741
InP	4.8	80

Table 3.2 Typical growth rates and V/III ratios for this work [30].

3.3.1 Surface Preparation Techniques

In the case of InGaAs MBLs, chemical mechanical planarization (CMP) and wet-etching helped reduce the surface cross-hatching and in turn improved the FWHM of the SL fringes for the test structure grown atop [20]. A similar effort is made to improve the surface morphology of the InP MBLs. We performed chemical polishing (CP) and CMP on InP MBL2 (with GoVS) and optical images and atomic force microscopy images showed most improvement with the CP.

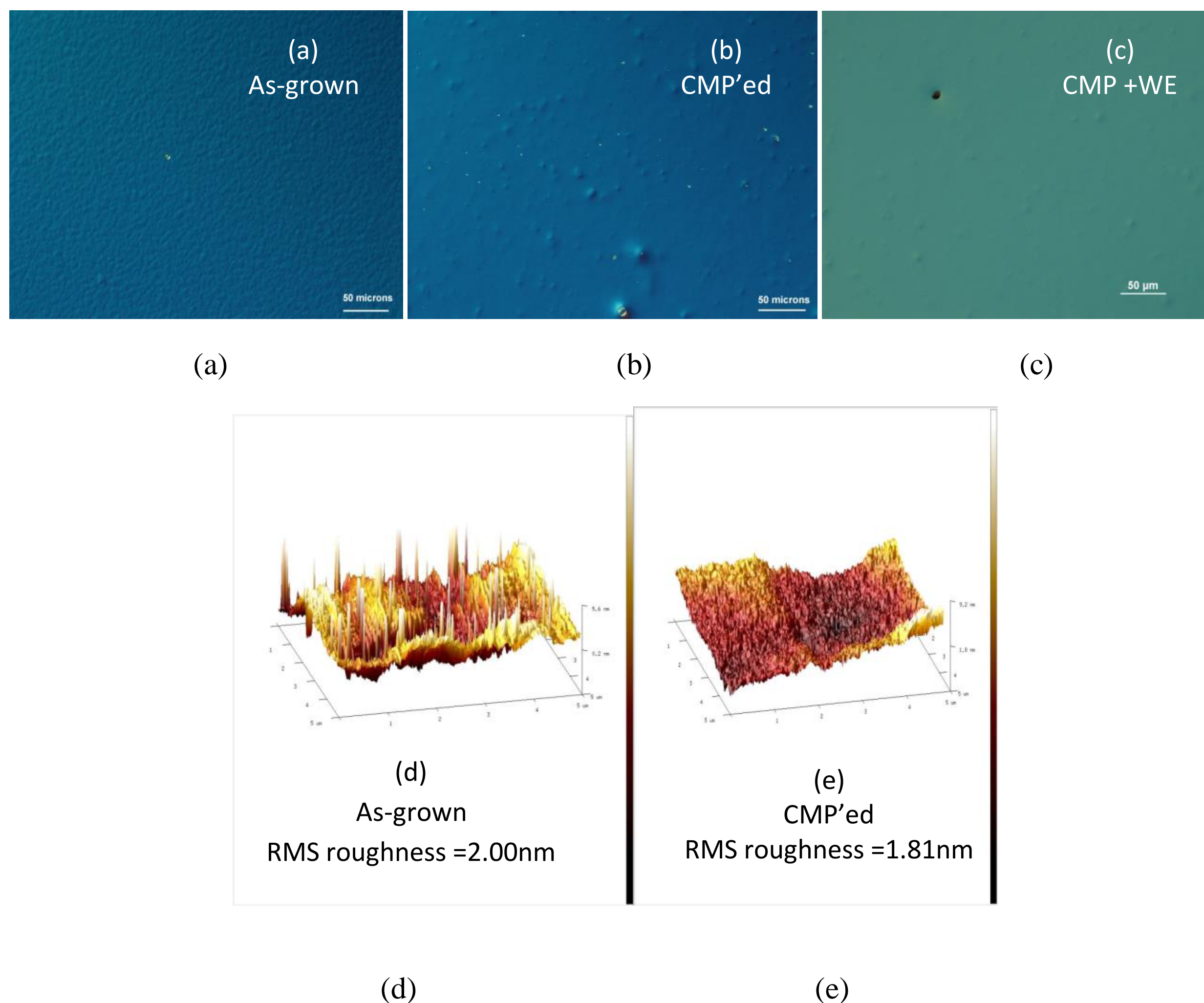

(a) (b) (c)

(d) (e)

Figure 3.1 Optical microscopy images of InP MBL2 (a) As-grown (b) after CMP (c) after CMP and wet etching; AFM (d) As-grown (e) after CMP

Chemical polishing (CP) was carried out on InP MBL3 samples to achieve a smoother surface morphology to eventually aid in obtaining highly planar SL structures. A solution consisting of 10% HCl and 90% acetic acid is used to polish for 20 minutes with an estimated removal rate of 70–100 nm/min. Figure 3.4 (a) shows the rough surface morphology of an as-grown (i.e., no CP applied) InP MBL3 with root mean square (RMS) roughness of 5.38 nm as measured from a 10×10 μm^2 AFM scan. Upon growing 2.5 µm of InP on this substrate, the RMS roughness increases to 6.89 nm for a 5×5 μm^2 AFM scan (figure 3.4 (b) and 3.3 (a)). Twenty minutes of CP is employed as surface preparation on this substrate with additional InP, which

results in an improved surface morphology (figure 3.4 (c) and 3.3 (b)) with an RMS roughness of 2.56 nm for the 5×5 μm^2AFM scan. The observed scratches were resolved by changing the polishing pad.

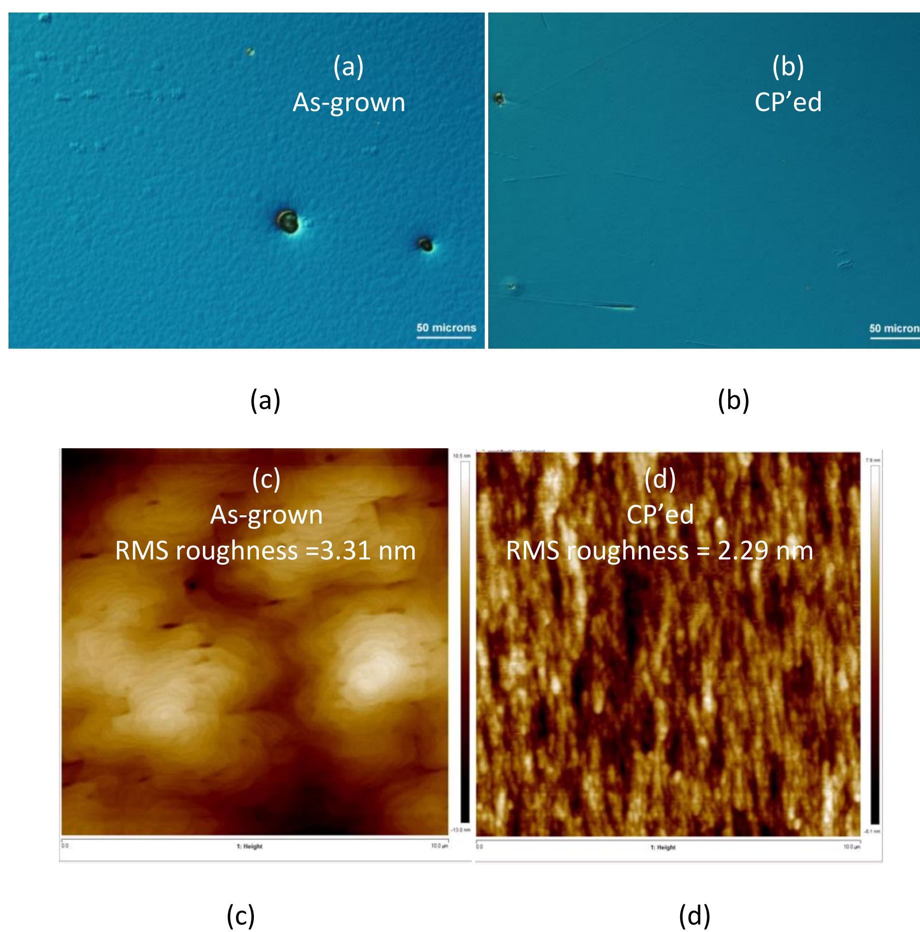

Figure 3.2 Optical microscopy images of InP MBL2 (a) As-grown (b) after CP; AFM (c) As-grown (d) after CP

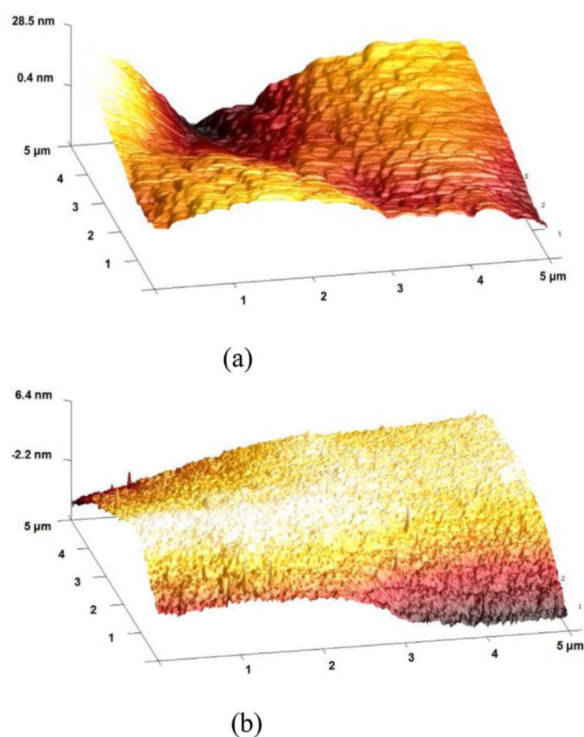

Figure 3.3 Atomic force microscopic images of InP MBL3 with (a) 2.5 µm of InP growth (b) 20 min CP subsequently.

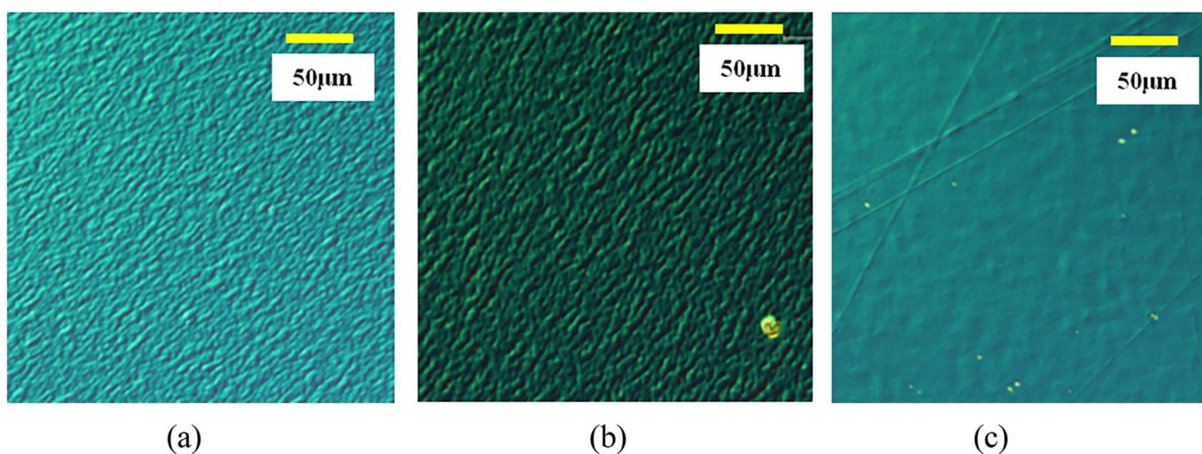

Figure 3.4 Nomarski optical images of an (a) as-grown MBL (b) MBL with 2.5 mm of InP growth (c) MBL with 20 min CP subsequently.

3.3.2 Strained Superlattice test structures

HRXRD and reciprocal space maps (RSM) were obtained using a PANalytical X'pert PRO MRD™ [31] equipped with as Ge (220) monochromator on the source side and the PANalytical

Empyrean tool. The structural characteristics of SLs grown were assessed by ω-2θ X-ray diffraction patterns about the (004) diffracted beam along with the symmetrical (004) and asymmetrical (-2-24) or (115) RSMs. The surface morphology was also monitored during the various growth steps by Nomarski optical microscope and atomic force microscopy (AFM).

Firstly, we confirmed by a (115) asymmetric HRXRD reciprocal space map that the InP layer is fully relaxed with respect to the Si substrate as shown in figure 3.5. This is important to determine the lattice constant of the top InP layer and consequently design test superlattice structures and QCLs that have low average strain. EpiTT™ emissivity corrected pyrometry [32] on SL growths done on an InP substrate and InP MBL 1 simultaneously, indicated that the surface temperature was 5 °C higher on the MBL as compared to an InP substrate. It was also observed that the SL layers were relaxed on InP MBL1 when growing 500 nm InP buffer and a 5×SL: $In_{0.41}Al_{0.59}As$ (22.5 nm)/ $In_{0.638}Ga_{0.362}As$ (24 nm).

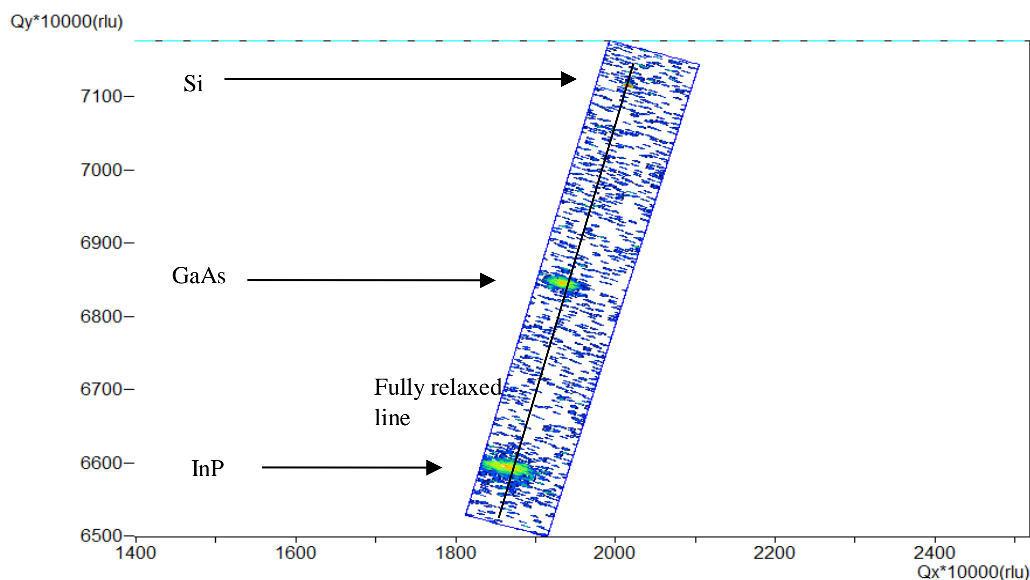

Figure 3.5 Asymmetrical HRXRD (115) reciprocal space map for InP MBL1

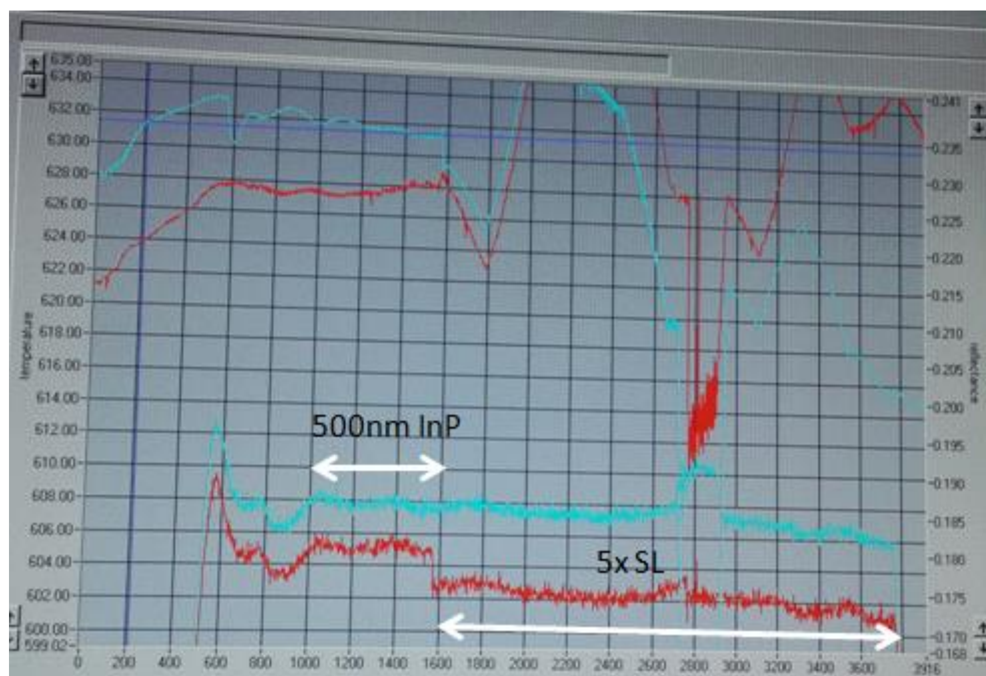

Figure 3.6 EpiTT™ reflectometer measurement during the MOCVD growth, showing the reflectance and temperature profiles as a function of time. Blue scan is for InP MBL1and the red scan is for an InP substrate, indicative of 5 °C surface temperature difference between the two substrates.

A low-strain SL test structure, which is a 10×SL: $In_{0.6}Ga_{0.4}As$ (3 nm)/ InP (31 nm), was grown on a 500 nm InP buffer layer. Owing to the low strain, HRXRD reveals good quality SL fringes as shown in figure 3.7 indicating that the layers have not relaxed. It is also important to note that the set point for the growth temperature was reduced by 5 °C.

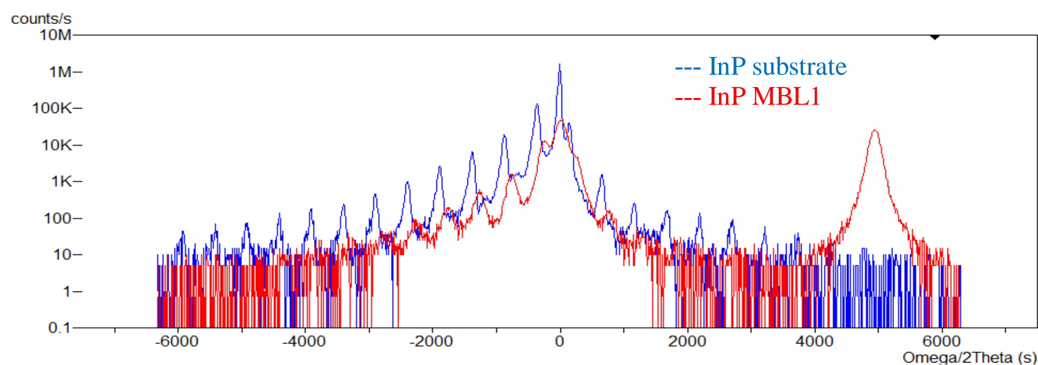

Figure 3.7 (004) HRXRD scan from the growth of a 500 nm InP buffer and 10×SL: $In_{0.6}Ga_{0.4}As$ (3 nm)/ InP (31 nm)

The high-strain SL test structure, was found to relax, when repeated at the growth temperature lowered by 5 °C, which can be attributed to the rough surface morphology of the MBL substrate. The next SL growth was modified to have half the thicknesses in order to reduce the average strain. X-ray diffraction scans show that the SL layers haven't relaxed and growing more periods of this SL does not result in a significantly higher intensity of the diffraction peaks as expected. SL layers are strained with respect to the InP MBL1 as confirmed by HRXRD RSMs in (004) and (115) axis.

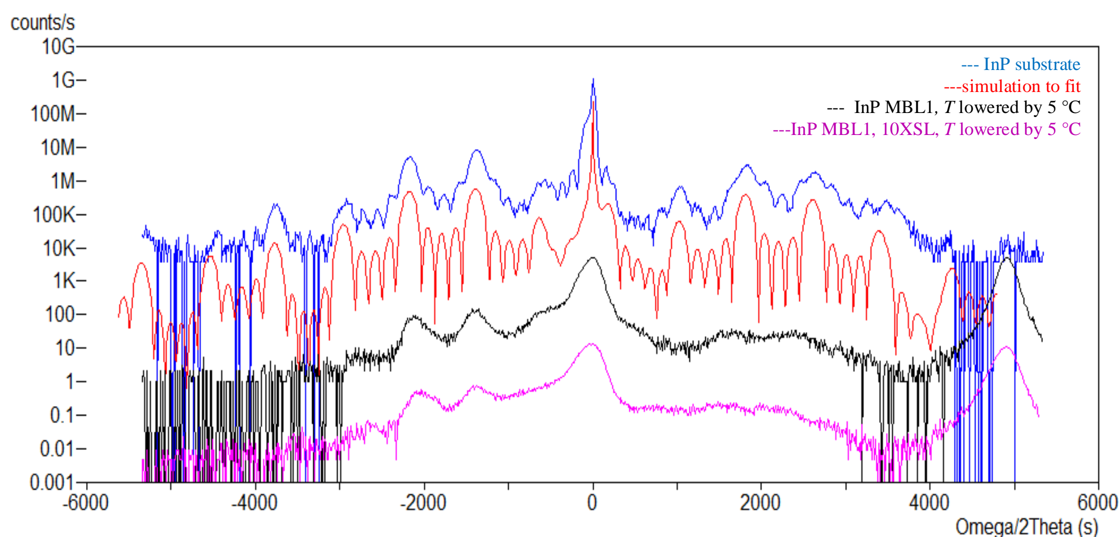

Figure 3.8 HRXRD scans and simulation to fit experimental results for the growth of 150 nm InP buffer and 5 × SL: $In_{0.39}Al_{0.61}As$ (11.48 nm)/ $In_{0.635}Ga_{0.365}As$ (11.9 nm). 10 repetitions of the same SL are indicated on the graph. Scans are offset vertically for clarity.

The InP MBL2 is expected to have up to 2 orders of magnitude lower dislocation density than MBL1, which will result in smaller FWHM of the SL fringes as seen from the x-ray diffraction scans. InP MBL3 has higher dislocation density than InP MBL2 but has a better surface morphology as seen from optical microscope images, which results in higher fidelity of HRXRD SL fringes. This comparison is depicted in figure 3.8.

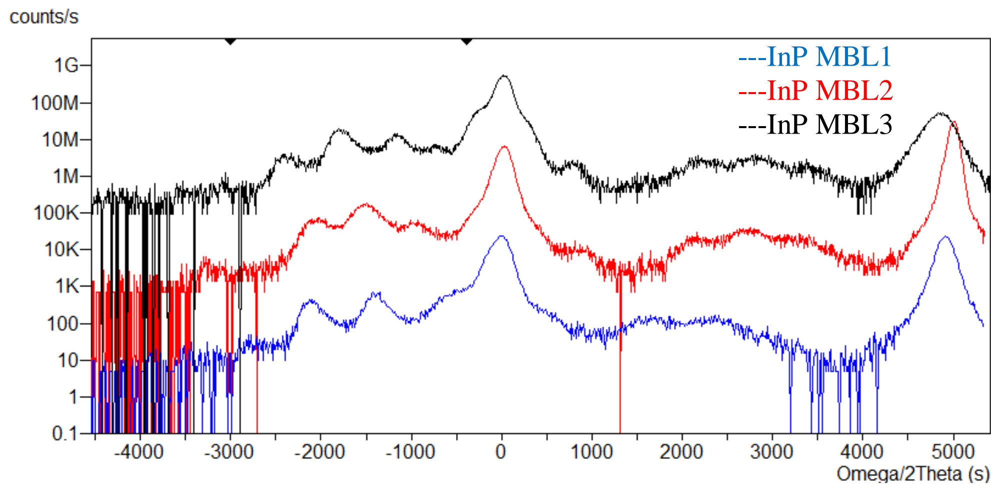

Figure 3.9 HRXRD comparison between InP MBL1, InP MBL2 and InP MBL3 for the growth of 150 nm InP buffer and 5×SL: $In_{0.39}Al_{0.61}As$ (11.48 nm)/ $In_{0.635}Ga_{0.365}As$ (11.9 nm)

3.3.3 QCL test structures and complete device growths

5-stage QCL regrowth

A simplified QCL structure in the form of 5 stages of the active region is grown on the InP MBL3. Typically, 40 stages of this active region will be grown in addition to the cladding and confinement layers to form the QCL for emission at 4.8 µm [5].

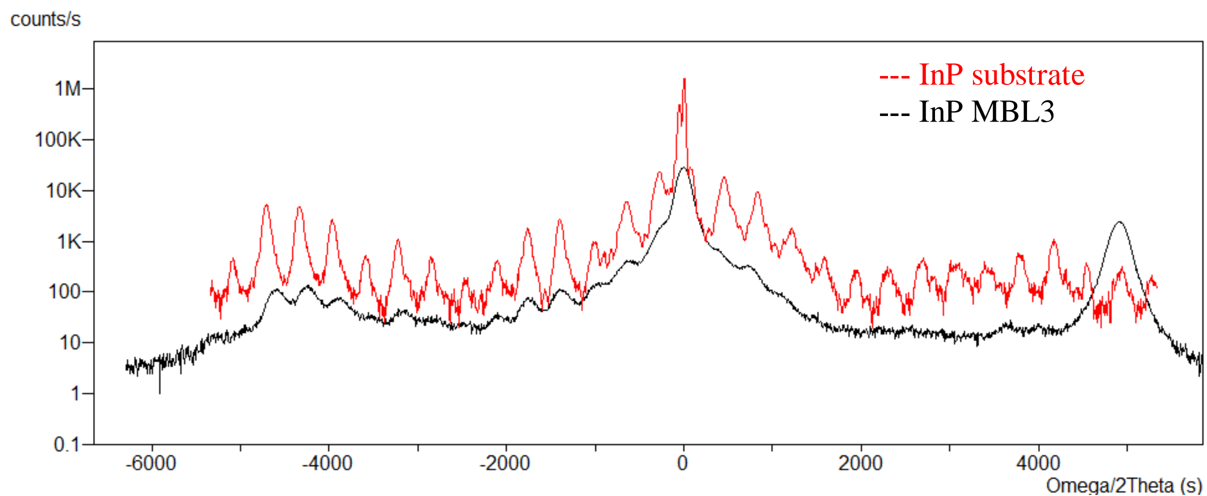

Figure 3.10 HRXRD scan for the growth of 1 µm InP buffer layer and 5 stages of the active region.

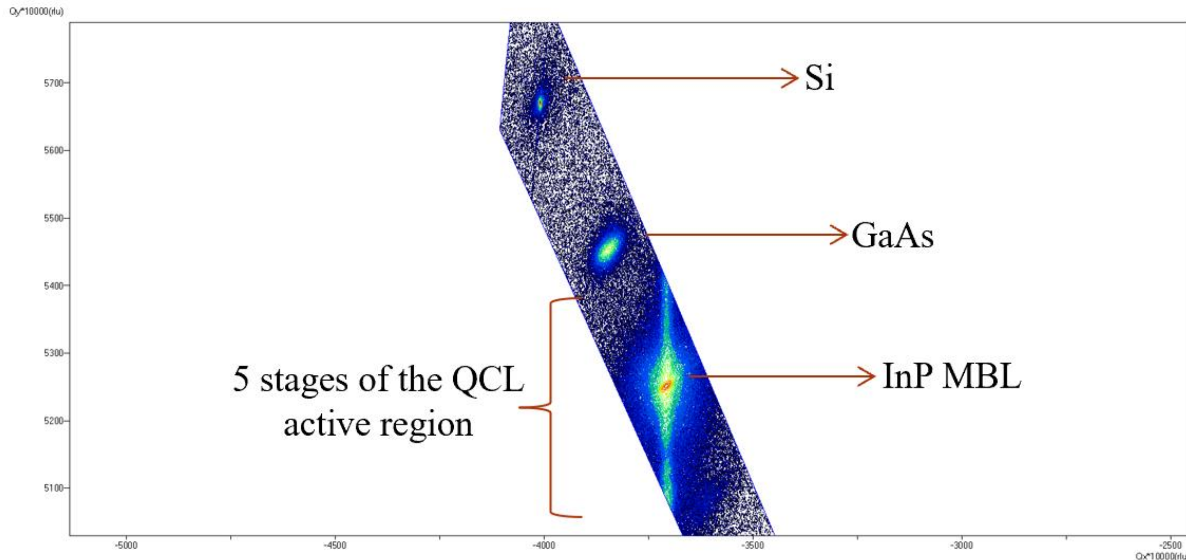

Figure 3.11 (-2-24) asymmetrical HRXRD RSM scan showing that the 5 stages of active region growth are strained with respect to InP

The growth of five stages of the active region for the QCL designed to emit at ~4.8 μm shows similar trends of HRXRD fringe broadening compared to those from the same structure grown on InP substrate (figure 3.10). (-2-24) RSM is presented in (figure 3.11) to verify that the SL layers are fully strained with respect to the InP cap on the MBL.

Room temperature photoluminescence (RT-PL) measurements were performed using a 532 nm laser with a 0.3 mm diameter spot size in the LabRAM Aramis Horiba instrument™ [33] with an InGaAs detector, to assist in comparing the active region fidelity. Initial RT-PL measurements were performed to compare the 5-stage growth on InP MBL3 versus InP substrate, taking into account the growth temperature difference (figure 3.12). It is observed that the peak PL intensity is about 10 times lower for InP MBL3 compared to the growth on an InP substrate, indicative of the high dislocation density. Moreover, some additional peaks at ~1500 nm are seen for InP MBL3 possibly due to the underlying MBL and QD structure. Multiple spectral peaks arising from the band-to-band electron–hole recombination are observed due to the various

quantum well compositions of the QCL active region. The spectral position of the peaks matches well between the InP MBL3 and InP substrate.

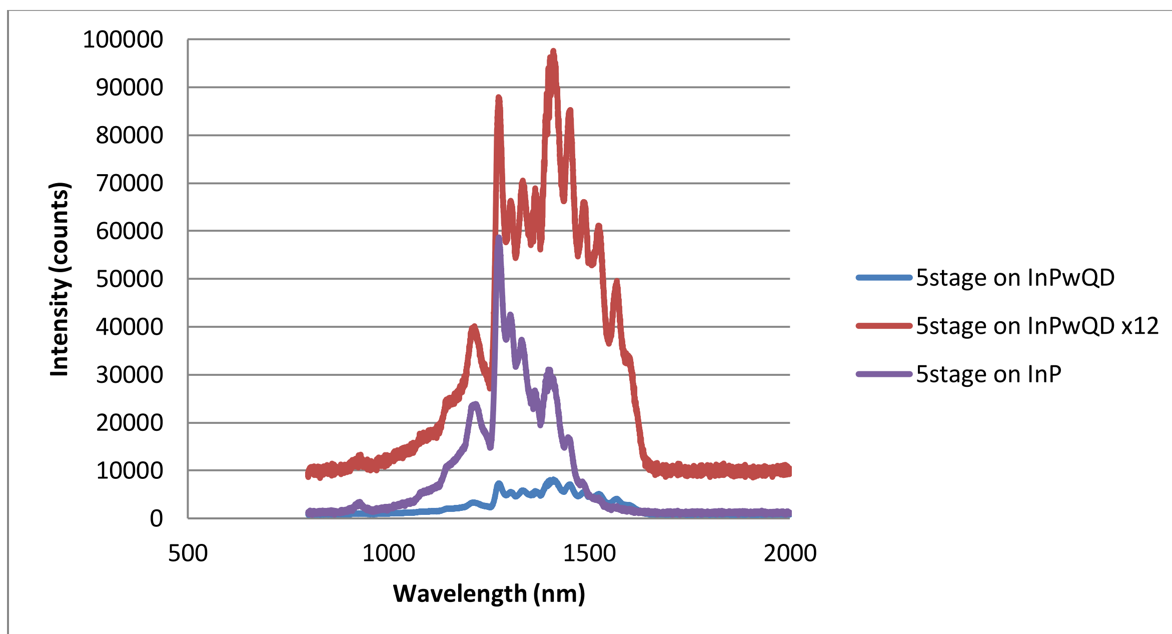

Figure 3.12 Photoluminescence measurements to compare the 5-stage growth on an InP substrate with that on the InP MBL3

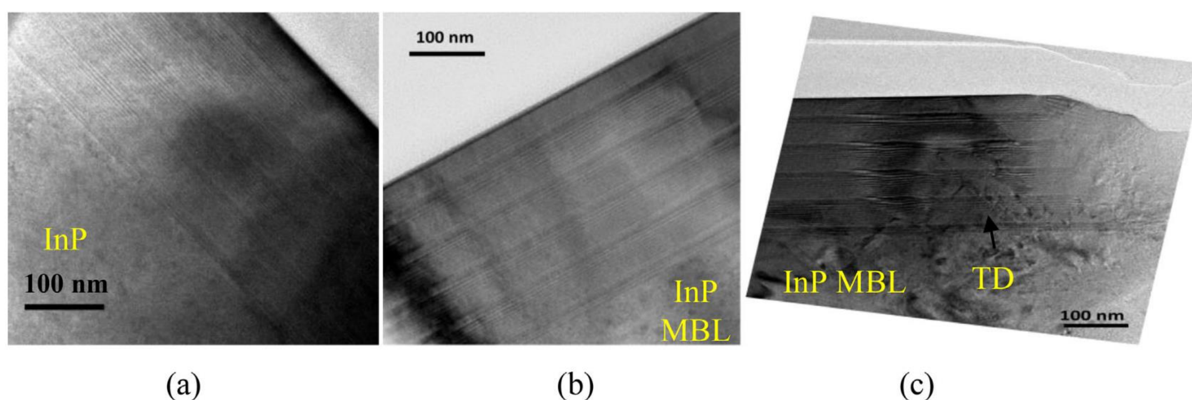

Figure 3.13 HRTEM analysis for the regrowth of 5 stages of the QCL active region a) on an InP substrate b) on the InP MBL3 c) on the InP MBL3 with threading dislocation penetrating through

HRTEM analysis reveals sections of the regrowth on the InP MBL3 (figure 3.13) to have planar interfaces and layers, as observed for the corresponding structure on the InP substrate (figure 3.13 (a)). However, there are regions on the InP MBL3 that contain TDs and large pits, and are

seen to disrupt the SLs in the vicinity of the TDs (figure 3.13 (c)). It is imperative to understand that by HRTEM, only small volumes of the sample can be analyzed. However, the intensity of the SL fringes in HRXRD data provides an averaged picture of the planarity of the SL layers and uniformity of the SL period over the XRD beam size (~1 cm height * variable width dependent on slits used). Due to the relatively high dislocation densities present, we anticipate that broadening of the XRD fringes will occur. This data clearly demonstrates the necessity to achieve low dislocation density, smooth, and planar MBL cap layers in order to avoid distortion of the SLs grown on top. Lower dislocation density is expected by implementing Aspect Ratio Trapping (ART) techniques within the buffer layer. Such techniques have demonstrated dislocation densities in the 10^7 cm^{-2} range [17].

40-stage QCL regrowth

Full QCL structures employing 40 stages of the active region were grown on CP surface-prepared InP MBL3. This sample was processed into ridge waveguide devices (25 mm wide and 3 mm long) with both electrical contacts on the epi-side to avoid current injection through the highly defective MBL and Si substrate. The control sample grown on InP is subsequently fabricated into circular mesa devices, 300 mm wide in diameter, which are consequently cleaved through the centers in half to measure the edge emission without feedback from a cavity. RT and LT (77 K) EL measurements are conducted to compare the FWHM of the emission spectral peak for the device on MBL versus that on InP substrate. These measurements are performed under pulsed-current injection (20% duty cycle) using a Fourier transform infrared (FTIR) spectrometer and cooled HgCdTe detector. To confirm the detection of transverse magnetic (TM) polarization intersubband transition, a rotating polarizer producing a sinusoidal response from the lock-in amplifier is used. Forty-stages of the QCL active region were regrown together with the InP cladding, waveguide,

and contact layers in order to obtain the full QCL structure on the InP MBL3 having received the CP surface preparation. (004) HRXRD scans show that the SL fringes line up with those seen on the InP substrate, but with much lower intensities and fringe broadening (figure 3.14). A (115) RSM was employed to ascertain that the SL within the active region stages is fully strained with respect to the InP cap of the MBL. A Nomarski optical image of the sample after the full QCL regrowth is also shown in figure 3.15 (a). The scanning electron microscopy (SEM) image in figure 3.15 (b) showed severe undulations at the interface between the top of the active region and upper confinement layer. This is an indication of possible strain relaxation in the latter stages of the active region.

EL from the ridge waveguide device on InP MBL3 was measured at 77 K with a current density of 2.67 kA/cm^2 and up to the highest current density of 9.3 kA/cm^2. The FWHM of the centered at ~5 µm (figure 3.16). Lasing is not observed up to the primary lasing transition is measured to be 48.6 meV. Interface roughness scattering is known to broaden the EL linewidth [19], [34] and is expected to be the cause for the broad transition peak in the case of lasers on InP MBL3 when compared to mesa devices on InP. More investigation is ongoing into the origin of the observed transition causing the additional narrow EL spectral feature seen at ~7.5 µm.

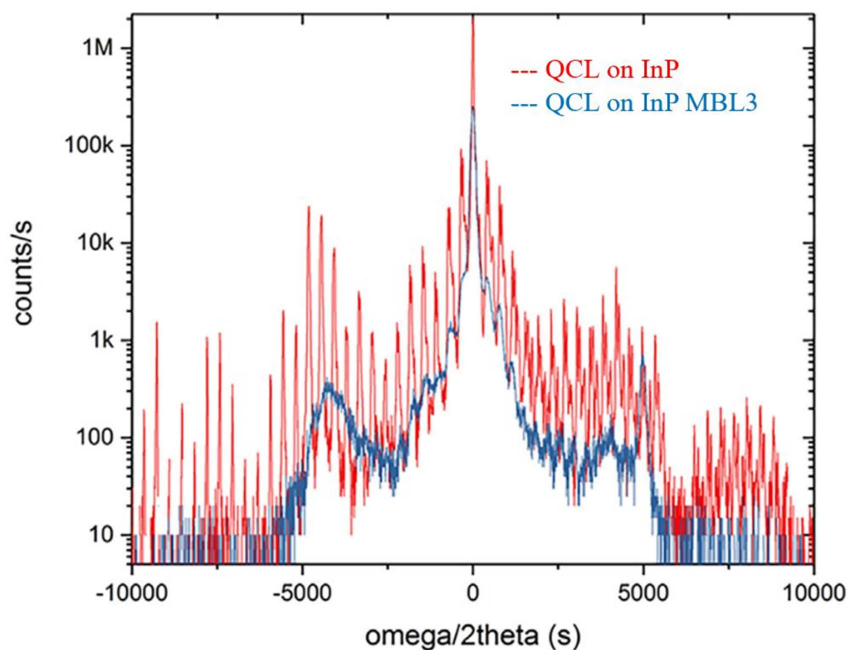

Figure 3.14 (004) HRXRD comparison of the regrowth of 40-stages of the active region on the InP MBL3 and InP

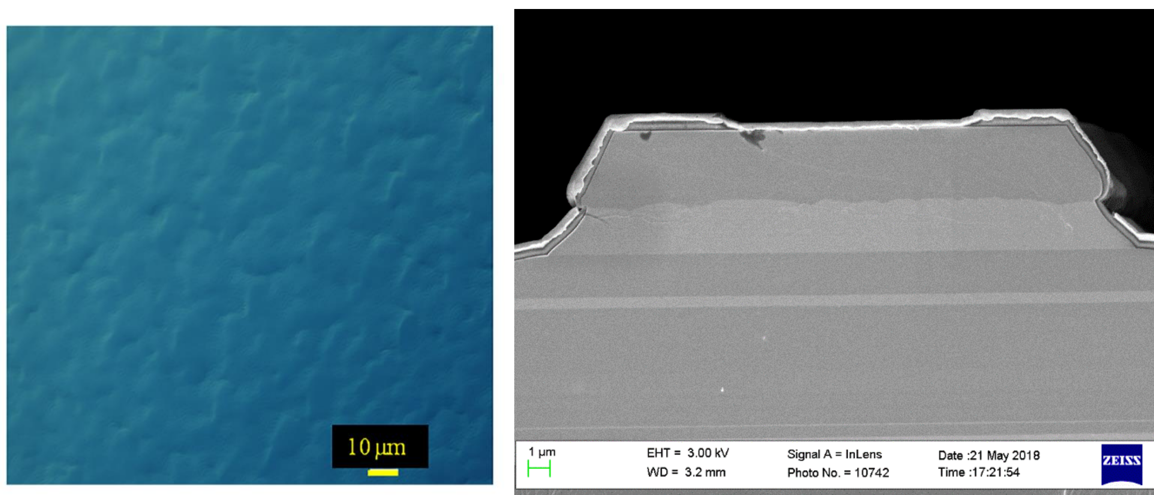

Figure 3.15 40-stage active region regrowth on InP MBL3 (a) surface morphology by a Nomarski optical image (b) SEM image showing undulations in the top stages grown towards the end of active region growth

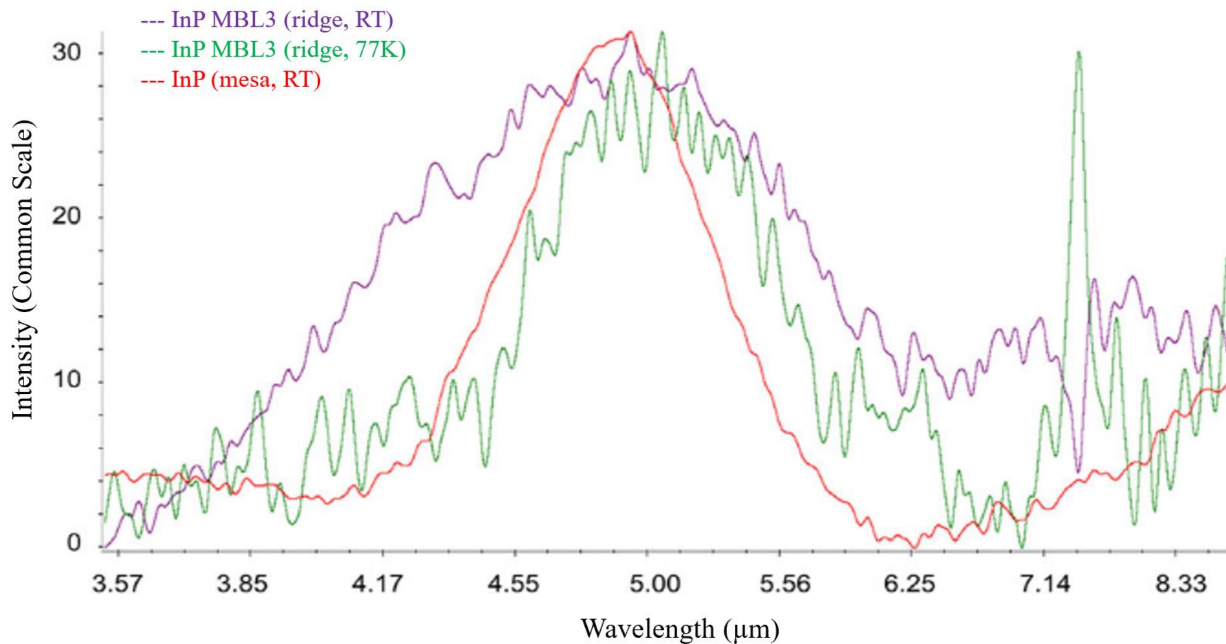

Figure 3.16 Measured EL spectra for ridge waveguide device from QCL on InP MBL3 (current density 2.33 kA/cm^2) and mesa device from QCL on InP.

20-stage QCL regrowth

Based on the SEM image of the 40-stage QCL regrowth, it appears that the last few stages of the active region, which exhibit large roughness, may have begun to relax due to accumulated net strain. The average strain per stage is 0.0026% tensile with respect to InP, which does not show observable strain relaxation on an InP substrate when measured by HRXRD. However, in the case of InP MBLs, the presence of a high density of threading dislocations at the cap layer may aggravate local strain relaxation resulting in poor SL XRD fringes and waviness in the constituent layers. To isolate the cause of the observed strain relaxation, 20-stages of the active region were regrown. Associated SEM image (figure 3.16) shows some undulations but mostly planar active region, as is desired.

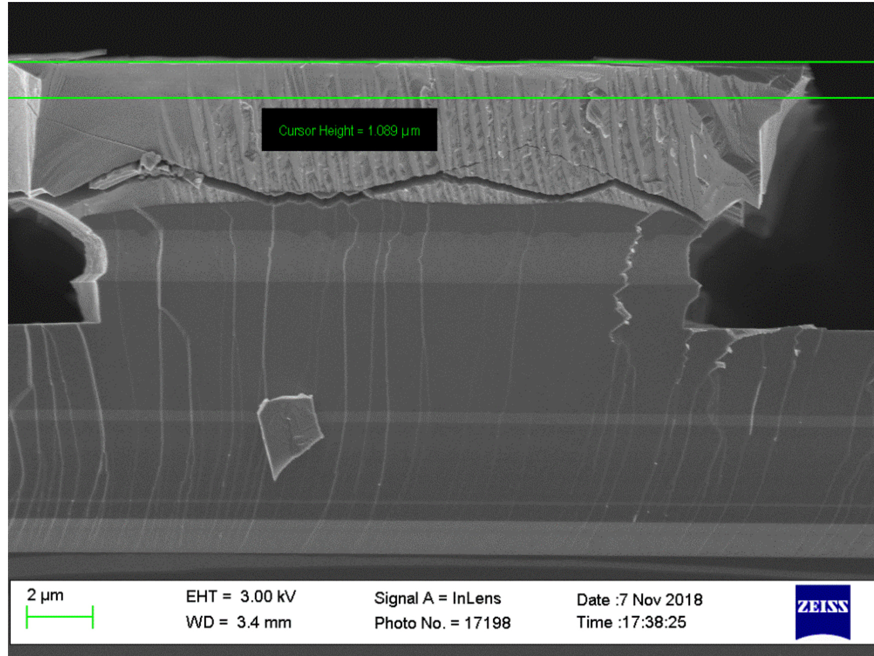

Figure 3.17 SEM image showing some undulations in the top stages grown towards the end of active region growth, but mostly planar in comparison to figure 3.15 (b)

RT-EL was obtained from ridge-waveguide devices fabricated out of the 20-stage active region regrowth at ~5 µm with a FWHM of 74.1 meV as shown in figure 3.18 (a). RT-EL from the same growth on InP typically results in a peak FWHM value of 30-35 meV. The wider EL FWHM from the device on MBL may stem from the roughness in the SL active region observed in figure 3.17. I-V characteristics of the same device grown on InP MBL and InP are compared in figure 3.18 (b). The I-V for the device on MBL exhibits a lower voltage than expected, presumably due to a current leakage path within the device. This may reflect current shunting through dislocations in the film. LT-EL is yet to be obtained for these devices. By calibrated L-I-V measurements on the 20-stage device grown on InP substrate (figure 3.18 (c)), a J_{th} of 1.89 kA/cm^2, a slope efficiency of 1.62 W/A and P_{max} of 4.65 W was obtained, ascertaining a good device growth in that run.

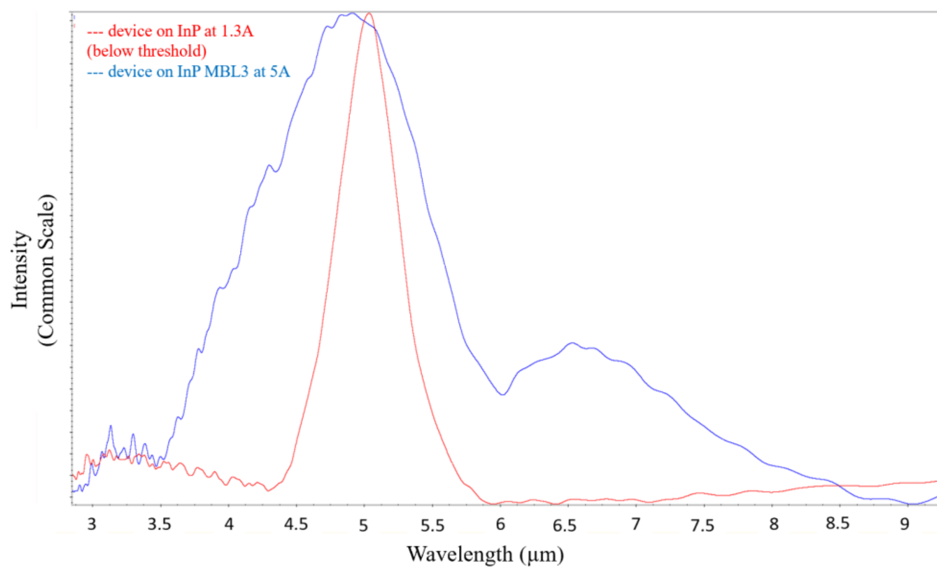

(a)

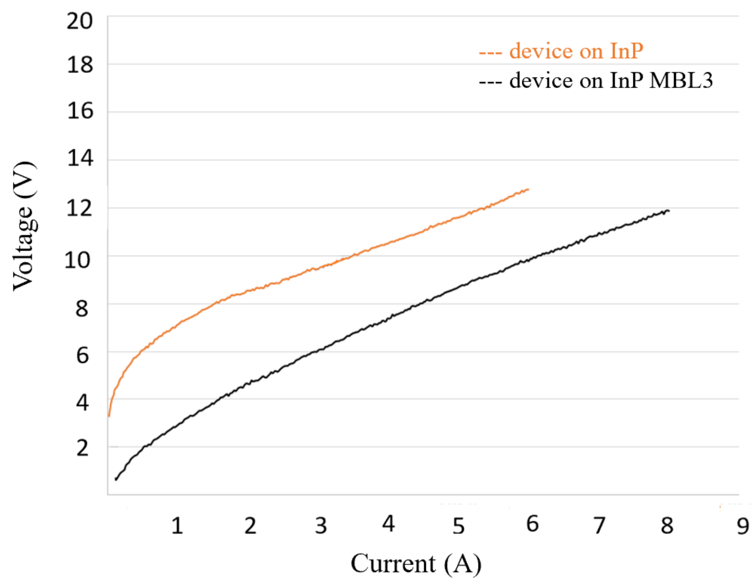

(b)

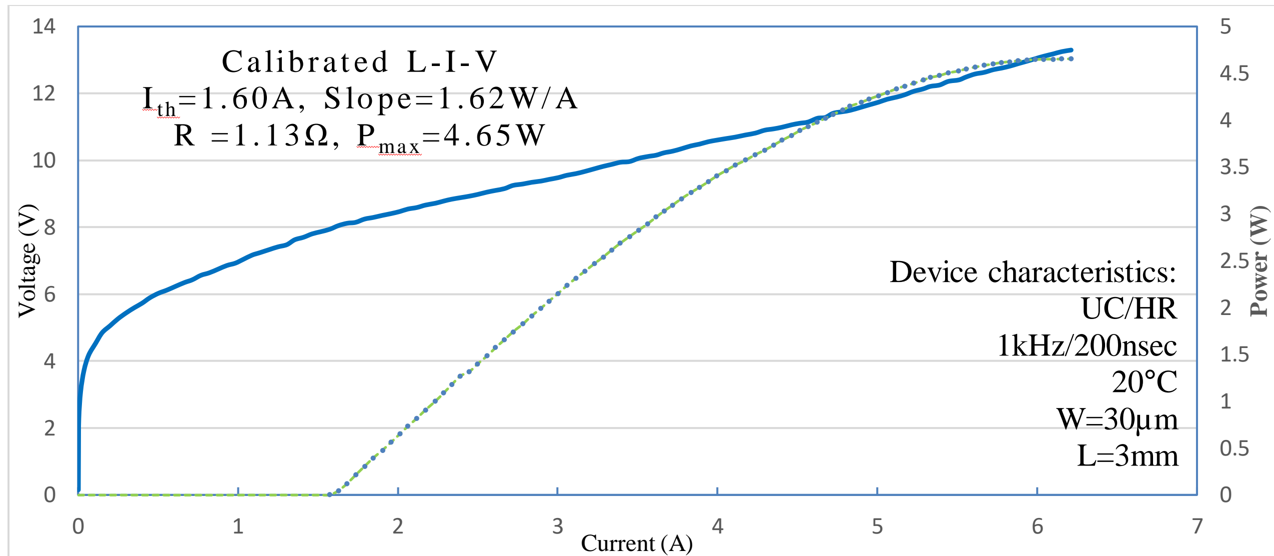

(c)

Figure 3.18 Device characterization of the 20-stage QCL regrowth (a) RT-EL measurements for devices on InP MBL3 and InP (b) I-V curves of the devices on InP MBL3 vs InP substrate (c) L-I-V curves on the InP substrate

3.4 Conclusions

Through the growth of test SL and QCL structures, InP MBL3 employing QDs as dislocation filters is shown to be the best candidate for growing the full QCL for device performance in comparison to that grown on InP substrate. RT-PL for the growth of 5-stages of the active region of the STA-QCL designed for emission at 4.8µm showed about 10 times lower intensity on the InP MBL3 indicative of the high dislocation density compared to InP. CP was effective on InP MBL2 and MBL3. These polishing procedures are expected to provide a smooth starting surface with reduced undulations for the growth of strained layers forming the QCL. HRTEM images of five stages of the QCL active region show good planarity of SL layers in selected regions while layers are highly distorted in the vicinity of a TD. Full QCL laser structure employing 40-stages of the active region was grown on the InP MBL with chemical polishing. LT-EL was observed from ridge waveguide devices at ~5 µm with a FWHM of 48.6 meV, although lasing was not observed with the driven current density of 9.3 kA/cm^2. Similar ridge-waveguide devices from the

full laser structure grown with a 20-stage active region showed a FWHM of 74.1 meV for RT-EL at ~5 µm.

Future work is focused on reducing the threading dislocation density of the InP cap layer of the MBLs (by exploring modified MBL designs such as with V-grooves Si substrates [35]) and achieving improved surface morphology (by further CP/Chemical Mechanical Polishing efforts in addition to optimization of the MBL design and growth) for the realization of mid-IR QCLs on Si using MOCVD. Nominally lattice-matched SLs and QCLs will be grown on the InP MBLs to assess the effect of threading dislocations on these structures in comparison to those grown on InP in the absence of significant net strain values.

References

[1] J. Faist, F. Capasso, D. L. Sivco, C. Sirtori, A. L. Hutchinson, and A. Y. Cho, "Quantum Cascade Laser," *Science* , vol. 264, pp. 553–556, 1994.

[2] A. Evans, J. S. Yu, S. Slivken, and M. Razeghi, "Continuous-wave operation of λ~4.8 µm quantum-cascade lasers at room temperature," *Appl. Phys. Lett.*, vol. 85, no. 12, pp. 2166–2168, 2004.

[3] M. Razeghi, "High-performance InP-based mid-IR quantum cascade lasers," *IEEE J. Sel. Top. Quantum Electron.*, vol. 15, no. 3, pp. 941–951, 2009.

[4] D. Botez *et al.*, "High internal differential efficiency mid-infrared quantum cascade lasers," *Proc. SPIE*, vol. 10123, p. 101230Q1-12, 2017.

[5] J. D. Kirch *et al.*, "86% internal differential efficiency from 8 to 9 microns-emitting, step-taper active-region quantum cascade lasers," *Opt. Express*, vol. 24, no. 21, pp. 24483–24494, 2016.

[6] T. Li, M. Mastro, and A. Dadgar, *III-V Compound Semiconductors: Integration with Silicon-based Microelectronics*, 1st ed. CRC Press, 2011.

[7] T. Mitze *et al.*, "Hybrid integration of III/V lasers on a Silicon-on-Insulator (SOI) optical board," *2005 IEEE Int. Conf. Gr. IV Photonics*, vol. WA1 Plenar, pp. 1–3, 2005.

[8] G. Roelkens *et al.*, "III-V/Si photonics by die-to-wafer bonding," *Mater. Today*, vol. 10, no. 7–8, pp. 36–43, 2007.

[9] K. Tanabe, K. Watanabe, and Y. Arakawa, "III-V/Si hybrid photonic devices by direct

fusion bonding," *Sci. Rep.*, vol. 2, no. 349, pp. 1–6, 2012.

[10] A. Spott *et al.*, "Quantum cascade laser on silicon," *Optica*, vol. 3, no. 5, pp. 545–551, 2016.

[11] A. Spott *et al.*, "Heterogeneously Integrated Distributed Feedback Quantum Cascade Lasers on Silicon," *Photonics*, vol. 3, no. 35, pp. 1–10, 2016.

[12] S. Jung, J. Kirch, J. H. Kim, L. J. Mawst, D. Botez, and M. A. Belkin, "Quantum cascade lasers transfer-printed on silicon-on-sapphire Quantum cascade lasers transfer-printed on silicon-on-sapphire," *Appl. Phys. Lett*, vol. 111, no. 211102, pp. 1–5, 2017.

[13] D. Cohen and C. B. Carter, "Structure of the (110) antiphase boundary in gallium phosphide," *J. Microsc.*, vol. 208, no. 2, pp. 84–99, 2002.

[14] V. Narayanan, S. Mahajan, K. J. Bachmann, V. Woods, and N. Dietz, "Antiphase boundaries in GaP layers grown on (001) Si by chemical beam epitaxy," *Acta Mater.*, vol. 50, pp. 1275–1287, 2002.

[15] M. Paladugu *et al.*, "Site selective integration of III-V materials on Si for nanoscale logic and photonic devices," *Cryst. Growth Des.*, vol. 12, pp. 4696–4702, 2012.

[16] Q. Li, X. Zhou, C. W. Tang, and K. M. Lau, "Material and Device Characteristics of Metamorphic In0.53Ga0.47As MOSHEMTs Grown on GaAs and Si Substrates by MOCVD," *IEEE Trans. Electron Devices*, vol. 60, no. 12, pp. 4112–4118, 2013.

[17] J. Norman *et al.*, "Electrically pumped continuous wave quantum dot lasers epitaxially grown on patterned, on-axis (001) Si," *Opt. Express*, vol. 25, no. 4, pp. 3927–3934, 2017.

[18] B. Shi, Q. Li, and K. M. Lau, "Self-organized InAs/InAlGaAs quantum dots as dislocation filters for InP films on (001) Si," *J. Cryst. Growth*, vol. 464, pp. 28–32, 2017.

[19] A. Rajeev, C. Sigler, T. Earles, Y. V. Flores, L. J. Mawst, and D. Boteza, "Design considerations for λ ~ 3.0- to 3.5-µm-emitting quantum cascade lasers on metamorphic buffer layers," *Opt. Eng.*, vol. 57, no. 1, p. 011017, 2018.

[20] A. Rajeev *et al.*, "Regrowth of quantum cascade laser active regions on metamorphic buffer layers," *J. Cryst. Growth*, vol. 452, pp. 268–271, 2016.

[21] L. J. Mawst *et al.*, "Low-strain, quantum-cascade-laser active regions grown on metamorphic buffer layers for emission in the 3.0–4.0 µm wavelength region," *IET Optoelectron.*, vol. 2013.0060, no. 10.1049, pp. 1–8, 2013.

[22] H. Nguyen-van *et al.*, "Quantum cascade lasers grown on silicon," *Sci. Rep.*, vol. 8:7206, pp. 1–8, 2018.

[23] R. Go *et al.*, "Room temperature operation of quantum cascade lasers monolithically integrated onto a lattice-mismatched substrate," *Appl. Phys. Lett*, vol. 112, no. 031103, pp. 2–6, 2018.

[24] R. Go *et al.*, "InP-based quantum cascade lasers monolithically integrated onto silicon," *Opt. Express*, vol. 26, no. 17, pp. 22389–22393, 2018.

[25] D.-H. Kim, B. Brar, and J. a. Del Alamo, “fT = 688 GHz and fmax = 800 GHz in Lg = 40 nm In0.7Ga0.3As MHEMTs with gm_max > 2.7 mS/μm,” *2011 Int. Electron Devices Meet.*, vol. 13, no. 6, p. 13.6.1-13.6.4, 2011.

[26] X. Zhou, Q. Li, C. W. Tang, and K. M. Lau, “30nm enhancement-mode In0.53Ga0.47As MOSFETs on Si substrates grown by MOCVD exhibiting high transconductance and low on-resistance,” *Tech. Dig. - Int. Electron Devices Meet. IEDM*, vol. 32, no. 5, pp. 1–4, 2012.

[27] C. W. Tang, H. Li, Z. Zhong, K. L. Ng, and K. M. Lau, “Hetero-epitaxy of III-V compounds lattice-matched to InP by MOCVD for device applications,” *Conf. Proc. - Int. Conf. Indium Phosphide Relat. Mater.*, vol. TuA2.6, pp. 136–139, 2009.

[28] B. Shi, Q. Li, and K. M. Lau, “Epitaxial growth of high quality InP on Si substrates : The role of InAs / InP quantum dots as effective dislocation filters,” *J. Appl. Phys.*, vol. 123, no. 193104, 2018.

[29] D. Botez *et al.*, “High-efficiency, high-power mid-infrared quantum cascade lasers,” *Opt. Mater. Express*, vol. 8, no. 5, pp. 1378–1398, 2018.

[30] J. D. Kirch, “High Performance Mid-Infrared-Emitting Quantum Cascade Lasers,” University of Wisconsin-Madison, 2017.

[31] “https://www.malvernpanalytical.com/en/products/product-range/xpert3-range/xpert3-mrd.” .

[32] “Laytec in situ metrology.” [Online]. Available: http://www.laytec.de/epitt.

[33] “https://www.horiba.com/fileadmin/uploads/Scientific/Documents/Raman/aramisbro.pdf.”

[34] A. Wittmann, Y. Bonetti, J. Faist, E. Gini, and M. Giovannini, “Intersubband linewidths in quantum cascade laser designs,” *Appl. Phys. Lett.*, vol. 93, no. 141103, 2008.

[35] S. Zhu, B. Shi, Q. Li, and K. M. Lau, “Room-temperature electrically-pumped 1.5μm InGaAs / InAlGaAs laser monolithically grown on on-axis (001) Si,” *Opt. Express*, vol. 26, no. 11, pp. 14514–14523, 2018.

Chapter 4 Atom Probe Tomography for Interface Analysis

4.1 Introduction

Atom Probe Tomography (APT) relies on the field evaporation of ions (one at a time) from a needle-shaped specimen to provide three-dimensional (3D) chemical and spatial information. It initially began as a specialized high-field physics and surface science experiment but now finds application in numerous academic and industrial research labs. APT can resolve features from 100 nm to 0.5 nm (or less in-depth profiling). Its detection limit finds a nice range to cover in between energy dispersive x-ray spectroscopy (EDS) and secondary ion mass spectroscopy (SIMS) techniques (~10-100 ppm) [1]. Common applications include composition profiling, microstructure analysis, the study of clusters and precipitates and interface analysis which will be discussed in detail. T. Tsong et al. first reported photon assisted field ionization in the 1970s [2], [3]. This was followed by the invention of pulsed laser atom probe (PLAP) with nanosecond pulses [4] and further enhancements in the laser pulse reducing the heating and improving the mass resolution by femtosecond pulses [5], [6]. Local electrode atom probe (LEAP) can analyze much larger volumes than PLAP, with lower extraction voltages, leading to higher repeatability of experiments and better mass resolution [7].

Typically, quantum cascade lasers (QCLs) contain active regions consisting of ~30-40 repetitions of a motif composed of quantum wells and barriers of various thicknesses (typically 1-5 nm each) and compositions [8]. A desirable feature of QCLs, being intersubband transition devices, is the tunability of the emission wavelength through changes in the thickness and composition of the layers within a chosen material system. However, these structures are sensitive to small deviations from the designed thickness and composition, that can result in changes in the electron wavefunctions in the conduction band and, consequently, an altered emission wavelength

of QCL [9]. Moreover, for strain-compensated SLs, minor thickness variations can lead to an imbalance in the overall strain-thickness product, which may result in strain relaxation of the several microns thick active region. Simulation of x-ray diffraction (XRD) data provides details about the average compositions and periodicity in the SL layers. Transmission electron microscopy (TEM) provides details of the atomic structures of the layers and interfaces, most readily in 2D projections. Near-atomic-resolution compositional mapping in 3D is more challenging in TEM [10]. We have utilized APT on InGaAs/InAlAs strained-bilayer SL structures grown by metalorganic chemical vapor deposition (MOCVD) to help elucidate the morphologies and compositional sharpness of the interfaces they contain. Prior studies on a nominally lattice-matched (LM) SL showed an In-rich InAlGaAs interfacial layer leading to excess compressive strain from InAlAs to InGaAs layers. The quaternary alloy grading when included in the bandstructure simulations, explained the observed red-shifted emission wavelength for LM QCLs grown on InP [9]. Similar asymmetry was observed between InGaN/GaN and GaN/InGaN interfaces in a multiple QW structure grown on (0001) GaN substrates [11].

4.2 Principle of operation

The operating principle for APT evolved from field desorption microscopy (FDM). Both these processes consist of two primary actions: field-induced ionization and desorption. Together this can be referred to as field evaporation. The applied electric field is believed to pull the negative charge towards the specimen interior with the positively charged ions on the surface. As the field increases and with thermal activation, the energy barrier is overcome by the ions which now accelerate towards the detector. Complete ionization at some critical distance and evaporation upon overcoming a field dependent Schottky barrier is proposed by Muller [12] whereas

continuous charge drainage evaporation is an alternative field evaporation mechanisms [13]. The height of the field-dependent energy barrier can be expressed as:

$$Q(F) = Q_0 - \sqrt{\frac{n^3 e^3}{4\pi\varepsilon_0} F} \quad 4.1$$

where Q_0 is the energy required to evaporate an atom from the tip in the absence of an applied field and ionize it *n* times[1] and *F* is the applied field. The evaporation rate, described by Arrhenius law is:

$$\Phi_{evap} = v_0 e^{-\frac{Q(F)}{k_B T}} \quad 4.2$$

where v_0 is the frequency of the component of vibration of atoms due to thermal agitation, normal to the surface [1] and *T* is the absolute temperature. Also, the evaporation field, F_{evap} is an important characteristic of constituent materials in a specimen. It is the field at which the energy barrier becomes zero and is dependent on the charge state of the ion. It is calculated as:

$$F_{evap} = \frac{4\pi\varepsilon_0}{n^3 e^3} (\Lambda + \sum_n I_n - n\phi_e)^2 \quad 4.3$$

where Λ is the sublimation energy, I_n is the nth ionization energy and ϕ_e is the work function of the surface emitting the ion [1]. F_{evap}, in addition to many other parameters discussed later, helps determine if there is a possibility of preferential evaporation. Although it hasn't been clearly defined for alloys or complex ions, the F_{evap} values for the constituent species in this study are listed in table 4.1

Element	Isotope Mass number*	F_{evap} **, [1] (V/nm)
Al	27	19
Ga	69	15
In	115	12
As	75	46

Table 4.1: Evaporative fields are listed for the primary elements under consideration in the materials studied (except P) [14] *Most abundant isotope listed in case of multiple isotopes **For single charge state

The electric field induced at the tip is given by:

$$F = \frac{V}{k_F R} \quad 4.4$$

where V is the high positive voltage at the tip, R is the radius of curvature and k_F is the field factor accounting for the tip shape and its electrostatic environment [1].

Two primary modes of evaporation exist:

1. Voltage Pulsing: increasing electric field with the temperature kept constant, often equated to stress pulsing

2. Laser pulsing: increasing temperature with the electric field kept constant, eliminates the stress pulsing component

The detection rate is defined as the average number of ions detected per pulse and is estimated by:

$$\Phi_D = \int_{-\infty}^{\infty} \Phi_{evap}(t)dt \times \varepsilon_D \times N_{at} \quad 4.5$$

where ε_D is the detector efficiency (known for a given instrument) and N_{at} is the number of atoms on the surface of the tip that can be evaporated, assuming all have an equal probability of evaporation.

4.3 Experimental Setup

A CAMECA 3000X Si local electrode atom probe (LEAP)™ instrument (figure 4.1) was employed for the experiments described in this chapter.

Figure 4.1: CAMECA 3000X Si™ instrument at the UW-Madison campus

An APT experiment results in two key pieces of information that are then used to uniquely identify the position and chemical identity of each ion detected, namely the time of flight (mass spectroscopy) and co-ordinates of ion detection on the detector. t_{pulse} denotes the time at which the laser pulse triggers field evaporation of ions from the specimen and t_{event} denotes the time at which the ion reaches the detector. With t_{pulse} and t_{event}, the time of flight can be determined in order to assign a unique chemical identity to the ion.

An incoming ion hits the walls of an angled channel maintained at high voltages such that the cascading of electrons causes the MCP to act as an electron amplifier. This electron cloud is

then focused on conductive lines forming a delay line detector. The x and y co-ordinates of the detected ion are deduced from the time it takes the electrical signals to reach the endpoint of the delay lines. A third delay line is used to separate multiple hits and reduce the dead time.

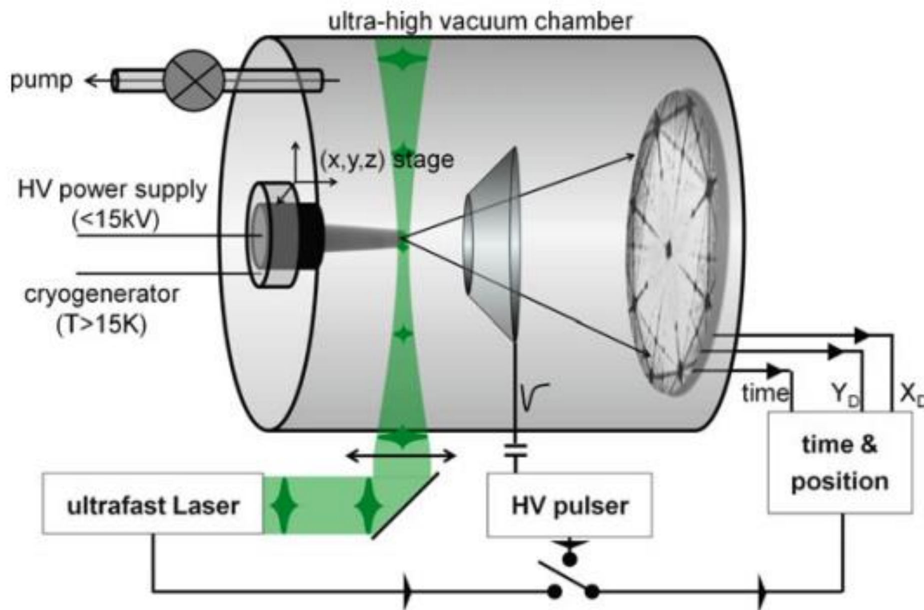

Figure 4.2: Schematic showing key components of the experimental setup [1]

$In_{1-x}Ga_xAs/In_{1-y}Al_yAs$ strained SL samples with the target characteristics illustrated in figure 4.3 were grown on (001)-oriented InP substrates. The sample designs included a thick (43.5 nm) motif SL composed of five repetitions of $In_{0.37}Al_{0.63}As$ (20.1 nm)/$In_{0.67}Ga_{0.33}As$ (23.4 nm) with 1% tensile/compressive strain relative to the InP substrate, nominally and respectively, and a thin (4.1 nm)-motif SL composed of 124 repetitions of $In_{0.44}Al_{0.56}As$ (1.9 nm)/$In_{0.6}Ga_{0.4}As$ (2.2 nm) nominally strained +0.56%/−0.47% relative to the substrate, respectively.

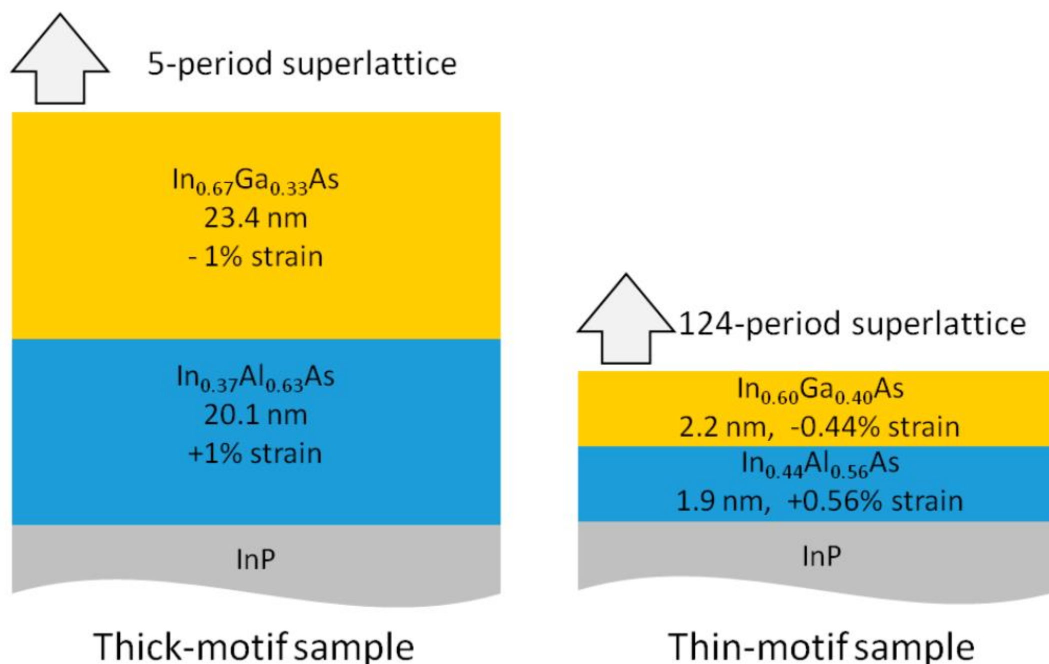

Figure 4.3 Schematic diagrams of the motif characteristics of the superlattice samples [15]

Both SL samples were grown in a close-coupled showerhead metalorganic chemical vapor deposition (MOCVD) reactor at a reactor pressure of 100 Torr and at a temperature of 605 °C, with a wafer rotation of 100 rpm. The growth rates and V:III precursor ratios are listed in table 4.2. The interruption time for switching between the SL layers was 5 s. Conventional sources trimethyl gallium ($(CH_3)_3Ga$, TMGa), trimethyl indium ($(CH_3)_3In$, TMIn), trimethyl aluminum ($(CH_3)_3Al$, TMAl), arsine (AsH_3) and phosphine (PH_3) comprised the precursors.

Material	V:III Precursor Ratio	Growth Rate (nm/s)
Thick-motif SL		
$In_{0.37}Al_{0.63}As$	428	0.10
$In_{0.67}Ga_{0.33}As$	315	0.14
Thin-motif SL		
$In_{0.44}Al_{0.56}As$	375	0.12
$In_{0.60}Ga_{0.40}As$	387	0.11

Table 4.2 Growth rates measured in calibration runs for V:III precursor ratios used to grow each superlattice (SL)

Taking into account the total volume upstream of the susceptor and the total precursor fluxes, which are dominated by the hydrogen carrier gas, the calculated precursor residence time was about 0.4 s, well below the interruption time of 5 s. These growth procedures resulted in the first-to-be-grown layers of the thick-motif SL being annealed at 605 °C for approximately 1900 s (about 32 min), and in the thin-motif SL for 5700 s (about 95 min).

The structural and microstructural characteristics of these two SLs were investigated using HRXRD and APT. ω-2θ X-ray diffraction patterns about the (004) diffracted beam were obtained at a step size of 0.002° using a PANalytical X'pert materials research diffractometer (MRD)™ [16] equipped with as Ge (220) monochromator on the source side. Needle-shaped atom probe specimens were prepared using conventional focused-ion-beam (FIB) lift-out and sharpening methods [1]. A 30 kV Ga+ beam was used for cutting, mounting, and initial shaping of the specimens; a 2 kV, 100 pA Ga+ beam was used for final sharpening as shown in figure 4.4. The long axis of the specimens was approximately parallel to the [001] growth direction of the SL and the z-axis of atom probe tomographs.

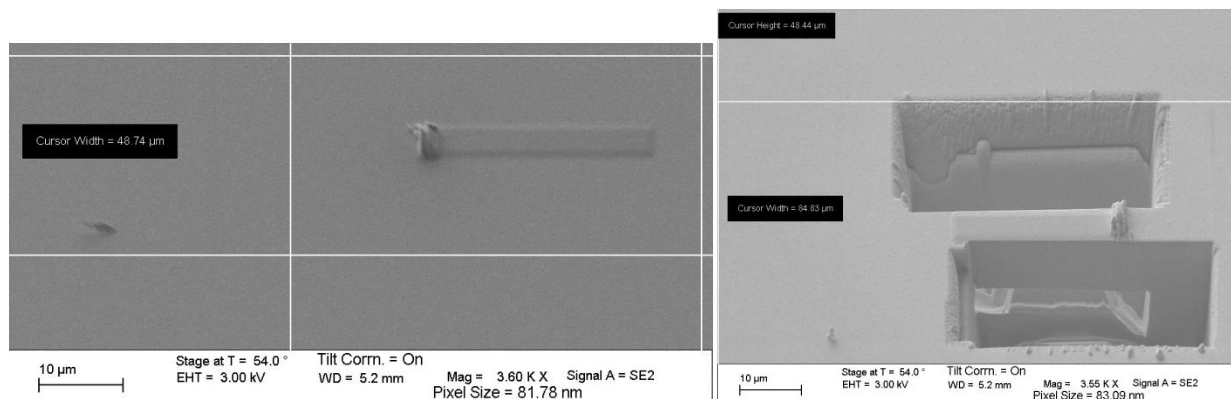

(a) (b)

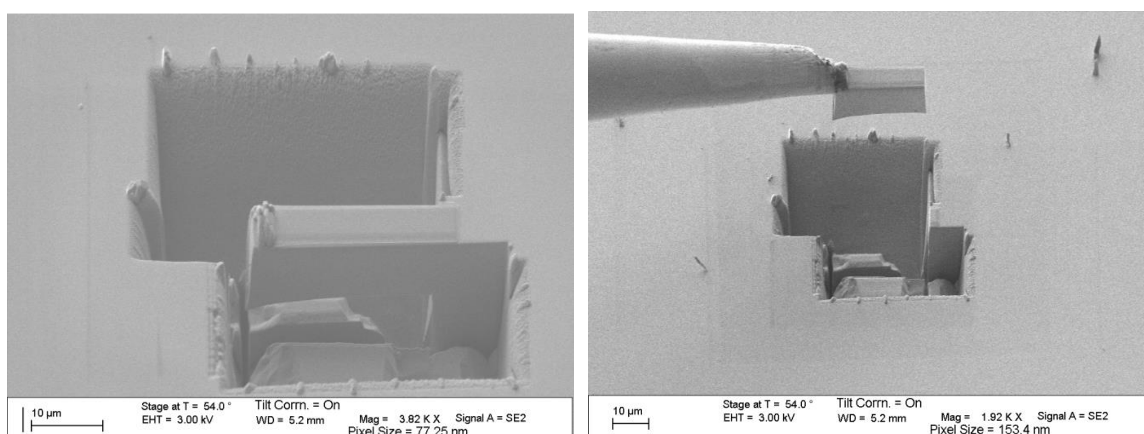

(c) (d)

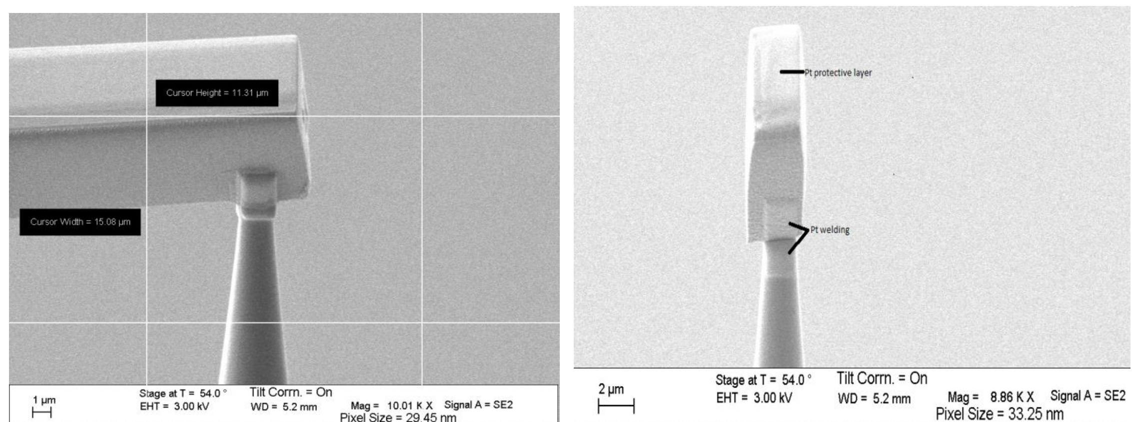

(e) (f)

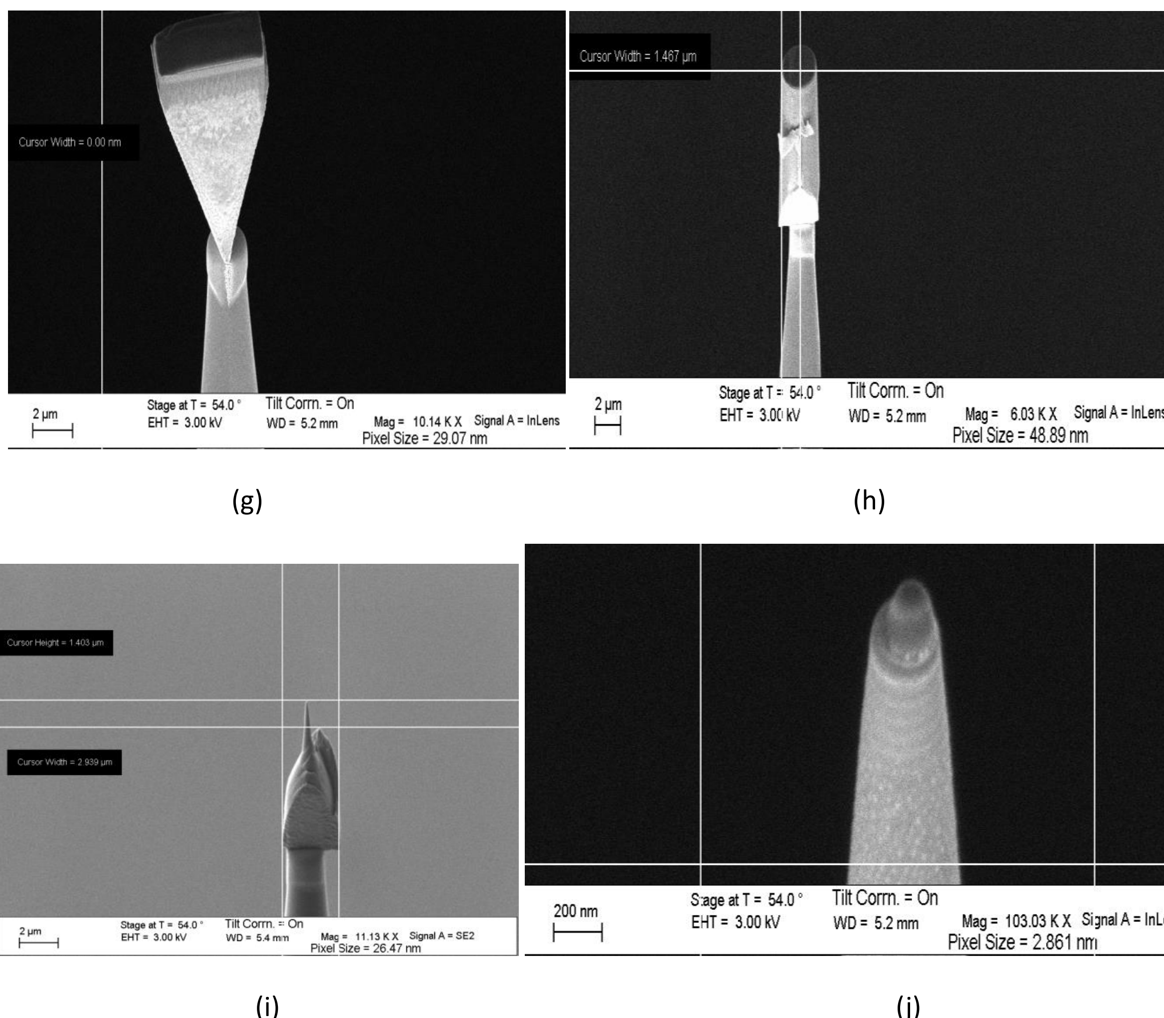

Figure 4.4 Preparation of an APT specimen by FIB lift out technique (a) deposition of a Pt cap over the wedge of interest; (b) wedge formation by milling at 30° to the normal; (c) weld the micromanipulator to one side of the now-released wedge; (d) mill the other side of the wedge to complete lift-off; (e) Pt welding of the wedge onto a Si micropost; (f) milled to separate one specimen from the wedge; (g) 90° rotated view of (f); (h) one of the many annular milling steps to form a tip; (i) further annular milling showing tip formation on the micropost with some material protrusions needing clean-up; (j) the tip showing the SL layers and substrate which will be ready for APT analysis after the removal of Pt protective layer

Atom probe data were obtained in the pulsed-green laser mode at a laser pulse rate of 400 kHz, an ion detection rate of 0.5% (as described in eq 4.5), and with the specimen holder cooled to 54 K. The laser pulse energy was 8 pJ for the thick-motif SL specimen, and 13 pJ for the thin-motif specimen for which results are presented below. Field evaporation commenced at a direct current (DC) voltage of ~ 2600 V for both of these specimens. The voltage increased to ~ 3200 V

before each of the specimens fractured. CAMECA's IVAS ™ [17] software suite was used to produce and to interrogate the reconstructions. Data were obtained from the bottom 1.5 bilayers and the substrate of the thick-motif SL, and ~ 70 repetitions of the thin-motif SL. Because a voltage drop was associated with crossing the interface between the (InAl)As/(InGa)As SL and the InP substrate, shank-angle evolution was used to calibrate the reconstructions. The initial specimen tip radii and shank angles were determined from secondary-electron SEM images of the specimens, prior to running them in the atom probe. The resolution of the APT data in the growth direction is expected to be better than that in the lateral direction [18]. The resolution in the growth direction could approach 0.2 nm in this analysis. The motif thicknesses in the reconstruction were within 10% of the periodicity deduced from the HRXRD diffraction pattern of each sample. Thus, the atom probe data might underestimate the diffusion distance that is determined below by at most 10%. The atom number density obtained in the reconstruction matched that determined for unstrained materials, assuming that Vegard's law holds, to within 15%. These comparisons were used to validate the reconstruction parameters. Atom probe data were obtained from interior sections of the thin-motif SL only, but shank-angle evolution was nevertheless employed for consistency.

It is also critical to ascertain if there is a dependence of the observed intermixing on the layer thicknesses and target compositions, more so in the 1-4 nm range for mid-IR QCLs [8]. A specific SL growth was performed by MOCVD at a reactor pressure of 100 Torr and at a temperature of 605 °C, with a wafer rotation of 100 rpm, to study this effect. The schematic for the target structure is shown in figure 4.5.

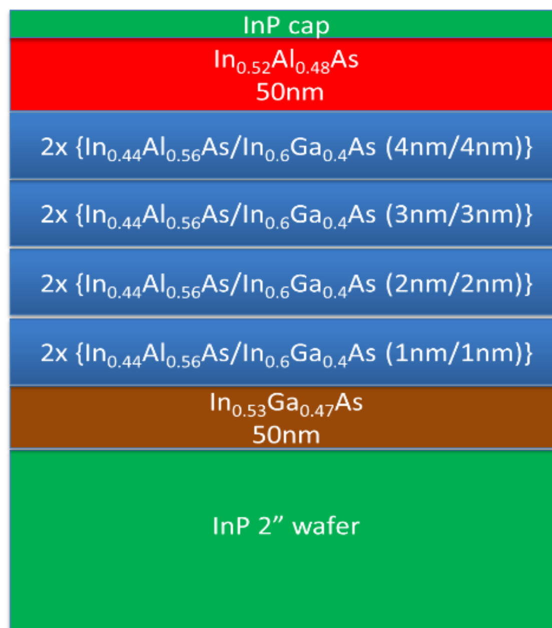

Figure 4.5 SL schematic to study the interfacial intermixing dependence on layer thicknesses.

Tip specimens were prepared from this sample using lift out and shaping techniques as enlisted earlier. APT experiments were conducted in collaboration with Dieter Ishiem at Northwestern university center of atom probe tomography (NUCAPT) using the CAMECA 5000X Si™ [19] instrument. FIB techniques were used to prepare slices for HRTEM analysis.

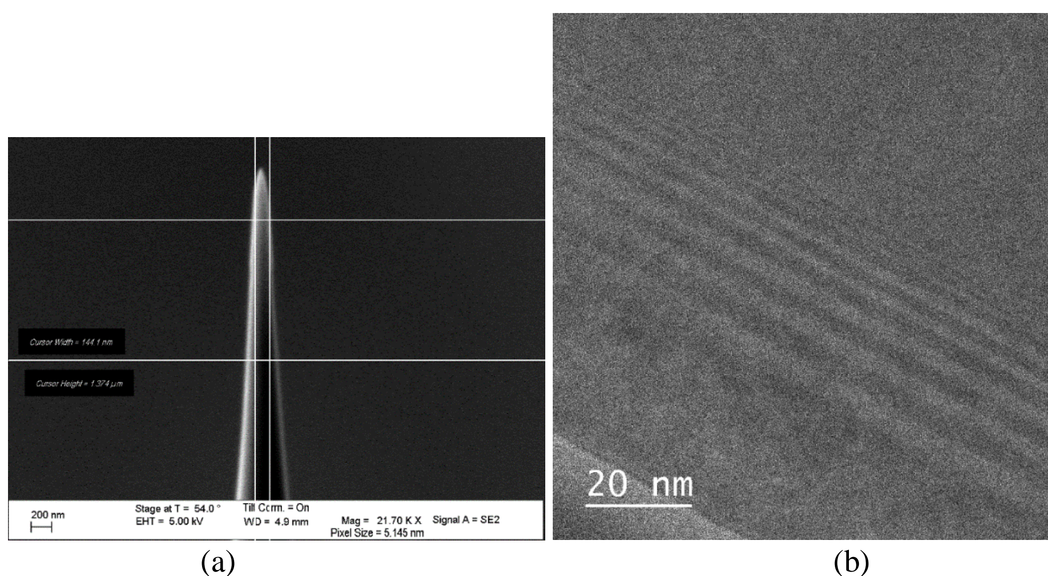

(a) (b)

Figure 4.6 (a) SEM image of the final tip shape before evaporation (b) HRTEM image

Atom probe data were obtained in the pulsed-UV laser mode at a laser pulse rate of 250 kHz, an ion detection rate of 1%, and with the specimen holder cooled to 30 K. The laser pulse energy was 0.88 pJ for the specimen. Field evaporation commenced at a direct current (DC) voltage of ~ 2300 V and increased to ~ 4500 V before the run ended. An SEM image of the final tip used for APT as well as atomic resolution HRTEM image were used to validate the tip shape and layer thicknesses respectively in the reconstruction (figure 4.6).

4.4 Reconstruction and Analysis

Figure 4.7 presents the HRXRD pattern measured from the thick-motif SL and two simulated patterns. The experimental pattern shows the sharp oscillations indicative of a highly periodic structure in the [001] (growth) direction, implying that the composition profile is repeated exactly in each bilayer motif. The shoulder at the lower side of the central InP substrate peak is due to an average residual, 0.093% compressive strain in the superlattice, which is not seen in the simulation for the targeted strain compensated superlattice. The simulations indicate a total motif thickness of 43.5 nm.

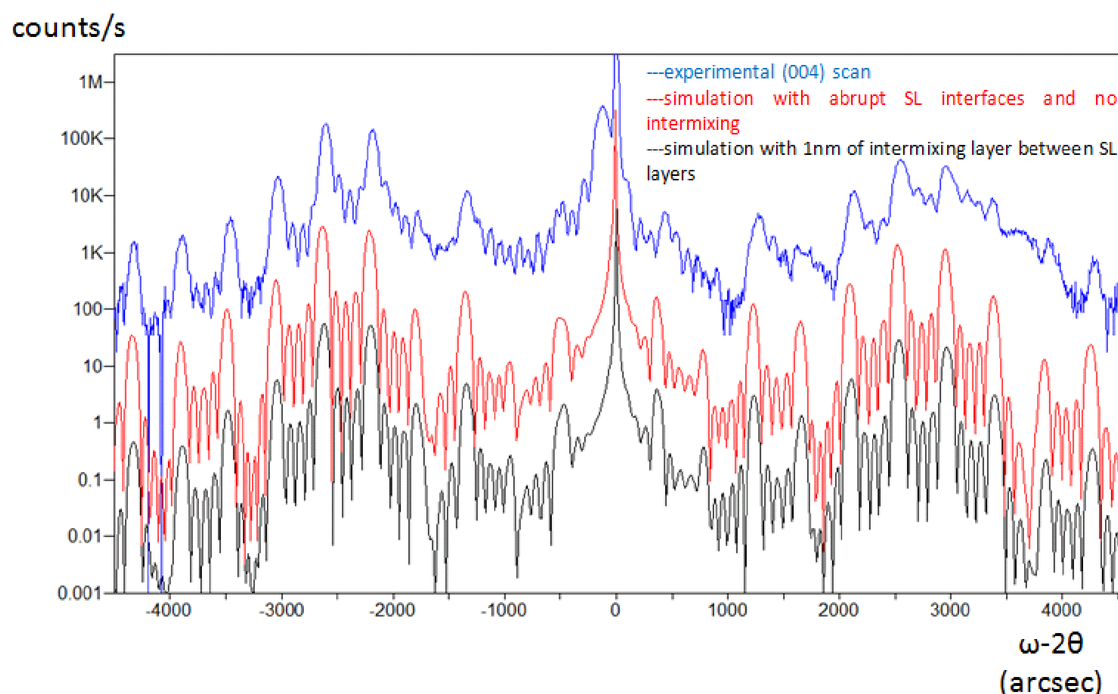

Figure 4.7 High-resolution X-ray diffraction (HRXRD) (004) ω-2θ scan for the thick-motif SL with simulations: (red) abrupt SL interfaces and (black) SL with a 1 nm thick constant composition intermixing layer. All scans are offset vertically for clarity

For the computed X-ray diffraction patterns shown in figure 4.7, both assume the same total thickness of the superlattice motif and the same average composition within the motif. The simulations differ in how the component elements are distributed within the motif. The red curve simulates the diffraction pattern from a superlattice motif, with step function changes in concentrations of the component elements at discrete interfaces between the sublayer, each of which has a uniform but different chemical composition. The black curve simulates the interfaces (simulation 2) as additional layers of thickness 1 nm with an intermediate composition, $In_{0.52}Al_{0.315}Ga_{0.165}As$, and keeps the periodicity of the motif constant. The figure demonstrates that the distance over which the composition change occurs, and therefore the interface thickness, cannot be deduced from the XRD data, due to the subtlety of the changes that the different composition profiles induce in the simulated pattern. However, the thickness of the bilayer motif

and its average composition can be determined from the HRXRD pattern and has served as inputs into the calibration of the atom probe data reconstruction.

The atom maps constructed from the atom probe data are shown in figure 4.8. The layer composition deduced by fixing the As concentration at 50 at.%, are $In_{0.39}Al_{0.61}As/In_{0.69}Ga_{0.31}As$, which are close to the values obtained from HRXRD (table 4.3). Confidence in the magnification calibration of the atom probe reconstruction in the growth direction, that is, perpendicular to the interfaces, was of particular importance. The reconstruction parameters were tuned such that the layers in the reconstruction were planar and the period of the SL was within 10% deviation from the value deduced by HRXRD. A ±1% uncertainty was observed in the HRXRD fit for this SL.

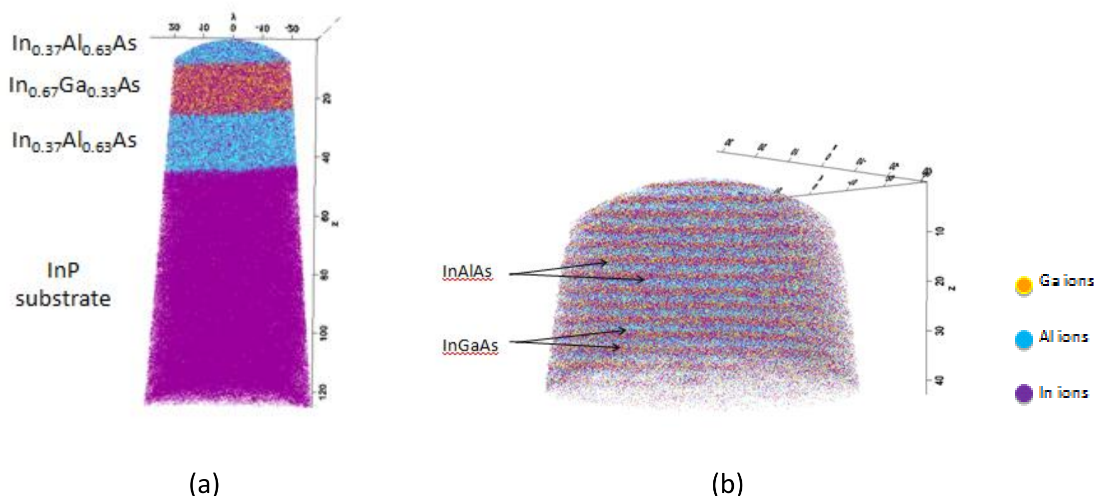

Figure 4.8 Atom maps for the obtained atom probe tomography (APT) for (a) thick-motif SL (b) thin-motif SL.

	HRXRD Composition; Period	**APT Composition; Period**
Thick-motif SL	$In_{0.37}Al_{0.63}As/In_{0.67}Ga_{0.33}As$; 43.5 nm	$In_{0.38}Al_{0.62}As/In_{0.69}Ga_{0.31}As$; 38.6 nm
Thin-motif SL	$In_{0.44}Al_{0.56}As/In_{0.60}Ga_{0.40}As$; 4.1 nm	$In_{0.46}Al_{0.50}Ga_{0.04}As/In_{0.58}Ga_{0.31}Al_{0.11}As$; 3.7 nm

Table 4.3 SL layer compositions and SL periods determined from HRXRD simulations and APT reconstructions

Concentration profiles along the growth direction and perpendicular to the interfaces were deduced from the atom probe reconstructions, in order to measure the compositional width of the

interfaces. A cylindrical volume-shaped subset of the reconstruction (a “region of interest”) centered approximately along the long axis of the specimen was extracted for this analysis, in order to exclude possible surface-related artifacts and distortions. An iso-concentration surface located approximately at one of the interfaces was chosen as the zero for these profiles. The compositions of sequential 0.2 nm thick discs of radius 9 nm lying parallel to the iso-concentration surface were determined from the reconstruction to generate the concentration profile (a “proxigram”). Extracting the concentration profile in this way should minimize any artificial broadening of the interface due to steps or other local morphological features with sizes greater than 0.5 nm. Growth steps up to 0.5 nm (or equivalently one unit cell) would be averaged in this method.

Figure 4.9 (a) shows proxigrams for the relative concentrations of the group III elements for the thick-motif SL. The III:V ratios deduced from the atom probe data were of the order (53:47), rather than 1:1. This deviation from the known stoichiometry of III-V compounds is commonly observed in atom probe reconstructions of arsenides and phosphides and is believed to arise from the propensity for As and P to field evaporate as polyatomic ions [1]. Because compound semiconductors are essentially line compounds with a III:V ratio of 1:1, the As concentration was assumed to be equal to 50 at.% throughout both superlattices, and the sum of the group III concentrations was set to 100%, to be consistent with the chemical formula as typically written, throughout the profiles shown in figures 4.9 and 4.10.

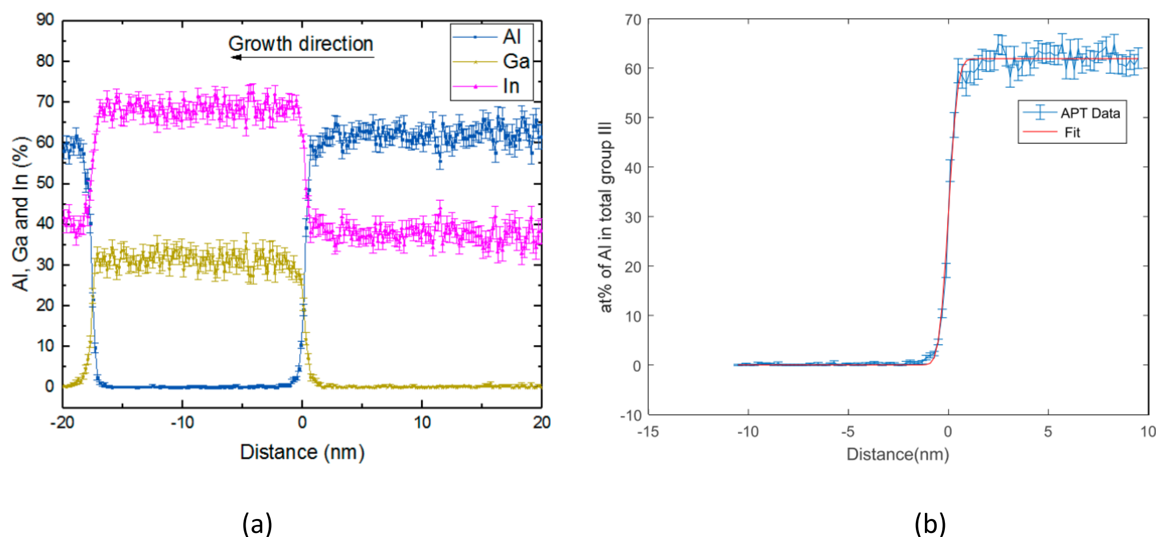

Figure 4.9 (a) Proxigram concentration profiles for the group III elements perpendicular to the interface in the thick-motif SL. Error bars represent counting-based statistical precision of the atom probe data; (b) Measured Al concentration profile, together with a best-fit semi-infinite solid solution to Fick's second law of diffusion applied to the InGaAs–InAlAs interface.

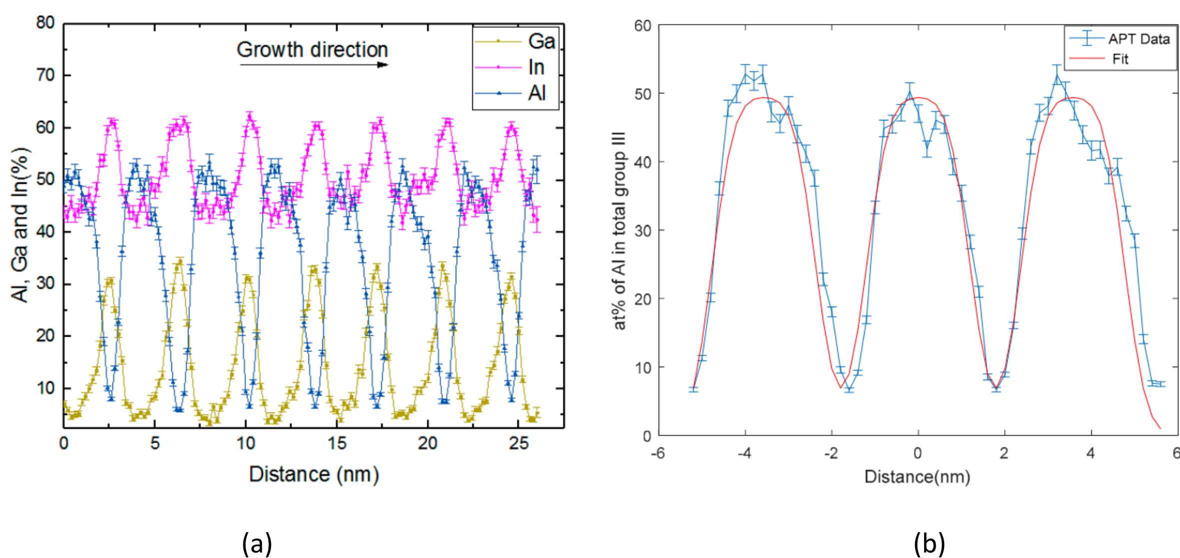

Figure 4.10 (a): Proxigram for thin-motif SL showing only group III concentrations. (b) Diffusion length estimation by fitting Fick's law of diffusion to the Al content profile

4.4.1 Extent of Intermixing in the Thick-motif sample

To assess the extent of intermixing at the interfaces between component materials, and to extract a measure of the compositional width of the interfaces, solutions to Fick's second law were fit to the measured concentration profiles. For both the thick-motif and the thin-motif SLs, the

interdiffusion coefficient, D, was assumed to be independent of composition. In the case of the thick-motif sample, mass spectra corresponding to the central volume of the (InAl)As showed no peaks corresponding to Ga; in parallel, mass spectra from the central volume of the InGaAs layers showed no intensity at the Al ion positions. Therefore, the one-dimensional solution to Fick's second law for a diffusion couple composed of two semi-infinite solids was fit to the Al concentration profile to extract a diffusion distance, the diffusivity, and a measure of the interface thickness. Specifically, the profile data $C_{Al}(x)$ were fit to the following function [20]:

$$C(x,t) = \frac{1}{2}\, C_0\, erfc\, \frac{x}{2\sqrt{Dt}} \qquad 4.1$$

where C_0 is the initial concentration of the diffusing species in one solid, Al in the InAlAs barriers, D is the interdiffusion coefficient at 605 °C (and the fitting parameter), and t is the time at that temperature.

For the semi-infinite solution to Fick's second law, $x = 2\sqrt{Dt}$, often referred to as the "diffusion distance", is the distance from the yet-to-diffuse step-function interface to the plane at which the concentration of Al in the nominal (InGa)As layer is 8% of the concentration of Al in $In_{0.38}Al_{0.62}As$, specifically 5 at. % of the atoms on the Group III site.

The fit obtained at the InGaAs–InAlAs interface is shown in figure 4.9 (b), and it yielded a diffusion length of 0.51 ± 0.02 nm at the 95% confidence interval. Noting that this interface is close to the substrate, therefore equating the time at the temperature to the approximate length of the growth run, t = 1900 s, an interdiffusion coefficient of $D = 4.1 \times 10^{-23} m^2 s^{-1}$ at 605 °C is estimated. Diffusion lengths considering Al and Ga concentration profiles and looking at both interfaces probed, were deduced by the same fitting technique, as summarized in table 4.4

Interface	Diffusion Length (nm) for Al	Diffusion Length (nm) for Ga
InAlAs–InGaAs	0.52 ± 0.02	0.54 ± 0.04
InGaAs–InAlAs	0.51 ± 0.02	0.58 ± 0.03

Table 4.4 Diffusion lengths obtained by fitting Fick's second law to Al and Ga concentration profiles in the thick-motif sample (table 4.3), not accounting for the 10% discrepancy between HRXRD and APT SL period measurements

4.4.2 Extent of Intermixing in the Thin-motif sample

The individual layers in the thin-motif SL are about one-tenth the thicknesses of those in the thick-motif SL, and more importantly, closer to the typical thicknesses of the layers that comprise QCL designs. Figure 4.10 presents proxigram concentration profiles for the group III elements obtained from this sample. The concentration profiles immediately suggest that there is intermixing throughout the SL structure to produce quaternary alloy layers with compositions that vary continuously in the growth direction. None of the component layers appeared to be ternary, as they were intended to be.

Specifically, the concentration profiles suggest that the (InGa)As wells contained a minimum of 11 at. % Al on the group III site, and the (InAl)As barriers contain at least 4 at. % Ga on the group III site. The presence of the fourth element in the intended ternary layers of the SL was confirmed by examining the mass spectrum from a thin slice of "material" from the center of the ternary layers and finding significant peaks from the fourth element. Pantzas et al. have reported similar concentration profiles for a QCL that is lattice-matched to InP, based on the high-angle annular dark-field scanning transmission electron microscopy (HAADF-STEM) image [21]. The semi-infinite solution to Fick's second law used above does not apply to the thin-motif SL profile because the adjacent diffusion fields overlap. To model the intermixing as a result of diffusional processes in this SL, a solution to Fick's second law that describes one-dimensional

diffusion of a component from an initial slab of material of fixed width, $2h$, and uniform concentration, C_0 was used, specifically [20]:

$$C = \frac{1}{2} C_0 \left\{ erf \frac{h - x}{2\sqrt{Dt}} + erf \frac{h + x}{2\sqrt{Dt}} \right\} \qquad 4.2$$

The concentrations at positions x, which would result from the summed diffusion from series of three such slabs of initial composition $In_{0.505}Al_{0.495}As$ and thickness 2.4 nm spaced on 3.7 nm centers were fit to the Al concentration profile, and they are shown in figure 4.10 (b). The SL period in the APT observed in the HRXRD fit for this SL reconstruction is ~ 10% smaller than that deduced from the HRXRD, given that a ±2.5% uncertainty is observed in the HRXRD fit for this SL.

The resulting $2\sqrt{Dt}$ diffusion distance was 0.56 ± 0.01 nm for the best fit at the 95% confidence interval. Assuming that the profile was obtained from approximately the middle of the SL—and it is only known that it was not from the bottom—a time at a temperature of 2800 s (half the total growth time) was applied, yielding an interdiffusion coefficient of 3.4×10^{-23} m^2s^{-1}. This was calculated accounting for the 10% thicker SL period (as observed by HRXRD) and is in good agreement with that deduced for the thick-motif sample.

The observed compositional grading at the interface could either result from; (a) surface segregation at the growth front during the layer growth or growth pause between SL layers [22], [23], and/or (b) solid-state diffusion during the growth of subsequent layers, due to continued annealing as the structure is grown. Based on the growth rates in table 4.2, the growth of 40 stages within a typical QCL active region takes ~ 6.42 hr (including the 5s pause time in between each layer) [24]. Using the diffusivity determined for the thin-motif SL results in a $2\sqrt{Dt}$ diffusion distance of 1.8 nm for the first layer within the first stage of the active region, while the first layer in the 40th stage would exhibit a $2\sqrt{Dt}$ diffusion distance of 0.3 nm if diffusion were responsible

for the intermixing. This rather large discrepancy in interfacial grading between the first and the last stage of a QCL would be expected to have a significant impact on device performance since the QCL designs are quite sensitive to SL layer thickness and composition.

However, according to the estimated diffusivity versus temperature profile for an InGaAs/InAlAs heterostructure grown by MBE and having undergone lamp annealing [25], *D* is projected to be in the 10^{-22} m^2s^{-1} range, which in turn indicates that solid state diffusion cannot be ruled out as a possible mechanism for observed composition profiles. From HRTEM analysis on similar QCL structures, the differences in layer thicknesses from the first to the last stage are seen to be within the measurement error. Additional APT experiments are required to analyze the interfaces in the first and the last stages of a QCL, to ascertain which mechanism or combination of mechanisms result in the observed composition gradients. Figure 4.10 suggests some degree of asymmetry in the interfacial composition profile, which is not accounted for in the fitting. The veracity of the asymmetry could be tested by running the atom probe experiments from the substrate down, in the opposite direction to that used in this study, but such experiments have not yet been achieved. Asymmetric graded interfaces (2.5–4.5 nm in width) have also been observed for lattice-matched InAlAs/InGaAs SL structures grown by MOCVD [9], and for InGaAsP multiple quantum well (MQW) structures where Ga and As are diffused asymmetrically into the lower and upper InP buffer layers [26], as well as for InGaN/GaN quantum wells where the upper InGaN/GaN interface is found to be 1.3 nm wide and the lower interface is 0.6 nm wide, in that study [11]. Lattice-matched InAlAs/InGaAs QCL active regions grown by molecular beam epitaxy (MBE) also exhibit four monolayers of compositional grading in the interfaces [22]. Indium segregation was not indicated at any interfaces in either of the SLs studied here, unlike what was reported in Ref [9].

4.4.3 Layer thickness dependent interfacial intermixing

For the SL analyzed at Northwestern University (figure 4.5), a 7° half shank angle was measured from figure 4.6 (a) for reconstructing the atom probe tip, as seen before evaporation.

Target composition	Target Thickness (nm)	Actual thickness (nm)
$In_{0.6}Ga_{0.4}As$	4	-
$In_{0.44}Al_{0.56}As$	4	4.3
$In_{0.6}Ga_{0.4}As$	4	4
$In_{0.44}Al_{0.56}As$	4	3.7
$In_{0.6}Ga_{0.4}As$	3	3.3
$In_{0.44}Al_{0.56}As$	3	3.3
$In_{0.6}Ga_{0.4}As$	3	3.1
$In_{0.44}Al_{0.56}As$	3	3.3
$In_{0.6}Ga_{0.4}As$	2	2
$In_{0.44}Al_{0.56}As$	2	2
$In_{0.6}Ga_{0.4}As$	2	2.4
$In_{0.44}Al_{0.56}As$	2	2.1
$In_{0.6}Ga_{0.4}As$	1	-
$In_{0.44}Al_{0.56}As$	1	-
$In_{0.6}Ga_{0.4}As$	1	-
$In_{0.44}Al_{0.56}As$	1	-

Table 4.5 Actual vs target thicknesses for the SL schematic in figure 4.5

The measured thicknesses from HRTEM for some of the constituent layers are compared with target thicknesses in table 4.5. The thicknesses of the 1 nm thick layers could not be accurately

determined from the HRTEM image. The actual thicknesses for the layers have not yet been incorporated in the tip reconstruction.

The reconstructed tip (figure 4.11) has some of the top 50 nm lattice-matched InAlAs layer, entire thin multilayer structure, and the entire bottom 50 nm lattice-matched InGaAs layer going into the InP substrate. By extracting a cylinder of diameter 5 nm from the central region of the reconstructed tip, and aligning it perpendicular to the SL layers, a 1D composition profile can be obtained with the thinnest layers being resolved as shown in figure 4.12 (a). This profile is obtained considering by looking at only the group III elements in the mass spectrum to remove any uncertainties in the layer compositions that could be brought about by the tendency of As to evaporate as molecular ions up to As_5^+. It is evident that there is a significant reduction in the Al content of the InAlAs layers from the target composition when they are 1 nm thick. It is also seen that the Al content in the target 1 nm thick layers is up to 20% less than that seen in the target 4 nm thick layers. The target 4 nm thick layers are close to the target composition within 2% Al content for barriers and within 4% In for the wells. The target 2 nm thick layers are on average 6-8 % Al deficient with respect to the target composition. It is important to note that the 1 nm thick layers, closer to the substrate, are annealed in the reactor for a longer time than the 4 nm layers.

Scanning transmission electron microscopy x-ray dispersive spectroscopy (STEM-EDX) was also performed. Ga and In L-lines and Al K-line were measured. From the 1D composition profile in figure 4.12 (b) obtained by this technique, the individual layers can be distinguished up to 1 nm thickness, but enough resolution isn't seen to extract interfacial grading information as can be done through APT.

Overshooting of Al content in the barriers is a well-known technique to get around the Al deficiency seen due to intermixing at interfaces [21]. Similarly, for a tapered active QCL structure

[27], the Al content in the 11 Å thin barriers was overshot by 5% to find that the observed emission wavelength reduces from 4.8 µm to match the designed target wavelength of 4.6 µm. The obtained 1-D composition profile from the APT reconstruction data provides direct input for the extent of overshooting of Al required in the 1 and 2 nm thick barriers, for these compositions and strains (figure 4.5). Efforts are underway to incorporate this result into the QCL design and overshoot the TMAl flow accordingly during the growth of the thinnest InAlAs barriers in the active region.

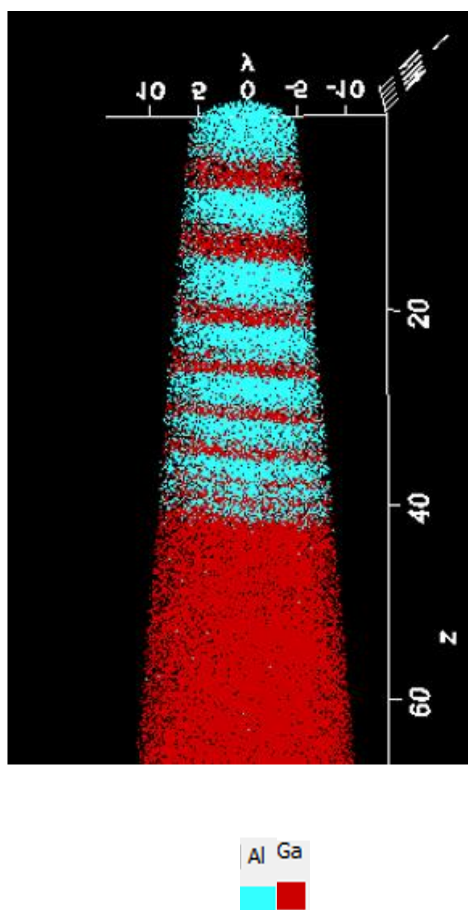

Figure 4.11 Reconstructed APT tip to study the layer thickness dependent interfacial intermixing. Only 50% of the Al and Ga atoms are shown.

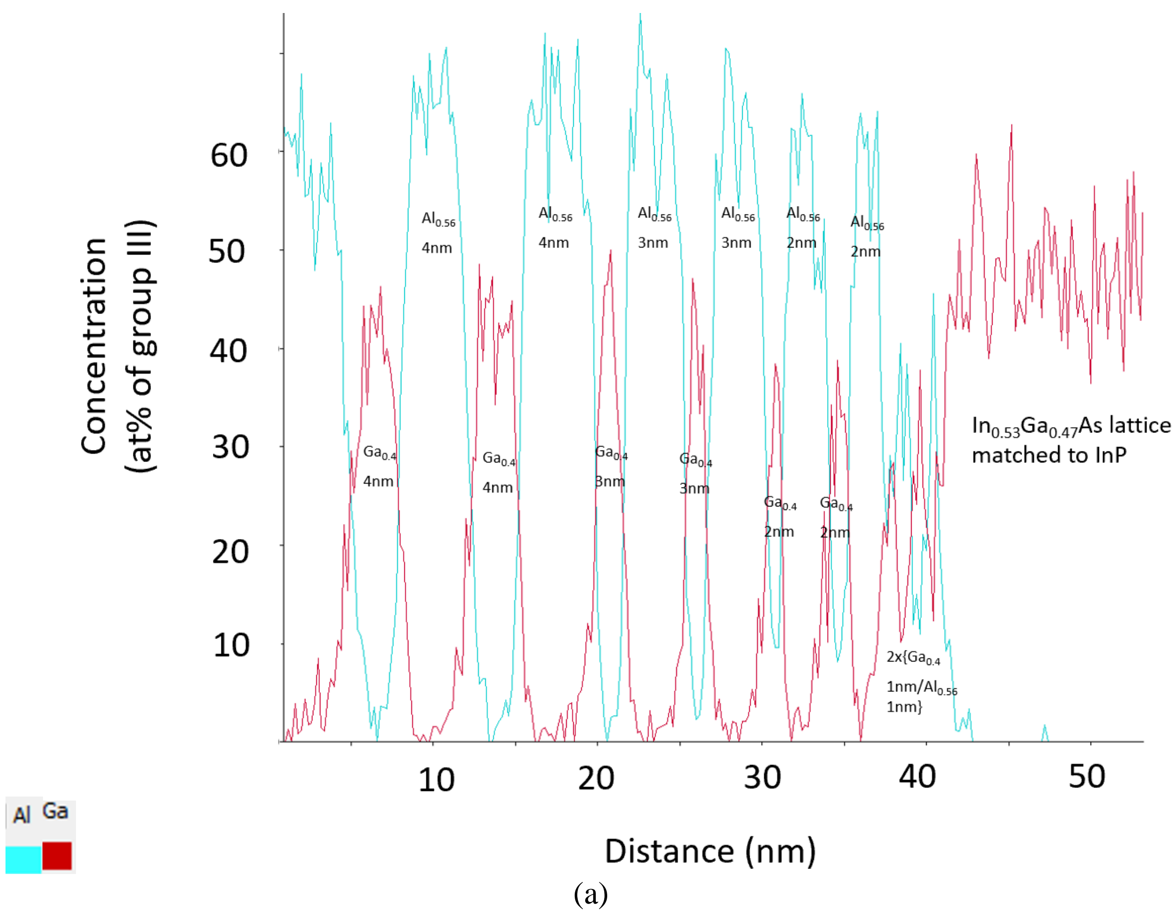

(a)

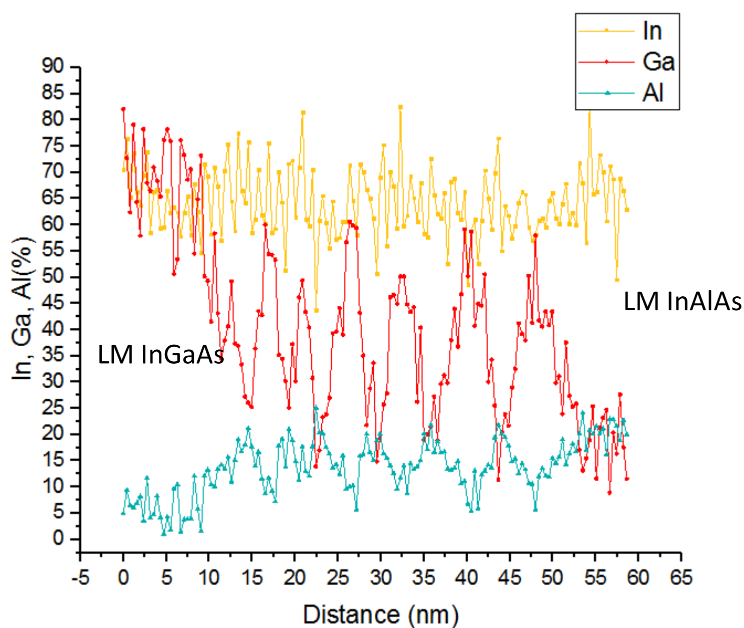

(b)

Figure 4.12 Layer thickness dependent 1-D composition profile from (a) a central ROI within the reconstructed tip, looking at only Al and Ga profiles (b) STEM-EDX

4.4.4 Lateral Interface Roughness

1-D composition profiles can be computed by selecting an iso-concentration surface in the APT reconstructed tips. Similarly, in-plane roughness can be calculated for the same iso-concentration surfaces. As an example, for the SL with thin layer motif, 11% Ga isoconcentration surfaces were created that resulted in peak-to-valley roughness values of 0.7-0.9 nm and RMS roughness values of 0.1-0.2 nm.

Wang et al. reported growth optimization with respect to V/III ratio, growth rates and strain balancing by atomic force microscopy (AFM) and XRD measurements [28]. AFM measurements are conducted using a Bruker Multimode™ 8 [29] instrument in tapping mode. The cantilever has a spring constant of 40 N/m and is made of n-type Si with 8 nm tip radius. Initial experiments consisted of analyzing 0.5 µm thick bulk layers of InGaAs and InAlAs nominally lattice-matched to an (001) InP substrate. All samples have a final coating of 10 nm thick InP. The flattening procedure employs a polynomial of the specified order on the AFM data (line by line) to find the least-squares fit which is then subtracted from the scanned line, in order to reduce the effect of bowing and tilt. 2nd order flattening is applied to all AFM scans (5×5 μm^2).

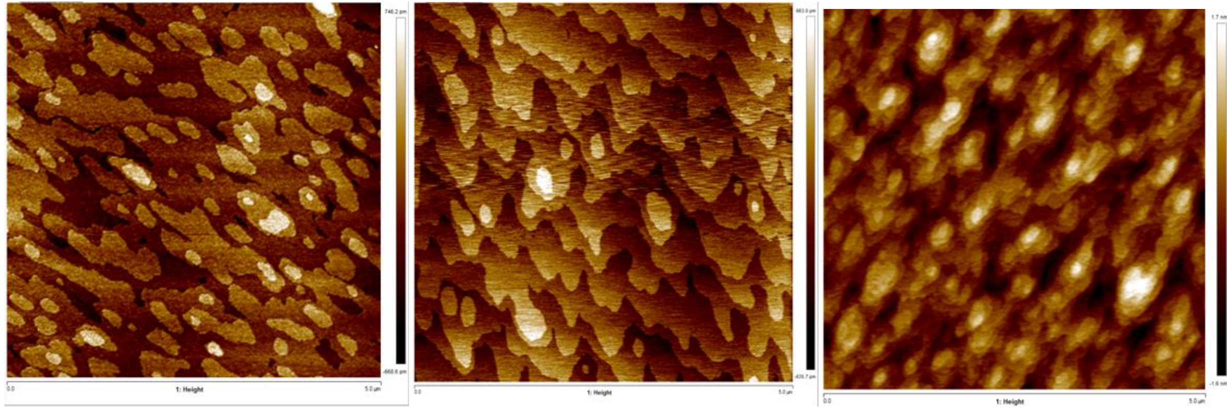

(a) (b) (c)

Figure 4.13: a) InGaAs, growth rate= 0.09 nm/s, *T*= 605 °C, V/III= 495, RMS roughness= 0.199 nm b) InGaAs, growth rate= 0.09 nm/s, *T*= 605 °C, V/III= 496, RMS roughness =0.191 nm c) InAlAs, growth rate= 0.13 nm/s, *T*= 605 °C, V/III= 340, RMS roughness= 0.453 nm

For bulk layers, the InAlAs surface is more than two times rougher than the InGaAs surface. Similarly, we intend to analyze surface morphologies with AFM for SL samples ending at InGaAs layer and InAlAs layer, along with samples of various strain balancing conditions in order to reveal the current growth mode for QCLs. Subsequently, the growth mode will be optimized to move from islanding or mixed islanding and step mode to pure step mode growth. It has been reported that growths interfaces are more smooth on exact (100) substrates when compared to those on 2° miscut substrates, which is supported by AFM data along with device performance [30].

The experimentally obtained values for in-depth roughness height and in-plane roughness height are important for calculating the interface roughness induced broadening of electroluminescence spectra of QCL devices [31].

4.5 Conclusions

$In_xAl_{1-x}As/In_yGa_{1-y}As$ SL structures with different compositions, layer thicknesses, and strains, grown on InP substrates were analyzed by APT. Fitting the compositional profile to solutions to

Fick's second law of diffusion provided an estimate for the interdiffusion length in the range of 0.54–0.56 nm. The interdiffusion coefficient for both structures with constant SL motif is in the range of 3–4 $\times 10^{-23}$ m^2 s^{-1}, which is within acceptable agreement with that reported for similar materials. A discussion is presented for the possible causes of the observed intermixing, which can be due to surface segregation or bulk phase diffusion, or a combination. When the SL layers' thicknesses are on the order of a typical QCL structure, the intended ternary layers are found to be quaternary alloys. InAlAs barriers are found to be significantly Al deficient when the target thicknesses are 1 nm. Lateral roughness of the interfaces, both in-plane and in-depth, can be calculated through iso-concentration surfaces in APT reconstructions and AFM measurements.

Future work will include APT of the full QCL structure in order to ascertain if annealing is the cause of observed interfacial diffusion profiles. This will be accomplished by comparing the layer thicknesses and compositions in the stages grown initially, in the middle and towards the end of the active region regrowth. The implementation of designs for the same accounting for the interface grading, and study of the effects of growth parameters on the intermixing is underway.

References

[1] Baptiste Gault; Michael P. Moody; Julie M. Cairney; Simon P. Ringer, *Atom Probe Microscopy*. Springer Science+Business Media, LLC 2012, 2012.

[2] T. T. Tsong, "Photon stimulated field ionization," *J. Chem. Phys.*, vol. 65, no. 6, pp. 2469–2470, 1976.

[3] B. Viswanathan, W. Drachsel, J. H. Block, and T. T. Tsong, "Photon enhanced field ionization on semiconductor surfaces," *J. Chem. Phys.*, vol. 70, no. 5, pp. 2582–2583, 1979.

[4] G. L. Kellogg and T. T. Tsong, "Pulsed-laser atom-probe field-ion microscopy," *J. Appl. Phys.*, vol. 51, no. 2, pp. 1184–1193, 1980.

[5] A. Cerezo, G. D. W. Smith, and P. H. Clifton, "Measurement of temperature rises in the femtosecond laser pulsed three-dimensional atom probe," *Appl. Phys. Lett.*, vol. 88, no. 154103, pp. 1–3, 2006.

[6] B. Gault *et al.*, "Design of a femtosecond laser assisted tomographic atom probe," *Rev. Sci. Instrum.*, vol. 77, no. 043705, pp. 1–8, 2006.

[7] T. F. Kelly and D. J. Larson, “Local electrode atom probes,” *Mater. Charact.*, vol. 44, pp. 59–85, 2000.

[8] D. Botez *et al.*, “High internal differential efficiency mid-infrared quantum cascade lasers,” *Proc. SPIE*, vol. 10123, p. 101230Q1-12, 2017.

[9] C. A. Wang *et al.*, “Sensitivity of heterointerfaces on emission wavelength of quantum cascade lasers,” *J. Cryst. Growth*, vol. 464, pp. 215–220, 2017.

[10] A. Rajeev *et al.*, “Regrowth of quantum cascade laser active regions on metamorphic buffer layers,” *J. Cryst. Growth*, vol. 452, pp. 268–271, 2016.

[11] F. Liu *et al.*, “Composition and interface analysis of InGaN/GaN multiquantum-wells on GaN substrates using atom probe tomography,” *J. Vac. Sci. Technol. B,Nanotechnology Microelectron. Mater. Process. Meas. Phenom.*, vol. 32, no. 5, pp. 0512091-7, 2014.

[12] E. W. Müller, “Field desorption,” *Phys. Rev.*, vol. 102, no. 3, pp. 618–624, 1956.

[13] R. Gomer, “Field Desorption,” *J. Chem. Phys.*, vol. 31, no. 2, pp. 341–345, 1959.

[14] T. T. Tsong, “Field Ion Image Formation,” *Surf. Sci.*, vol. 70, no. 1, pp. 211–233, 1978.

[15] A. Rajeev *et al.*, “Interfacial Mixing Analysis for Strained Layer Superlattices by Atom Probe Tomography,” *Crystals*, vol. 8, no. 437, pp. 1–9, 2018.

[16] “https://www.malvernpanalytical.com/en/products/product-range/xpert3-range/xpert3-mrd.” .

[17] “CAMECA.” [Online]. Available: http://www.cameca.com/service/software/ivas.

[18] F. Vurpillot, G. Da Costa, A. Menand, and D. Blavette, “Structural analyses in three-dimensional atom probe: A Fourier transform approach,” *J. Microsc.*, vol. 203, no. 3, pp. 295–302, 2001.

[19] “https://www.cameca.com/products/apt/leap-5000.” .

[20] J. Crank, *The mathematics of diffusion*, 2nd ed. Bristol: Oxford University Press, Ely House, London, 1975.

[21] K. Pantzas *et al.*, “Sub-nanometrically resolved chemical mappings of quantum-cascade laser active regions,” *Semicond. Sci. Technol.*, vol. 31, no. 055017, pp. 1–7, 2016.

[22] P. Offermans, P. M. Koenraad, J. H. Wolter, M. Beck, T. Aellen, and J. Faist, “Digital alloy interface grading of an InAlAs/InGaAs quantum cascade laser structure studied by cross-sectional scanning tunneling microscopy,” *Appl. Phys. Lett.*, vol. 83, no. 20, pp. 4131–4133, 2003.

[23] A. A. Marmalyuk *et al.*, “Investigation of indium segregation in InGaAs /(Al) GaAs quantum wells grown by MOCVD,” vol. 237–239, no. Part 1, pp. 264–268, 2002.

[24] D. Botez *et al.*, “High-efficiency, high-power mid-infrared quantum cascade lasers,” *Opt.*

Mater. Express, vol. 8, no. 5, pp. 1378–1398, 2018.

[25] K. S. Seo, P. K. Bhattacharya, G. P. Kothiyal, and S. Hong, "Interdiffusion and wavelength modification in In0.53Ga0.47As/ In0.52Al0.48As quantum wells by lamp annealing," *Appl. Phys. Lett.*, vol. 49, no. 15, pp. 966–968, 1986.

[26] L. Megalini *et al.*, "1550-nm InGaAsP multi-quantum-well structures selectively grown on v-groove-patterned SOI substrates," *Appl. Phys. Lett.*, vol. 111, no. 032105, 2017.

[27] D. Botez, C. C. Chang, and L. J. Mawst, "Temperature sensitivity of the electro-optical characteristics for mid-infrared (λ = 3-16 μm)-emitting quantum cascade lasers," *J. Phys. D. Appl. Phys.*, vol. 49, no. 043001, pp. 1–33, 2016.

[28] C. A. Wang *et al.*, "OMVPE growth of highly strain-balanced GaInAs/AlInAs/InP for quantum cascade lasers," *J. Cryst. Growth*, vol. 310, no. 23, pp. 5191–5197, 2008.

[29] "https://www.bruker.com/products/surface-and-dimensional-analysis/atomic-force-microscopes/multimode-8-hr/overview.html." .

[30] A. Bhattacharya, L. J. Mawst, S. Nayak, J. Li, and T. F. Kuech, "Interface structures of InGaAs/InGaAsP/InGaP quantum well laser diodes grown by metalorganic chemical vapor deposition on GaAs substrates," *Appl. Phys. Lett.*, vol. 68, no. 16, pp. 2240–2242, 1996.

[31] A. Rajeev, C. Sigler, T. Earles, Y. V Flores, L. J. Mawst, and D. Botez, "Design considerations for λ ~ 3.0-to 3.5-μm-emitting quantum cascade lasers on metamorphic buffer layers," *Opt. Eng.*, vol. 57, no. 1, p. 011017(1-10), 2017.

Chapter 5 Concluding Remarks

5.1 Summary

A mid-IR QCL with an emission wavelength of 3.4 μm has been designed for a virtual substrate of the composition $In_{0.22}Ga_{0.78}As$ [1]. This design has the advantage of depopulation of the lower laser level involving both the SPR scheme and resonant-tunneling extraction to the extractor/injector region. In turn, one obtains fast, miniband-like carrier extraction from the active region. InAlAs is computationally shown to be more effective than InGaP in confining the optical field as well as better for dissipating the generated heat. There is, however, a penalty in the heat dissipation of such a QCL owing to the requirement of a ternary cladding layer lattice-matched to the MBL when compared to the InP-based QCLs employing InP claddings.

An HVPE-grown MBL was used to access a substrate lattice parameter which could not be obtained by the use of a conventional binary semiconductor substrate. This change in lattice parameter allows for the use of barrier and well compositions which would be otherwise prohibited due to excessive strain if grown on a conventional substrate, thus enables the development of a short-emission-wavelength QCL of potentially significantly improved performance [2], [3]. CMP and wet-chemical etching are found to be effective in preparing the MBL surface for growth of the QCL structure. Successful MOCVD growth of ten stages of a QCL active region (with and without cladding layers) on such a surface has been achieved with high structural fidelity. Moreover, the growth of thirty stages of the same active region along with the cladding and confinement layers necessary for fabricating a laser device has been demonstrated successfully as evidenced by HRXRD data.

A typical QCL consists of layers on the order of 1nm or less which makes it critical to have a step flow growth mode and consequently obtain monolayer control on the interfaces. Through

atom by atom evaporation, APT reveals the interface characteristics on SLs grown by MOCVD. XRD is useful to gauge the SL periodicity and the average composition. TEM is employed to look at 2-D projections of the thin slices of the SL in order to verify the individual layer thicknesses and overall SL quality. These characteristics correlate to the growth conditions and the SL design, which are then optimized to obtain abrupt compositional interfaces. The k.p modeling used to design QCLs for specific emission wavelengths and optimize the key parameters, assumes abrupt interfaces. Strong deviation observed in composition with respect to the target compositions in III-V strained SL layers with thicknesses ~1nm will affect the thinnest barriers in the QCL design. It was shown that intended ternary layers with thicknesses 1-2 nm exist as quaternary alloys due to interfacial composition grading. Intermixing such that all layers are quaternary can alter the design completely. Small changes (~1 Å) in the active region distort the intended electron wavefunctions and offset the emission wavelength. It has been observed that overshooting Al content by 5% in the 11 Å thick InAlAs barriers provided a good correlation between the target and obtained wavelength emission from a tapered active QCL [4].

5.2 Future Work

This work will take the following paths:

- **Interface Analysis for InP based-QCLs**
    - through APT, XRD, TEM and AFM characterization of strained layer SLs

In addition to the SLs typically grown as calibration samples for a QCL, we have investigated an STA-QCL full laser structure through APT. This QCL designed for emission at 4.8 μm [5], consists of an active region with various thicknesses and compositions unlike the bilayer motif in the SL samples. This entails much more complicated HR-XRD fitting and consequently difficulty in

creating an accurate reconstruction. It is, therefore, better to break down the problem into simpler SL structures for analysis. Moreover, growth conditions such as interruption interval between the SL layers, growth rates, V/III ratios, reactor geometry and residence time are known to affect the compositional grading at the interfaces [6]–[9]. It is important to ascertain if the observed composition profiles truly exist because of the SL design and growth specifications, and not as an artifact of the APT probing direction. This could be accomplished by preparing APT specimens in the growth direction such that the substrate is encountered first during the experiment. A specialized Al holder is required for flipping the sample during the FIB process as explained by Martens et al. [10]. The impact of the interface properties on device performance can be evaluated by fabricating and testing devices grown under conditions known to affect the interface gradient. In addition to APT, photoluminescence measurements are needed on SLs with varying thickness thin (<2 nm) layers such that the optical characteristics are sensitive to the interfacial gradient.

- Through the evaluation of device performance

CMP and CP surface preparation processes need optimization before they can be successfully be applied to the InP MBLs. CMP has previously shown to improve the fidelity of SL structures and stage of the QCL active region [11]. This also helps to avoid any strain relaxation due to surface roughness. Similar surface preparation applied to InP MBLs will enable growth of 40 stages of the active region. It is important also because it enables III-V optoelectronics integration with low-cost Si substrates and Si photonics integration.

- **Growth of QCL MOCVD-grown InGaAs MBL employing the design established**

The second suggested task is to perform the QCL growth on an InGaAs MBL, grown by high growth rate MOCVD. A design for the same has been presented with optimized key parameters,

thermal and optical modeling. The main advantage for this design is being able to achieve 3.4 μm emission wavelength on a substrate with a lattice constant intermediate to InP and GaAs, such that large conduction band offsets between wells and barriers are obtained without increasing the average strain. The MBL design employs relatively low indium content QWs in the active region, compared with the short-wavelength (<3.4 μm) QCLs on conventional InP substrates. The low indium content active region design is expected to eliminate a major carrier loss mechanism, leakage to indirect (X, L) valleys [1], [12]. This also opens up an arena of growing custom-made MBLs according to the QCL requirements.

Higher growth rate (>10 μm/hr) InGaAs MBLs can be grown by MOCVD. The effect of substrate miscut and growth temperature on observed threading dislocation density and cross-hatched surface morphology can be studied. Previously, hillock-like features were observed on the surface of InGaAs MBLs grown by HVPE [11], which are absent from the surfaces MBLs grown by MOCVD. Lower etch pit density (~10^6 cm^{-2}) along with hillock free surfaces are promising to obtain highly reproducible, high growth rate MBLs by MOCVD, which can then be used for QCL device regrowths.

References

[1] A. Rajeev, C. Sigler, T. Earles, Y. V Flores, L. J. Mawst, and D. Botez, "Design considerations for λ ~ 3.0-to 3.5-μm-emitting quantum cascade lasers on metamorphic buffer layers," *Opt. Eng.*, vol. 57, no. 1, p. 011017(1-10), 2017.

[2] L. J. Mawst *et al.*, "Low-strain, quantum-cascade-laser active regions grown on metamorphic buffer layers for emission in the 3.0–4.0 μm wavelength region," *IET Optoelectron.*, vol. 2013.0060, no. 10.1049, pp. 1–8, 2013.

[3] L. J. Mawst *et al.*, "Quantum-cascade-laser active regions on metamorphic buffer layers," in *Proceedings of SPIE - The International Society for Optical Engineering*, 2015, vol. 9370.

[4] D. Botez, C. C. Chang, and L. J. Mawst, "Temperature sensitivity of the electro-optical characteristics for mid-infrared (λ = 3-16 μm)-emitting quantum cascade lasers," *J. Phys. D. Appl. Phys.*, vol. 49, no. 043001, pp. 1–33, 2016.

[5] D. Botez *et al.*, "High internal differential efficiency mid-infrared quantum cascade lasers," *Proc. SPIE*, vol. 10123, p. 101230Q1-12, 2017.

[6] Y. Huang *et al.*, "Optimization of growth conditions for InGaAs/InAlAs/InP quantum cascade lasers by metalorganic chemical vapor deposition," *J. Cryst. Growth*, vol. 316, pp. 75–80, 2011.

[7] C. A. Wang *et al.*, "High power (>5W) λ~9.6μm tapered quantum cascade lasers grown by OMVPE," *J. Cryst. Growth*, vol. 370, pp. 212–216, 2013.

[8] J. C. Shin, L. J. Mawst, and D. Botez, "Crystal growth via metal-organic vapor phase epitaxy of quantum-cascade-laser structures composed of multiple alloy compositions," *J. Cryst. Growth*, vol. 357, pp. 15–19, 2012.

[9] R. P. Green *et al.*, "Room-temperature operation of InGaAs/AlInAs quantum cascade lasers grown by metalorganic vapor phase epitaxy," *Appl. Phys. Lett.*, vol. 83, no. 10, pp. 1921–1922, 2003.

[10] R. L. Martens, F. Fei, and F. E. G. Tem, "Specimen Preparation for Atom Probe Tomography," *Appl. Microsc.*, vol. 46, no. 1, pp. 14–19, 2016.

[11] A. Rajeev *et al.*, "Regrowth of quantum cascade laser active regions on metamorphic buffer layers," *J. Cryst. Growth*, vol. 452, pp. 268–271, 2016.

[12] M. P. Semtsiv, M. Wienold, S. Dressler, and W. T. Masselink, "Short-wavelength (λ ≈ 3.05 μm) InP based strain compensated quantum-cascade laser," *Appl. Phys. Lett.*, vol. 90, no. 051111, 2007.